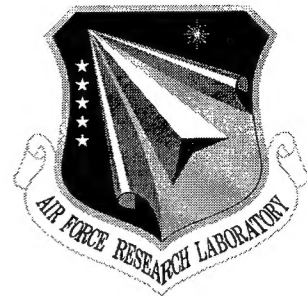


**AFRL-SN-RS-TR-1999-94**  
**Final Technical Report**  
**May 1999**



## **THE EIGENCANCELER: SPACE TIME ADAPTIVE RADAR BY EIGENANALYSIS METHODS**

**New Jersey Institute of Technology**

**Alexander M. Haimovich and Tareq F. Ayoub**

*APPROVED FOR PUBLIC RELEASE; DISTRIBUTION UNLIMITED.*

**19990719 123**

**AIR FORCE RESEARCH LABORATORY  
SENSORS DIRECTORATE  
ROME RESEARCH SITE  
ROME, NEW YORK**

**DTIC QUALITY INSPECTED 4**

This report has been reviewed by the Air Force Research Laboratory, Information Directorate, Public Affairs Office (IFOIPA) and is releasable to the National Technical Information Service (NTIS). At NTIS it will be releasable to the general public, including foreign nations.

AFRL-SN-RS-TR-1999-94 has been reviewed and is approved for publication.

APPROVED:



MARK L. PUGH  
Project Engineer

FOR THE DIRECTOR:



ROBERT G. POLCE, Acting Chief  
Rome Operations Office  
Sensors Directorate

If your address has changed or if you wish to be removed from the Air Force Research Laboratory Rome Research Site mailing list, or if the addressee is no longer employed by your organization, please notify AFRL/SNRT, 26 Electronic Parkway, Rome, NY 13441-4514. This will assist us in maintaining a current mailing list.

Do not return copies of this report unless contractual obligations or notices on a specific document require that it be returned.

REPORT DOCUMENTATION PAGE			Form Approved OMB No. 0704-0188
<p>Public reporting burden for this collection of information is estimated to average 1 hour per response, including the time for reviewing instructions, searching existing data sources, gathering and maintaining the data needed, and completing and reviewing the collection of information. Send comments regarding this burden estimate or any other aspect of this collection of information, including suggestions for reducing this burden, to Washington Headquarters Services, Directorate for Information Operations and Reports, 1215 Jefferson Davis Highway, Suite 1204, Arlington, VA 22202-4302, and to the Office of Management and Budget, Paperwork Reduction Project (0704-0188), Washington, DC 20503.</p>			
1. AGENCY USE ONLY (Leave blank)	2. REPORT DATE	3. REPORT TYPE AND DATES COVERED	
	May 1999	Final Jul 94 - Nov 97	
4. TITLE AND SUBTITLE		5. FUNDING NUMBERS	
THE EIGENCANCELER: SPACE TIME ADAPTIVE RADAR BY EIGENANALYSIS METHODS		C - F30602-94-1-0012 PE - 62702F PR - 4600 TA - A0 WU - A9	
6. AUTHOR(S)		8. PERFORMING ORGANIZATION REPORT NUMBER	
Alexander M. Haimovich and Tareq F. Ayoub		N/A	
7. PERFORMING ORGANIZATION NAME(S) AND ADDRESS(ES)		10. SPONSORING/MONITORING AGENCY REPORT NUMBER	
New Jersey Institute of Technology 323 Martin Luther King Blvd. Newark NJ 07102-1982		AFRL-SN-RS-TR-1999-94	
9. SPONSORING/MONITORING AGENCY NAME(S) AND ADDRESS(ES)		11. SUPPLEMENTARY NOTES	
Air Force Research Laboratory/SNRT 26 Electronic Parkway Rome NY 13441-4514		Air Force Research Laboratory Project Engineer: Mark L. Pugh/SNRT/(315) 330-7684	
12a. DISTRIBUTION AVAILABILITY STATEMENT		12b. DISTRIBUTION CODE	
Approved for public release; distribution unlimited.			
13. ABSTRACT (Maximum 200 words)		<p>In airborne surveillance radar applications, adaptive antennas provide for the detection of small targets in severe clutter environments. Adaptive antennas are currently being considered for the design of next generation surveillance platforms. The radar problem is two-dimensional with radar returns being a function of both angle and Doppler. Space-Time Adaptive Processing (STAP) is required for rejection of interferences in the space-time domains. To make STAP feasible for incorporation into future systems, low complexity algorithms are required. The space-time radar problem is well suited to the application of techniques that take advantage of the low-rank properties associated with the interference in such radars. The Eigencanceler is an interference cancellation method based on the spectral decomposition (eigenanalysis) of the space-time covariance matrix. The linear space spanned by the columns of the space-time covariance matrix is formed by the union of the algebraic spaces of the interference and the noise. The Eigencanceler's weight vector is designed to lie in the noise subspace and to provide a prescribed gain to the desired signal. Thus significant computational savings are realized since a Weiner filter requires a matrix inversion, while the eigencanceler is implemented by computing only a limited number of interference eigenvectors.</p>	
14. SUBJECT TERMS		15. NUMBER OF PAGES	
Space-Time Adaptive Processing, Eigenanalysis, Signal Processing		132	
16. PRICE CODE			
17. SECURITY CLASSIFICATION OF REPORT	18. SECURITY CLASSIFICATION OF THIS PAGE	19. SECURITY CLASSIFICATION OF ABSTRACT	20. LIMITATION OF ABSTRACT
UNCLASSIFIED	UNCLASSIFIED	UNCLASSIFIED	UL

## EXECUTIVE SUMMARY

This report summarizes the work on "The Eigencanceler: Space-Time Adaptive Radar by Eigenanalysis Methods" carried out at the New Jersey Institute of Technology from 6/94 to 9/97. The main contribution of this work was to develop and study an adaptive radar signal processing method referred to as *eigencanceler*. In airborne surveillance radar applications, adaptive antennas provide for the detection of small targets in severe clutter environments. Adaptive antenna arrays are currently being considered for the design of the next generation surveillance platforms. The radar problem is two-dimensional with radar returns being a function of both angle and Doppler. Space-time adaptive processing (STAP) is required for rejection of interferences in the space-time domains. To make STAP feasible for incorporation in future systems, low complexity algorithms are required. The space-time radar problem is well suited to the application of techniques that take advantage of low-rank property associated with the interference in such radars.

The eigencanceler is an interference cancellation method based on the spectral decomposition (eigenanalysis) of the space-time covariance matrix. The linear space spanned by the columns of the space-time covariance matrix is formed by the union of the algebraic spaces of the interference and the noise. The eigencanceler's weight vector is designed to lie in the noise subspace, and to provide a prescribed gain to the desired signal. Thus significant computational savings are realized since a Wiener filter requires a matrix inversion, while the eigencanceler is implemented by computing only a limited number of eigenvectors (interference eigenvectors).

Application of Wiener filtering required knowledge of the true space-time covariance matrix. In radar applications, the space-time covariance matrix (including contributions of jammers, clutter, and noise) cannot be known *a priori*, hence it needs to be estimated from the observations. The sample matrix inversion method (SMI) consists of substituting the estimated covariance matrix for the true coavariance matrix in the Wienre filter. It is well known that to achieve an output signal-to-noise ratio (SNR) within 3 dB of the optimal, the number of independent space-time snapshots required is  $K = 2N$ , where  $N$  is the dimensionality of the space-time array. While preserving the linear architecture of the radar detector, the SMI detector has a number of drawbacks: (1) it is not optimal for detection performance, (2) it has slow convergence for large dimensionallity  $N$  (i.e., large number of snapshots required), (3) it is sensitive to calibration errors, (4) it is not CFAR. In this report it is shown that the eigencanceler addresses many of the SMI's deficiencies.

The following specific contributions of this report are noted:

1. Formulation of the eigencanceler method [1, 2]. The eigencanceler provides better detection performance in cases of limited data support (low number of snapshots for coavariance matrix estimation). It is shown that the number of snapshots required is  $K = 2r$ , where  $r$  is the rank of the interference subspace. For a calibrated space-time array,  $r$  is usually much smaller than the array dimensionallity  $N$ . Alternatively, for the same number of snapshots, the eigencanceler delivers much better performance.
2. Development of the theory of the eigencanceler. Radar performance is commonly measured in terms of detection and false alarm probabilities. In turn, those are determined by the, so-called, *conditioned signal-to-noise ratio* (CSNR). The statistical characterization of the SMI CSNR has been known for some time. In this report the probability density function of the eigencanceler is developed. This work has been also published in a recent journal publication [3]. The development is based on the asymptotic distribution of the principal components of the covariance matrix. It is shown that, unlike the SMI method, the eigencanceler yields a conditioned SNR distribution that is dependent on the covariance matrix. Several covariance matrix independent approximations of the distribution are developed for the large interference-to-noise case.

3. Performance analysis of the eigencanceler. This work is significant in that several adaptive methods were evaluated using experimental data supplied by the Air Force Research Laboratory (AFRL). The performance of the eigenanalysis-based detector is analyzed with respect to convergence rate and robustness to calibration errors. Analytical expressions are developed for receiver operating curves when the clutter signal environment is assumed to be Gaussian. Simulation results are provided to corroborate the theoretical analysis. Examples of experimental data from the Mountaintop dataset are used to illustrate the higher convergence rate and increased robustness of the eigenanalysis method. In the course of this work various techniques had to be developed to enable the utilization of the experimental data, such as calibrations and other processes. This work is also reported on in the journal publication [4] and conference publications [5, 6]. It is shown, through analysis of the Mountaintop dataset, that the SMI method is very sensitive to target leakage in the training set. This requires large guard rails around the cell under test. It is shown that the eigencanceler is less susceptible to this type of errors.
4. Other reduced-rank methodss are also studied. These methods' utility is demonstrated by simulations in terms of the output signal-to-noise ratio and detection probability. It is shown that reduced-rank processing has two opposite effects on the performance: increased statistical stability which tends to improve performance, and introduction of a bias which lowers the signal-to-noise ratio. Several reduced-rank methods are analyzed and compared for both cases of known and unknown covariance matrix. While best performance is obtained using transforms based on the eigendecomposition (data dependent), the loss incurred by the application of fixed transforms (such as the discrete cosine transform) is relatively small. The main advantage of fixed transforms is the availability of efficient computational procedures for their implementation. These findings suggest that reduced-rank methods could facilitate the development of practical, real-time STAP technology. This work is also reported on in publications [7].
5. The application of the eigencanceler to the high pulse repetition frequency (HPRF) radar is demonstrated. High pulse repetition frequency radars are employed for airborne applications due to their capability to place high closing-rate targets in the clutter-free region. The highly ambiguous range returns, may however, cause low Doppler targets to compete with near-range strong clutter. It is shown that STAP techniques are required to reject the near-range clutter returns which mask low Doppler targets. As a result of range ambiguity of the HPRF radar, the sample support for estimating the array covariance matrix is limited, leading to an ill-conditioned problem. Hence, the traditional SMI technique, if applicable, results in poor performance. Reduced rank techniques such as the eigencanceler applied to the HPRF airborne STAP problem are shown to perform well in terms of the CSNR and probability of detection. This work is also reported on in publications [8, 5].

## TABLE OF CONTENTS

Chapter	Page
1 INTRODUCTION .....	1
2 SIGNAL ENVIRONMENT .....	3
2.1 Signal Model .....	3
2.2 Optimum Radar Signal Processing .....	4
2.3 The Minimum Variance Beamformer .....	5
3 ADAPTIVE RADAR METHODS .....	8
3.1 The Eigencanceler .....	8
3.1.1 Eigenstructure of the Correlation Matrix .....	9
3.1.2 Optimization Criteria .....	12
3.1.3 Steady State Analysis .....	13
3.1.4 Perturbation Analysis .....	15
3.2 Simulations .....	16
3.3 Discussion .....	22
4 ASYMPTOTIC DISTRIBUTION OF THE CONDITIONAL SIGNAL-TO-NOISE RATIO .....	24
4.1 Distribution of the CSNR .....	25
4.1.1 Perturbation Analysis of the Noise Subspace .....	26
4.1.2 Computation of the PDF .....	29
4.1.3 Discussion .....	33
4.1.4 Approximation for Large INR .....	33
4.2 Numerical Results .....	34
4.3 Discussion .....	43
5 PERFORMANCE ANALYSIS .....	44
5.1 Performance Analysis .....	44
5.1.1 Detection .....	44

Chapter		Page
5.1.2 Robustness . . . . .		47
5.1.3 Numerical Results . . . . .		49
5.2 Discussion . . . . .		50
<b>6 PERFORMANCE ANALYSIS USING EXPERIMENTAL DATA . . . . .</b>		<b>52</b>
6.1 The Mountaintop Data Package . . . . .		52
6.1.1 Description of the Assets . . . . .		52
6.1.2 Calibration . . . . .		54
6.1.3 Pulse Compression . . . . .		58
6.2 Joint Domain and Cascade Processors . . . . .		58
6.3 Array Improvement Factor . . . . .		63
6.4 Array Improvement Factor Calculations . . . . .		65
6.5 Mountaintop Data Analysis . . . . .		68
6.5.1 Description of the Data Files . . . . .		68
6.5.2 Target Range Detection . . . . .		75
6.5.3 Antenna Pattern . . . . .		77
6.5.4 Target Angle Detection . . . . .		84
6.5.5 Signal Cancellation . . . . .		84
6.6 Discussion . . . . .		89
<b>7 PERFORMANCE COMPARISON OF REDUCED RANK STAP TECHNIQUES . . . . .</b>		<b>91</b>
7.1 Reduced Rank Processing with Known Covariance . . . . .		91
7.2 Reduced Rank Processing with Unknown Covariance . . . . .		95
7.3 Numerical Results . . . . .		96
<b>8 EIGENCANCELER APPLIED TO HPRF RADAR . . . . .</b>		<b>100</b>
8.1 Problem Statement . . . . .		100
8.2 HPRF System's Definitions and Properties . . . . .		102
8.2.1 System's Definitions . . . . .		102
8.2.2 Degrees of Freedom . . . . .		103

Chapter	Page
8.2.3 ‘J-Hook’ Clutter . . . . .	104
8.3 STAP Techniques . . . . .	104
8.3.1 Pseudoinverse SMI . . . . .	104
8.3.2 Diagonally Loaded SMI . . . . .	105
8.3.3 The Eigencanceler . . . . .	105
8.4 Numerical Analysis . . . . .	105
APPENDIX A Derivations of equations (5.25) and (5.26) . . . . .	110
REFERENCES . . . . .	112

## LIST OF FIGURES

Figure	Page
2.1 Space-time array structure . . . . .	4
3.1 Eigenvalues of the space-time covariance matrix . . . . .	11
3.2 The eigencanceler architecture . . . . .	13
3.3 Geometrical interpretation . . . . .	14
3.4 Spatial patterns. $K = 10N$ . . . . .	17
3.5 Frequency response patterns. $K = 10N$ . . . . .	18
3.6 Spatial patterns. $K = N$ . . . . .	19
3.7 Frequency response patterns. $K = N$ . . . . .	20
3.8 Improvement factors vs. CNR. $K = N$ . . . . .	21
3.9 3D plots of the received signal and space-time patterns. $K = N$ . Notice the “notch” in Figure (b) corresponding to the clutter “ridge” in (a). . . . .	22
4.1 Simulation clutter map. The vertical line indicates the steering vector. . . . .	35
4.2 The mean conditioned signal to noise ratio as a function of the clutter to noise ratio for covariance matrix estimates using $K = 2N$ samples. . . . .	36
4.3 The mean conditioned signal to noise ratio as a function of the clutter to noise ratio for covariance matrix estimates using $K = 3N$ samples. . . . .	38
4.4 The mean conditioned signal to noise ratio as a function of the clutter to noise ratio for covariance matrix estimates using $K = 4N$ samples. . . . .	39
4.5 The mean conditioned signal to noise ratio as a function of the number of snapshots for CNR = 10 dB. . . . .	40
4.6 The mean conditioned signal to noise ratio as a function of the number of snapshots for CNR = 10 dB for low number of samples. . . . .	41
4.7 Density functions of the CSNR for CNR = 10 dB and $K = 4N$ snapshots. . . . .	42
5.1 Signal cancelation effects: $G_e$ , $G_o$ vs. $\gamma_s$ with $\gamma_i$ as parameter. . . . .	49
5.2 Probability density of the CSNR. Top: simulations. Bottom: theoretical. . . . .	51
5.3 Probability of detection from theory and simulations. . . . .	51
6.1 The Radar Surveillance Technology Experimental Radar (RSTER) . . . . .	53

Figure	Page
6.2 Transversal Linear Prediction Filter . . . . .	55
6.3 Results of Receiver and Antenna Calibration . . . . .	57
6.4 Chirp Signal . . . . .	59
6.5 Chirp Signal Matched Filter Output . . . . .	60
6.6 Block Diagram of Joint-Domain and Cascade Processors . . . . .	62
6.7 Effects of Desired Signal Component and Pointing Error on the AIF . . . . .	69
6.8 Effects of Phase Errors and Pointing Error on the AIF . . . . .	70
6.9 Effects of Amplitude Errors and Pointing Error on the AIF . . . . .	71
6.10 Effects of Signal-to-Noise Ratio and Pointing Error on the AIF . . . . .	72
6.11 Effects of Desired Signal Angle and Pointing Error on the AIF . . . . .	73
6.12 Magnitude Plot of Range Returns on IDPCA Data, CPI 6, PRI 1 . . . . .	74
6.13 Doppler-Azimuth Plot for Target Range Cell . . . . .	75
6.14 Eigenvalues of the Data . . . . .	76
6.15 Joint-Domain Range Plots Using 300 Training Points . . . . .	78
6.16 Post-Doppler Range Plots Using 300 Training Points . . . . .	79
6.17 Post-Doppler Range Plots Using 50 Training Points . . . . .	80
6.18 Post-Doppler Range Plots Using 28 Training Points . . . . .	81
6.19 Post-Doppler Antenna Pattern Plots Using 300 Training Points . . . . .	82
6.20 Post-Doppler Antenna Pattern Plots Using 50 Training Points . . . . .	83
6.21 Post-Doppler Antenna Pattern Plots Using 28 Training Points . . . . .	85
6.22 Post-Doppler Target Detection Using 300 Training Points . . . . .	86
6.23 Post-Doppler Target Detection Using 50 Training Points . . . . .	87
6.24 Post-Doppler Target Detection Using 28 Training Points . . . . .	88
6.25 Signal Cancellation . . . . .	90
7.1 Reduced-rank MVB . . . . .	92
7.2 Reduced-rank GSC . . . . .	92
7.3 Probability density of the CSNR . . . . .	97

<b>Figure</b>	<b>Page</b>
7.4 Probability of detection for reduced-rank methods. . . . .	97
7.5 Rank order. . . . .	98
7.6 CSNR vs CNR. . . . .	99
8.1 Geometry of the airborne radar problem. . . . .	101
8.2 Iso-Doppler, Iso-range ring map for LPRF radar. . . . .	101
8.3 Iso-Doppler, Iso-range ring map for HPRF radar. . . . .	102
8.4 HPRF Clutter Intensity map. . . . .	104
8.5 PDF of the CSNR obtained by averaging 2000 runs. . . . .	106
8.6 Probability of detection of the CSNR obtained by averaging 200 runs. . . . .	106
8.7 Clutter map for HPRF radar. . . . .	107
8.8 Post-processing clutter using the Loaded SMI. . . . .	108
8.9 Post-processing clutter using the eigencanceler. . . . .	109
A.1 Geometry for robustness analysis. . . . .	111

## CHAPTER 1

### INTRODUCTION

The theory of space-time adaptive processing (STAP) was pioneered by Brennan and Reed [9]. They showed that the optimal Neyman-Pearson detector for a known signal vector in colored Gaussian noise with a known covariance matrix is linear, i.e., it consists of a linear combination of the vector's components. In practice, the noise (a collective reference to background noise+clutter+jammers) covariance matrix is typically not known. The common approach is to estimate it from a *secondary* data set that does not contain the signal of interest. In radar, the secondary data may be composed of signals from range cells adjacent to the one under observation. Reed et. al. suggested the Sample Matrix Inversion (SMI) method, in which an estimate is substituted for the noise covariance matrix expression in the linear detector [10]. They developed an expression for the density of the SNR loss with respect to the optimal case and showed that if the signal vector dimension is  $N$ , the number of samples required to achieve performance within 3 dB of the optimal, is approximately  $K = 2N$ . This convergence has the remarkable property of being independent from the true noise covariance matrix. Other authors have analyzed the performance of the linear detector with estimated covariance matrix [11], [12], and [13]. While preserving the linear architecture of the detector, the SMI detector has a number of drawbacks: (1) it is not optimal for detection performance, (2) it has slow convergence for large  $N$ , (3) it is sensitive to calibration errors, and (4) it is not CFAR. Subsequent work addressed some of these concerns. A detector for a signal vector with unknown amplitude and in unknown colored noise was derived by Kelly from a generalized likelihood ratio (GLR) test [14]. Unfortunately, the GLR-based detector is more complex and has convergence properties similar to the SMI detector. The SMI method was shown to be sensitive to calibration errors [15, 16]. Various remedies have been suggested, for example, [17, 18], which reduce sensitivity to calibration errors at the expense of some added complexity. CFAR modifications of the SMI detector were suggested and analyzed in [19] and [20]. While deficiencies of the SMI detector have been addressed on an individual basis, a comprehensive approach for the design of a linear detector with fast convergence, increased robustness, and CFAR capability, has been lacking. Most of these desired features can be achieved in the case of STAP radar, by a linear eigenanalysis-based detector. Such a detector is derived from partitioning the signal space into *interference* and *noise* subspaces and computing a weight vector in the noise subspace. The interference subspace contains the clutter contributions. Two forms of the eigenanalysis-based detector have been referred to as the eigencanceler [21, 1] and the PCI method in [22]. The eigencanceler is a modification of the minimum variance beamformer. The minimum variance beamformer minimizes the array output subject to a set of linear constraints [23]. The eigencanceler produces the minimum norm weight vector meeting the set of linear constraints, and subject to the additional constraint of orthogonality to the interference subspace [24]. The PCI is derived as a linear detector of data from which the interference has been removed [22]. In the case of a single steering vector constraint, the two methods provide similar solutions. In [1] we show that the space-time clutter covariance matrix for a uniform array and fixed PRF is essentially low rank, due to the inherent oversampling nature of the STAP architecture. Hence, the space-time radar problem is well

suited to the application of techniques that take advantage of the low-rank property. The eigenanalysis-based method has been shown to have a faster convergence rate than the SMI method. Specifically, it has been shown that the number of samples required for an average loss of 3 dB with respect to the optimal detector is  $2r$ , where  $r$  is the interference space rank [25, 1]. This finding is particularly significant when  $r \ll N$ , which turns out to be the case for a typical space-time radar.

In this report, we describe various adaptive radar techniques and discuss their performance in comparison with reduced rank techniques, mainly the eigencanceler. Our interest in those methods arises since it has been shown that when the interference is contained within a subspace of the signal space, and the interference+noise covariance matrix is estimated from a dataset with limited support, reduced-rank methods actually *outperform* full-rank adaptive processing. This is explained by the presence, in addition to thermal noise effects, of errors resulting from the estimation process. Reduced-rank processing suppresses estimation errors at the cost of a bias in the SNR. The net effect, however, is a significant performance improvement for cases when the interference may be modeled as low-rank. Reduced-rank methods are clearly important for STAP radar, where a large number of degrees of freedom may be available.

This report is organized as follows: Chapter 2 presents the signal model that will be used through this work and also presents some background into adaptive processing. Chapter 3 introduces the the Eigencanceler and discusses its weight vector. Chapter 4 has the derivation of the distribution of the conditioned signal-to-noise ratio (CSNR) for the eigencanceler as a performance measure. A performance comparison between the eigencanceler and full-rank adaptive radar techniques is given in Chapters 5 and 6. The eigencanceler's performance is compared with other reduced-rank techniques in Chapter 7. In Chapter 8, the eigencanceler is applied to high pulse repetition frequency (HPRF) airborne radar.

## CHAPTER 2

### SIGNAL ENVIRONMENT

In this chapter, the mathematical model for the type of signals addressed in the report is presented. The optimum and linearly constrained weight vectors are introduced, and their deficiencies are discussed. The following notation is adopted: boldface lower case letters denote vectors, boldface upper case letters denote matrices, the superscript H denotes Hermitian transpose.

#### 2.1 Signal Model

Consider a space-time array with  $N_s$  antennas uniformly spaced and a  $N_t$  pulse coherent pulse interval (CPI) as shown in Figure 2.1. The array is side-looking, i.e., its axis is parallel to the flight axis. The complex envelope of the signal received at the array from a point source, is given by the vector  $\mathbf{s}_s = (1, \dots, e^{j(N_s-1)u})^T$ , where  $u$  is the normalized spatial frequency given by

$$u = \frac{2\pi}{\lambda} d \sin \theta \quad (2.1)$$

and  $d$ ,  $\lambda$ , and  $\theta$  are the inter-element spacing, wavelength and angle of arrival, respectively. The complex envelope sampled at the first array element is represented by the vector  $\mathbf{s}_t = (1, \dots, e^{j(N_s-1)v})^T$ , where  $v$  is the normalized Doppler frequency

$$v = \frac{2v_r}{\lambda f_r} \quad (2.2)$$

and  $v_r$  and  $f_r$  are the radar-target radial velocity and the radar PRF, respectively. The  $(N = N_s N_t)$ -dimensional target vector is defined

$$\mathbf{s} = \frac{1}{\sqrt{N}} \mathbf{s}_s \otimes \mathbf{s}_t \quad (2.3)$$

where  $\otimes$  denotes the Kronecker product.

Under hypothesis  $H_0$  the received signal  $\mathbf{x}$  consists only of clutter  $\mathbf{c}$  and noise  $\mathbf{v}$  contributions:

$$\mathbf{x} = \mathbf{c} + \mathbf{v} \quad (2.4)$$

where  $\mathbf{x}$  is assumed a zero-mean, circularly symmetric complex Gaussian random vector with covariance matrix  $\mathbf{R}$ . Under hypothesis  $H_1$ ,  $\mathbf{x}$  is given by

$$\mathbf{x} = a\mathbf{s} + \mathbf{c} + \mathbf{v} \quad (2.5)$$

where  $a$  is a zero-mean, circularly symmetric complex Gaussian random variable with variance  $\sigma_s^2$ .

Since the colored noise (colored noise refers to the aggregate of noise+clutter+interferences) covariance matrix is usually not known, an estimate is used. The estimate is

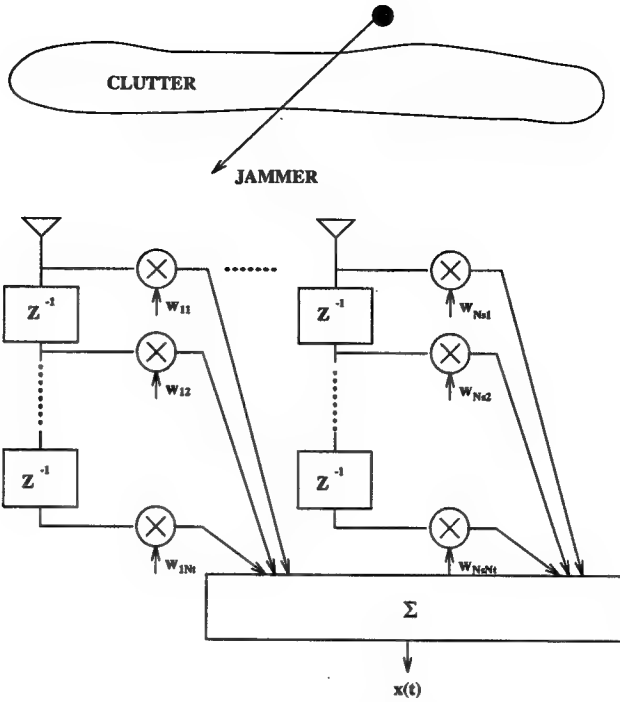


**Figure 2.1** Space-time array structure

derived from range cells in the vicinity of the tested range cell and is termed “secondary data”. The secondary data consists of clutter returns and, possibly, other interferences, such as jammers. The presence of narrowband jammers does not alter the signal model as presented. In the sequel, the terms clutter and interference are used interchangeably. The assumption is that the secondary  $\mathbf{x}_k$ ,  $k = 1, \dots, K$ , data has the same statistical properties as the tested cell under hypothesis model  $\mathbf{H}_0$ . The maximum likelihood estimate of the covariance matrix is given by

$$\widehat{\mathbf{R}} = \frac{1}{K} \sum_{k=1}^K \mathbf{x}_k \mathbf{x}_k^H \quad (2.6)$$

## 2.2 Optimum Radar Signal Processing

The theory of adaptive radar was established in a series of publications by Brennan, Mallett, and Reed [9], [26]. They showed that if a disturbance is a stationary process, and the components of the corresponding array vector are distributed jointly Gaussian, then the likelihood ratio test for detecting the signal in the presence of the disturbance is maximized by a weighted linear combination of the array outputs using the following weight vector:

$$\mathbf{w}_o = k \mathbf{R}^{-1} \mathbf{s} \quad (2.7)$$

where  $k$  is a gain constant. Equation (2.7) represents the classical Wiener filter. It can be interpreted as a cascade of a whitening filter for the interference, followed by a matched filter for the modified (by the whitening operation) useful signal.

The solution in (2.7) requires a-priori knowledge of the space-time correlation matrix  $\mathbf{R}$ . In practice we work with a finite segment of data from which  $\mathbf{R}$  is estimated. In this case the solution is not optimal anymore, indeed its quality depends on the goodness of the correlation matrix estimate.

The signal environment can be assumed stationary only over short periods, hence the correlation matrix estimate needs to be continually updated. A number of adaptive procedures have been advanced over the years for updating the array weight vector. The Howells-Applebaum loop [27] is an analog implementation of the adaptive filter and it makes use of the known angle of arrival of the desired signal. The Least Mean Square (LMS) algorithm [28] is identical from a mathematical viewpoint to the Howell- Applebaum algorithm, but uses a reference signal rather than a steering vector, hence is less suited to radar problems and more applicable to communications. Both algorithms are attractive for their simplicity, but convergence times are dependent on the spread of the eigenvalues of the correlation matrix. Other methods invariably trade away simplicity for speed. The Direct Inversion Method (DMI) [10], is fast and independent of eigenvalues, but necessitates order of  $(M^2)$  operations per iteration, where  $M = \dim(\mathbf{R})$ , compared to order of  $(M)$  operations for the LMS algorithm. Other adaptive radar approaches are available. For example the sidelobe canceler can be implemented using the Linear Prediction Method (LPM) [29]. Application of the Levinson-Durbin algorithm to the LPM problem avoids the matrix inversion [30]. Closely related to (LPM) is the Maximum Entropy Method (MEM) [31].

### 2.3 The Minimum Variance Beamformer

Often in radar there is the requirement for some control over the beam pattern in addition to cancelling interferences. This requires the introduction of steering point and velocity constraints. With the Maximum Likelihood Method (MLM) [32], a filter is designed to pass a narrowband signal while rejecting all other signals in an optimal manner. This method is closely related to the Minimum Variance Distortionless Response (MVDR) technique for spectral estimation. In adaptive beamforming this is known as the Minimum Variance Beamformer (MVB) [23]. In some cases the steering point constraint is required over a range of angles and Doppler frequencies. One way to force the beamformer response over an interval is to prescribe the response at preselected points in space and frequency. The optimal weight vector is then obtained by solving the linearly constrained minimization problem [33]:

$$\min_w \mathbf{w}^H \mathbf{R} \mathbf{w} \text{ subject to } \mathbf{C}^H \mathbf{w} = \mathbf{f} \quad (2.8)$$

where  $\mathbf{C}$  is the  $N \times J$  constraint matrix ( $N = N_s N_t$ ), and  $\mathbf{f}$  is the response vector. The weight vector that satisfies (2.8) is given by:

$$\mathbf{w}_o = \mathbf{R}^{-1} \mathbf{C} (\mathbf{C}^H \mathbf{R}^{-1} \mathbf{C})^{-1} \mathbf{f} \quad (2.9)$$

This solution is optimal in the sense that, if the interference can be represented by a stationary process with known 2-nd order statistics (correlation matrix), then it provides the minimum output noise power (jammers+clutter+noise) for a constrained desired signal response.

When applied to practical radar situations, the minimum variance beamformer has a number of drawbacks which are summarized below:

1. *Data Record Size.* The minimum variance weight vector is not optimal if the correlation matrix  $\mathbf{R}$  is not known. The correlation matrix can be estimated using the relation given in (2.6). If  $\mathbf{x}$  is Gaussian then it can be shown that  $\widehat{\mathbf{R}}$  has a Wishart distribution [10] and a reasonable estimate can be obtained when the number of snapshots used in the estimate is at least twice as large as  $\text{dim}[\mathbf{R}]$ , i.e.,  $K = 2N$ . Given an estimate of  $\mathbf{R}$  derived from a short data record, it is known that elements  $\widehat{\mathbf{R}}(i, j)$  provide poor estimates for large  $(i, j)$  space-time lags [34]. Consequently, the MVB is deficient for short data records.
2. *Pattern Robustness.* It can be shown that the optimal weight vector of the form  $\mathbf{w}_o = k\mathbf{R}^{-1}\mathbf{s}$ , can also be written (leaving out constant gain factors) as [35]:

$$\mathbf{w}_o = \mathbf{s} - \sum_{i=1}^{N-1} (1 - 1/\bar{\lambda}_i)(\mathbf{q}_i^H \mathbf{s}) \mathbf{q}_i \quad (2.10)$$

where  $\bar{\lambda}_i$ 's are the eigenvalues of  $\mathbf{R}$  indexed in descending order and normalized to the smallest eigenvalue  $\lambda_N$ . The vector  $\mathbf{q}_i$  is the eigenvector corresponding to  $\bar{\lambda}_i$ . Equation (2.10) indicates that the optimal weight vector consists of weighted eigenvector beams subtracted from the quiescent weight vector  $\mathbf{d}_s$ . The quiescent weight vector is just the steering vector to the desired signal which can also be viewed as the matched filter to a signal at specified angle and frequency. The eigenvector beams subtract from the quiescent beam to produce nulls in the directions of interferences. From (2.10) it can be seen that all the eigenvectors affect the sidelobes of the space-time pattern. The error variance in the pattern is inversely related to the number of samples and to the true value of the eigenvalues [36], hence, for short data records the fluctuations of the noise eigenvectors between updates can cause large variations in the array pattern.

3. *Computational Complexity.* The solution in (2.8) requires a matrix inversion. That could be a fairly costly operation which requires an order of  $(N)^3$  multiplications. Obviously,  $(N)^3$  could be large even for moderate number of sensors and filter taps. A number of adaptive procedures have been advanced for on-line computation of the minimum variance weight vector. Frost's algorithm [33] is a modification of the LMS algorithm and, as such, is plagued by the same poor convergence problems. The Recursive Least Squares (RLS) algorithm exploits the well known matrix inversion lemma. The RLS converges much faster than the LMS but still requires a data record length of approximately  $(2N)$  samples [30].

- 
4. *Cancellation of Repeater Jammers.* The operation of the minimum variance beamformer derives from the array correlation matrix which represents the mix of interferences (jammers, clutter, etc.) and thermal noise. The depth of cancellation of any particular source is reciprocal to its power; stronger interference sources are allocated deeper nulls. In some cases it may be desired to decouple the null depth from the source's power. For example a low power repeater jammer, mimicking the desired signal, could pass with little attenuation through the array only to be enhanced by the signal matched filter.

## CHAPTER 3

### ADAPTIVE RADAR METHODS

The airborne radar problem is two-dimensional with the radar returns a function of both angle and time. Airborne radars utilize velocity information (contained in the Doppler phase history) to discriminate between target and clutter. Radars are generally classified into one of three pulse repetition frequency (PRF) types: low, high, and medium. This classification is based on the range-Doppler operation. The low PRF radar provides unambiguous range measurements but, due to low sampling rate, it provides ambiguous Doppler information. The high PRF radar provides unambiguous Doppler information, but due to the higher sampling rate, it provides ambiguous range measurements. For many airborne applications the medium PRF radar, which is ambiguous in both range and Doppler domains, offers the best compromise solution, [37]. Adaptive space-time processing is particularly important for medium PRF radars, since it is the only way to simultaneously satisfy the conflicting demands of low antenna sidelobes for clutter reduction and placement of nulls for directional interference suppression.

The areas of adaptive nulling, beamforming and spectral estimation are characterized by similar mathematical models. Hence, it comes as no surprise that some adaptive nulling methods bear similarities to spectral estimation techniques. The last decade has seen widespread development of so-called superresolution spectral estimation techniques. They owe their name to their capability to resolve frequencies beyond the resolution limit suggested by the data time aperture. Exploiting model similarities, spectral estimation techniques have been tailored to solve direction finding problems [38], [39], [29]. Eigenanalysis based methods have seen extensive application to spectral estimation and direction finding problems. However, few researchers have tried to exploit eigenanalysis for interference cancellation. The eigencanceler is a new eigenanalysis based technique, motivated by approaches taken in spectral estimation and direction finding and developed for interference cancellation.

The eigencanceler provides simultaneous rejection of both clutter and directional interferences by adaptive processing in the spatial and Doppler domains. The eigencanceler uses eigendata to suppress clutter and directional interferences while minimizing noise contributions and maintaining specified beam pattern constraints. The method was originally suggested by the author for suppression of directional narrowband interferences [40], [24]. This chapter extends the eigencanceler to the space-time problem and explores its application to airborne radar.

#### 3.1 The Eigencanceler

In this section we present some important properties of the space-time correlation matrix. We subsequently formulate the optimization criteria for the Eigencanceler, provide the solutions weight vectors and develop the performance analysis for a simple case.

### 3.1.1 Eigenstructure of the Correlation Matrix

In the radar problem the desired signal is present only part of the time (corresponding to the pulses returned from the target). Considerable simplification can be achieved if the interferences are estimated when the signal is not present. This corresponds to collecting clutter and jammer data from neighboring range cells. For this case the stacked array vector  $\mathbf{x}(t)$  is a superposition of jammer signals  $\mathbf{j}(t)$ , clutter  $\mathbf{c}(t)$ , and thermal noise  $\mathbf{v}(t)$  only. The space-time correlation matrix can then be written,

$$\begin{aligned}\mathbf{R} &= E\{\mathbf{x}\mathbf{x}^H\} \\ &= \mathbf{R}_J + \mathbf{R}_c + \mathbf{R}_v\end{aligned}$$

where  $\mathbf{R}_J$ ,  $\mathbf{R}_c$ ,  $\mathbf{R}_v$  are the correlation matrices of the jammers, clutter, and noise, respectively. The reasonable assumption is made that the stochastic processes underlying the clutter echoes, jammer signals, and thermal noise are independent. Our objective is to make determinations on the eigenstructure of the space-time correlation matrix  $\mathbf{R}$ . To that end we will now examine each contributor in more detail.

1. *Jammers.* Jammer signals can be viewed as sources at discrete angles. In general we can model jammers to extend over the full range of baseband frequencies, since this range  $B_\nu$  is much smaller than the RF frequency at which the jammer signal originated. Using a continuous representation rather than the discrete approach in Section II-A, the jammers correlation matrix can be then written

$$\mathbf{M}_J = \sum_{\theta_i} \int_{B_\nu} S_{J,i}(\nu) \mathbf{d}(\theta_i, \nu) \mathbf{d}^H(\theta_i, \nu) d\nu \quad (3.1)$$

where the notation emphasizes the dependency of the position vector  $\mathbf{s}$  on the angle  $\theta_i$  and Doppler frequency  $\nu$  and  $S_{J,i}(\nu)$  is the power spectral density of the  $i$ -th jammer and at frequency  $\nu$ .

1. *Clutter.* The clutter extends over a sector of angles  $\Theta$ , and due to the flight geometry of the airborne radar, it covers a band of Doppler frequencies. The clutter correlation matrix is given by

$$\mathbf{R}_C = \int_{\Theta} \int_{B_\nu} S_C(\theta, \nu) \mathbf{s}(\theta, \nu) \mathbf{s}(\theta, \nu)^H s \nu s \theta \quad (3.2)$$

where  $S_C(\theta, \nu)$  is the power spectral density of the clutter at angle  $\theta$  and at frequency  $\nu$ .

2. *Noise.* Thermal noise is assumed white across the array and over the frequency band of interest. Stated another way, sensor outputs are uncorrelated to each other and uncorrelated to themselves at non-zero time lags. The resulting correlation matrix is the unity matrix scaled by the noise variance:

$$\mathbf{R}_v = \sigma_v^2 \mathbf{I} \quad (3.3)$$

It should be noted, however, that when the correlation matrix is estimated from the data the noise correlation matrix will not necessarily have the form shown in (3.3).

From the foregoing discussion it is evident that, in the airborne radar problem, clutter and jammer signals may be broadband spatially and temporally. The eigenstructure of the space-time correlation matrix of such signals has been considered by a number of authors, [41], [42]. The eigenanalysis of the space-time correlation matrix reveals a few large eigenvalues and a large number of small eigenvalues. The number of large (principal) eigenvalues is predicted by the Landau-Pollak theorem. The theorem states that the system energy is essentially concentrated in its largest  $r = 2BT + 1$  eigenvalues, where  $B$  is the bandwidth covered by the signals received by the array and  $T$  is the total durations of those signals across the array structure. Before evaluating the number of significant eigenvalues for the space-time array, it is interesting to consider the case of the simple linear space array. The  $n$ -th element output due to a single source at angle  $\theta$  and assuming half wavelength spacing between elements is given by:

$$x_n = e^{j2\pi \frac{\sin \theta}{2}(n-1)}$$

This signal may be regarded as samples of a sinusoid at frequency  $0.5\sin\theta$ . The bandwidth is essentially zero, hence the number of eigenvalues predicted by the theorem is just one, which turns out to actually be the case. A continuum of targets between angles  $\theta_1$  and  $\theta_2$  corresponds to a signal with bandwidth  $B = 0.5(\sin \theta_1 - \sin \theta_2)$ . The duration across the array is  $T = (N_s - 1)$ , hence the number of significant eigenvalues for this case is  $r = (N_s - 1)(\sin \theta_1 - \sin \theta_2) + 1$ . Another interpretation of the number  $r - 1 = 2BT$  is that it represents the number of cycles advanced across the array by the highest frequency component relative to the lowest frequency component. This number is clearly bounded by  $(N_s - 1)$ . This interpretation is also useful in evaluating the number of significant eigenvalues for the space-time array. These signals may be viewed as samples of sinusoids of the form

$$x_n = e^{j2\pi \left( \frac{\sin \theta}{2} + \mu \right)(n-1)}$$

where  $\mu = \nu T_r$  is the Doppler shift between two samples in the tapped delay line structure. The number of cycles advanced across the array structure is bound by  $(N_s - 1)$ , and the number of cycles advanced across the tapped delay line structure is  $(N_t - 1)$ . Hence, the number of significant eigenvalues of the space-time correlation matrix is bound by:

$$r \leq N_s + N_t - 1$$

This bound is independent of target distribution and is inherent to the way the space-time structure samples the received signals. This eigenanalysis is substantiated by experimental data [43]. Simulations of typical eigenspectra resulting from a clutter field and background noise are shown in Figure 3.1 for three different record sizes:  $N$ ,  $3N$ , and  $10N$  snapshots. The curves were obtained using the simulation model described in chapter 2.

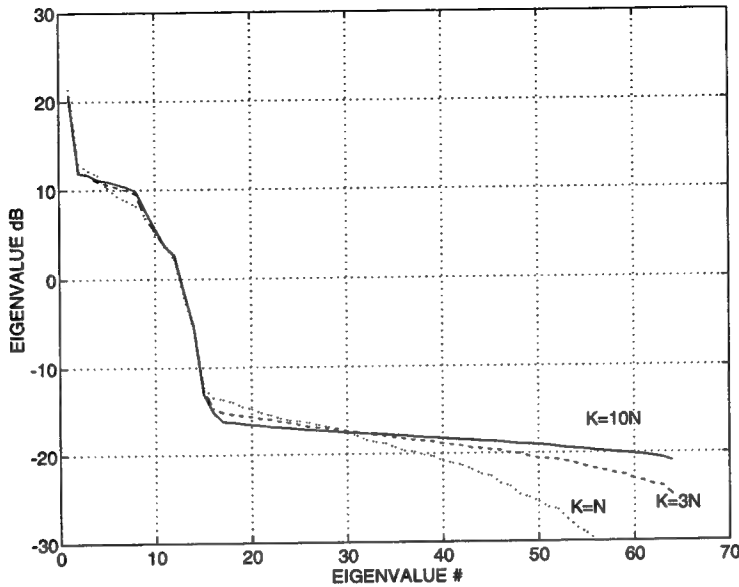


**Figure 3.1** Eigenvalues of the space-time covariance matrix

The total power of the jammer and clutter signals in the array is given by:

$$\begin{aligned} P &= \text{tr}[\mathbf{R}] \\ &= \sum_{i=1}^N \lambda_i \end{aligned}$$

where  $\lambda_i$  are the eigenvalues of  $\mathbf{R}$ . The eigenanalysis suggests that most of the power is concentrated in the largest  $r \leq (N_s + N_t - 1)$  eigenvalues. For arrays with  $r \ll N$ , a small number of eigenvalues contain all the information about interferences (jammers and clutter). It follows that the span of the eigenvectors associated with these significant eigenvalues includes all the position vectors that comprise the interference signals (see (3.1) and (3.2)). For that reason we refer to the dominant eigenvectors, as *interference eigenvectors*. The interference eigenvectors span the *interference subspace*. The rest of the  $N - r$  eigenvectors are referred to as *noise eigenvectors*. They span the *noise subspace*, and are orthogonal to the interference subspace. These properties are summarized as follows:

*Property 1.* The number of dominant eigenvalues of the space-time correlation matrix is bound by  $(N_s + N_t - 1)$ .

*Property 2.* The eigenvectors associated with the largest eigenvalues span the same algebraic subspace as the interference position vectors.

*Property 3.* The noise eigenvectors are orthogonal to the interference subspace.

The eigencanceler exploits those properties of the space-time correlation matrix to construct a weight vector that is very effective in cancelling the interferences.

### 3.1.2 Optimization Criteria

Let  $\mathbf{Q}_r$  denote the matrix representation of the interference subspace generated by the jammers+clutter contributions. The columns of  $\mathbf{Q}_r$  consist of the interference eigenvectors. Let  $\mathbf{Q}_v$  denote the matrix representation of the noise subspace. The columns of  $\mathbf{Q}_v$  consist of the noise eigenvectors. Since  $\mathbf{Q}_r^H \mathbf{Q}_v = 0$ , any weight vector in the noise subspace,  $\mathbf{w} \in \text{span}[\mathbf{Q}_v]$ , has the property of cancelling interferences. Additional requirements may be imposed on  $\mathbf{w}$  to optimize some array performance criterion. Two beamformer formulations are suggested:

1. The *minimum power eigencanceler* (MPE) is defined as the solution of the following optimization problem.

$$\min_{\mathbf{w}} \mathbf{w}^H \mathbf{R} \mathbf{w} \text{ subject to } \mathbf{Q}_r^H \mathbf{w} = 0 \text{ and } \mathbf{C}^H \mathbf{w} = \mathbf{f} \quad (3.4)$$

With the MPE, the beamformer output power is minimized under the space-frequency pattern constraints  $\mathbf{C}^H \mathbf{w} = \mathbf{f}$  and the additional constraint that the weight vector  $\mathbf{w}$  lies in the noise subspace. If the last constraint is removed we revert to the formulation of the minimum variance beamformer.

2. The *minimum norm eigencanceler* (MNE) is designed to minimize the norm of the weight vector while maintaining the linear and eigenvector constraints:

$$\min_{\mathbf{w}} \mathbf{w}^H \mathbf{w} \text{ subject to } \mathbf{Q}_r^H \mathbf{w} = 0 \text{ and } \mathbf{C}^H \mathbf{w} = \mathbf{f} \quad (3.5)$$

The solutions to the optimizations in (3.4) and (3.5) are provided in Appendix A. In particular, the minimum power eigencanceler is found to be:

$$\mathbf{w}_p = \mathbf{Q}_v \Gamma_v \mathbf{Q}_v^H \mathbf{C} \left[ \mathbf{C}^H \mathbf{Q}_v \Gamma_v \mathbf{Q}_v^H \mathbf{C} \right]^{-1} \mathbf{f} \quad (3.6)$$

where  $\Gamma_v$  is a diagonal matrix of the reciprocals of the noise eigenvalues. The minimum norm eigencanceler solution is given by:

$$\mathbf{w}_e = \mathbf{Q}_v \mathbf{Q}_v^H \mathbf{C} \left[ \mathbf{C}^H \mathbf{Q}_v \mathbf{Q}_v^H \mathbf{C} \right]^{-1} \mathbf{f} \quad (3.7)$$

an alternative expression of the MNE in terms of the dominant eigenvectors can be obtained by using the identity:  $\mathbf{Q}_r \mathbf{Q}_r^H + \mathbf{Q}_v \mathbf{Q}_v^H = \mathbf{I}$ .

$$\mathbf{w}_e = (\mathbf{I} - \mathbf{Q}_r \mathbf{Q}_r^H) \mathbf{C} \left[ \mathbf{C}^H (\mathbf{I} - \mathbf{Q}_r \mathbf{Q}_r^H) \mathbf{C} \right]^{-1} \mathbf{f} \quad (3.8)$$

A block diagram of the MNE is shown in Figure 3.2. The difference between the weight vectors of the MNE and the MPE is significant and will be discussed in the next section.

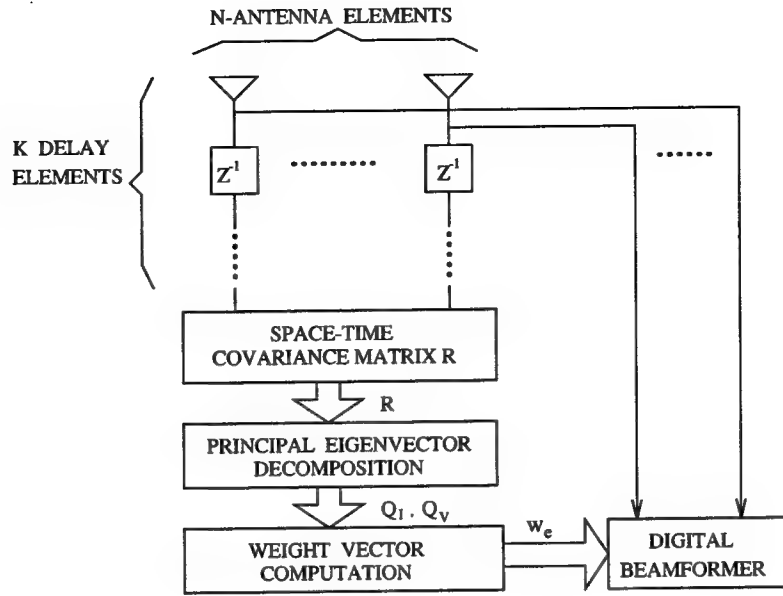


**Figure 3.2** The eigencanceler architecture

Also, note, that for white noise,  $\Gamma_v = 1/\sigma_v^2 \mathbf{I}$ , and the MPE filter in (3.6) reduces to the form of the MNE filter in (3.7). In most applications, however, the correlation matrix is estimated from the data and the noise correlation matrix will be in general different from a unity matrix. Since the two types of eigencanceler are suggested as alternatives of the minimum variance beamformer, it is useful to rewrite the MVB weight vector in (2.9) in terms of the eigenstructure of  $\mathbf{R}$ . Using the relation:  $\mathbf{R}^{-1} = \mathbf{Q}_r \Gamma_r \mathbf{Q}_r^H + \mathbf{Q}_v \Gamma_v \mathbf{Q}_v^H$ , where  $\Gamma_r$  is the diagonal matrix of the reciprocals of the interference eigenvalues, we get:

$$\mathbf{w}_o = (\mathbf{Q}_r \Gamma_r \mathbf{Q}_r^H + \mathbf{Q}_v \Gamma_v \mathbf{Q}_v^H) \mathbf{C} [\mathbf{C}^H (\mathbf{Q}_r \Gamma_r \mathbf{Q}_r^H + \mathbf{Q}_v \Gamma_v \mathbf{Q}_v^H) \mathbf{C}]^{-1} \mathbf{f} \quad (3.9)$$

From inspection of (3.9), (3.6), (3.7), or (3.8) the minimum variance beamformer weight vector is a superposition of vectors in the noise subspace  $\mathbf{Q}_v$ , as well as vectors in the interference subspace  $\mathbf{Q}_r$ , while the MPE and MNE weight vectors lie entirely in the noise subspace.

An illustrative geometrical interpretation of the MPE/MNE and the MVB is provided in Figure 3.3. The interference subspace and the noise subspace are represented by orthogonal planes. The weight vectors terminate on the constraint plane  $\Omega$ . The main difference is that  $\mathbf{w}_p/\mathbf{w}_e$  is orthogonal to the interference subspace, while  $\mathbf{w}_o$  is not.

### 3.1.3 Steady State Analysis

For the steady state analysis of the Eigencanceler's performance we consider the simple case of a single point jammer interference characterized by a stacked position vector  $\mathbf{s}_J$ . A single

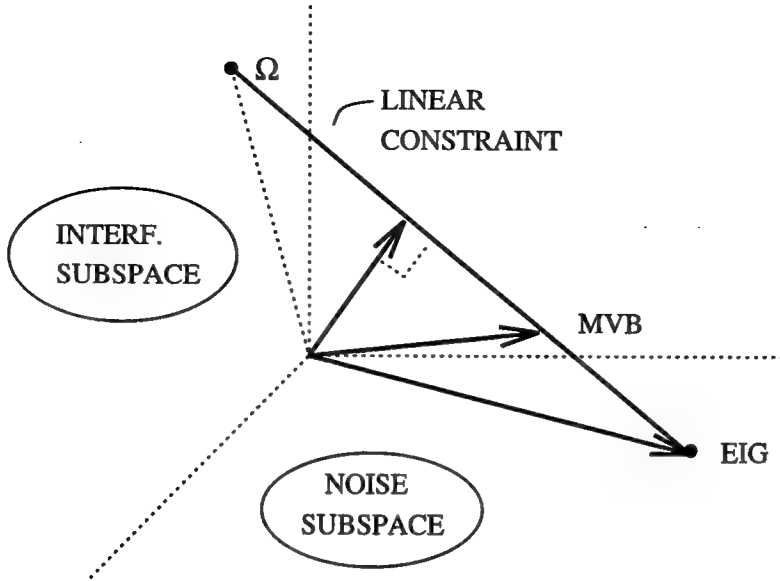


**Figure 3.3** Geometrical interpretation

linear constraint  $\mathbf{s}^H \mathbf{w} = 1$  is imposed. The space-time correlation matrix for this case is

$$\mathbf{R} = P_J \mathbf{s}_J \mathbf{s}_J^H + \sigma_v^2 \mathbf{I} \quad (3.10)$$

where  $P_J$  is the jammer power. In this ideal case the MPE and MNE provide identical weight vectors and the interference subspace is spanned by the single vector  $\mathbf{s}_J$ . Direct substitution of  $\mathbf{Q}_r = \mathbf{s}_J$ , and the unity gain constraint in (3.8) or (3.6) yields the eigencanceler weight vector:

$$\mathbf{w}_e = \frac{1}{1 - \|\rho\|^2} (\mathbf{I} - \mathbf{s}_J \mathbf{s}_J^H) \mathbf{s}_s \quad (3.11)$$

where  $\rho = \mathbf{s}_J^H \mathbf{s}_s$ . To calculate the minimum variance weight vector,  $\mathbf{R}$  is inverted using the matrix inversion lemma:

$$\mathbf{R}^{-1} = \frac{1}{\sigma_v^2} (\mathbf{I} - \gamma \mathbf{s}_J \mathbf{s}_J^H) \quad (3.12)$$

where  $\gamma = (P_J/\sigma_v^2)/(1 + P_J/\sigma_v^2)$ . Direct substitution of this result and the linear constraint, in (2.8) yields

$$\mathbf{w}_o = \frac{1}{1 - \gamma \|\rho\|^2} (\mathbf{I} - \gamma \mathbf{s}_J \mathbf{s}_J^H) \mathbf{s} \quad (3.13)$$

The interference gain is defined  $g_J = \mathbf{w}^H \mathbf{s}_J \mathbf{s}_J^H \mathbf{w}$ . While the eigencanceler has null response to the interference, the MVB interference gain is:

$$g_J = \frac{\|\rho\|^2 (1 - \gamma)^2}{(1 - \gamma \|\rho\|^2)^2} \quad (3.14)$$

Clearly when the jammer and desired signal position vectors are not orthogonal  $\rho \neq 0$  and  $g_J > 0$ , i.e. some interference is let in by the MVB. When  $P_J \gg \sigma_v^2$ ,  $\gamma \rightarrow 1$ , and the gain  $g_J \rightarrow 0$ .

Another merit figure of interest is the interference+noise output power,  $P_{I+N} = \mathbf{w}^H \mathbf{R} \mathbf{w}$ . For the eigencanceler we have:

$$\begin{aligned} P_{I+N,e} &= \mathbf{w}_e^H \mathbf{R} \mathbf{w}_e \\ &= \frac{\sigma_v^2}{1 - \|\rho\|^2} \end{aligned}$$

and for the MVB:

$$\begin{aligned} P_{I+N,o} &= \mathbf{w}_o^H \mathbf{R} \mathbf{w}_o \\ &= \frac{\sigma_v^2}{1 - \gamma \|\rho\|^2} \end{aligned}$$

Since  $0 \leq \gamma \leq 1$ , the total undesired power at the output of the eigencanceler is larger than for the MVB. This is hardly surprising since the MVB minimizes output power under a single linear constraint, while the eigencanceler minimizes output power with an extra constraint (orthogonality to interference subspace). The complete cancelation of the interference by the eigencanceler is traded off by the higher weight vector gain which, in turn, introduces more noise. However, we will show that this is not the case when the correlation matrix is estimated from the data.

### 3.1.4 Perturbation Analysis

When the correlation matrix is estimated from a finite number of snapshots the measurement noise causes perturbations in the values of the weight vectors. This perturbations affect differently the MVB, MPE and MNE weight vectors. The effect of perturbations on the eigenvalues and eigenvectors of the correlation matrix has been studied in [44] and [45]. The estimated correlation matrix can be written as

$$\widehat{\mathbf{R}} = \mathbf{R} + \Delta \mathbf{R}$$

where  $\Delta \mathbf{R}$  is a perturbation due to the measurement noise. Assuming a single linear constraint, the estimated MVB weight vector is given by:

$$\widehat{\mathbf{w}}_o = c_o \widehat{\mathbf{R}}^{-1} \mathbf{s} \quad (3.15)$$

where  $c_o$  is the scaling factor required to meet the constraint. For the MVB method it can be shown [46] that

$$E\{\gamma_o^2\} = \frac{1}{K} \quad (3.16)$$

where  $E\{\gamma_o^2\} = E\{\|\Delta \mathbf{w}_o\|^2 / \|\mathbf{w}_o\|^2\}$  is the normalized MVB weight vector norm variance and  $\Delta \mathbf{w}_o = \widehat{\mathbf{w}}_o - \mathbf{w}_o$ .  $K$  is the number of snapshots used in the estimation of the correlation matrix  $\mathbf{R}$ . This result holds for large  $K$ .

The minimum norm eigencanceler weight vector for the case of a single interference source and single linear constraint is given by:

$$\widehat{\mathbf{w}}_e = c_e [\mathbf{I} - \widehat{\mathbf{q}}_1 \widehat{\mathbf{q}}_1^H] \mathbf{s} \quad (3.17)$$

where  $c_e$  is a fixed scalar and  $\widehat{\mathbf{q}}_1$  is the eigenvector associated with the largest eigenvalue  $\widehat{\lambda}_1$ . It can be shown that for this case the error variance is given by [46]:

$$E\{\gamma_e^2\} \simeq \frac{1}{K} \frac{\lambda_{\min}(\mathbf{R})}{\lambda_{\max}(\mathbf{R})} \quad (3.18)$$

where  $E\{\gamma_e^2\} = E\left\{\|\Delta \mathbf{w}_e\|^2 / \|\mathbf{w}_e\|^2\right\}$ ,  $\Delta \mathbf{w}_e = \hat{\mathbf{w}}_e - \mathbf{w}_e$ , and  $\hat{\mathbf{w}}_e$  is the MNE weight vector obtained from the eigendecomposition of the estimated correlation matrix  $\widehat{\mathbf{R}}$ . Comparison of the error variances for the minimum variance beamformer and the minimum norm Eigencanceler, expressions (3.16) and (3.18) respectively, reveals a much lower variance for the Eigencanceler. This robustness explains the superior performance exhibited by the Eigencanceler.

An estimate of the error variance for the minimum power Eigencanceler, a single interference source and a single linear constraint, can be obtained by rewriting (3.6) as

$$\hat{\mathbf{w}}_p = c_p \left[ \widehat{\mathbf{R}}^{-1} - \hat{\lambda}_1^{-1} \hat{\mathbf{q}}_1 \hat{\mathbf{q}}_1^H \right] \mathbf{s} \quad (3.19)$$

Using (3.15) and (3.17) with (3.19), we can write  $\hat{\mathbf{w}}_p$  as a linear combination of the MVB and MNE weight vectors:

$$\hat{\mathbf{w}}_p = c_1 \hat{\mathbf{w}}_o - c_2 \hat{\mathbf{w}}_e + c_3 \mathbf{s}$$

The MPE weight vector sensitivity to perturbations is consequently controlled by  $\hat{\mathbf{w}}_o$  and does not possess the robustness shown by the MNE method. The simulations presented in the next section substantiate the results of the perturbation analysis by showing that the MNE is superior in performance to the MVB and MPE.

### 3.2 Simulations

For programming convenience we considered a linear uniform array with  $N_s = 8$  elements, spaced at half wavelength. Each array channel consisted of an FIR filter with  $N_t = 8$  taps. The sampling frequency was normalized to 1. The radar waveform was assumed narrowband, i.e. effectively constant over the propagation time across the array. We considered a forward looking airborne radar with a normalized platform velocity of 0.4. Hence ground clutter at boresight appears approaching at relative velocity 0.4. Radial velocities of other clutter returns depend on their azimuth angle. The clutter was assumed to extend over the angular sector -60 to +60 degrees. The clutter returns were simulated by spreading at random 60 scatterers in this angular sector. The clutter echoes were modeled as independent random variables, drawn from a random complex Gaussian distribution, with zero mean, and variance determined by the clutter-to-noise (CNR) parameter. We assumed the clutter sources uncorrelated to each other and uncorrelated between snapshots. Each clutter scatterer at each snapshot was assumed coherent across the array sensors and across the filter taps. The CNR was calculated from the contribution of all clutter echoes. Note that clutter signals extend over intervals in both the frequency and spatial domains. The simulation also included two jammer signals. Both were modeled with a relative radial velocity of 0.8. One jammer was placed at 30 degrees and the other at 35 degrees, and their power was 10 and 20 dB above the noise level, respectively. For simplicity we modeled the jammers as sinusoids at carrier frequency. For all simulations, the array was steered at boresight, and the array weight vector was constrained to unity gain over the Doppler frequency sector [0.7, 0.9]. The sample correlation matrix was calculated using (2.6). The various weight vectors were computed using relations (2.9), (3.6), and (3.8), respectively.

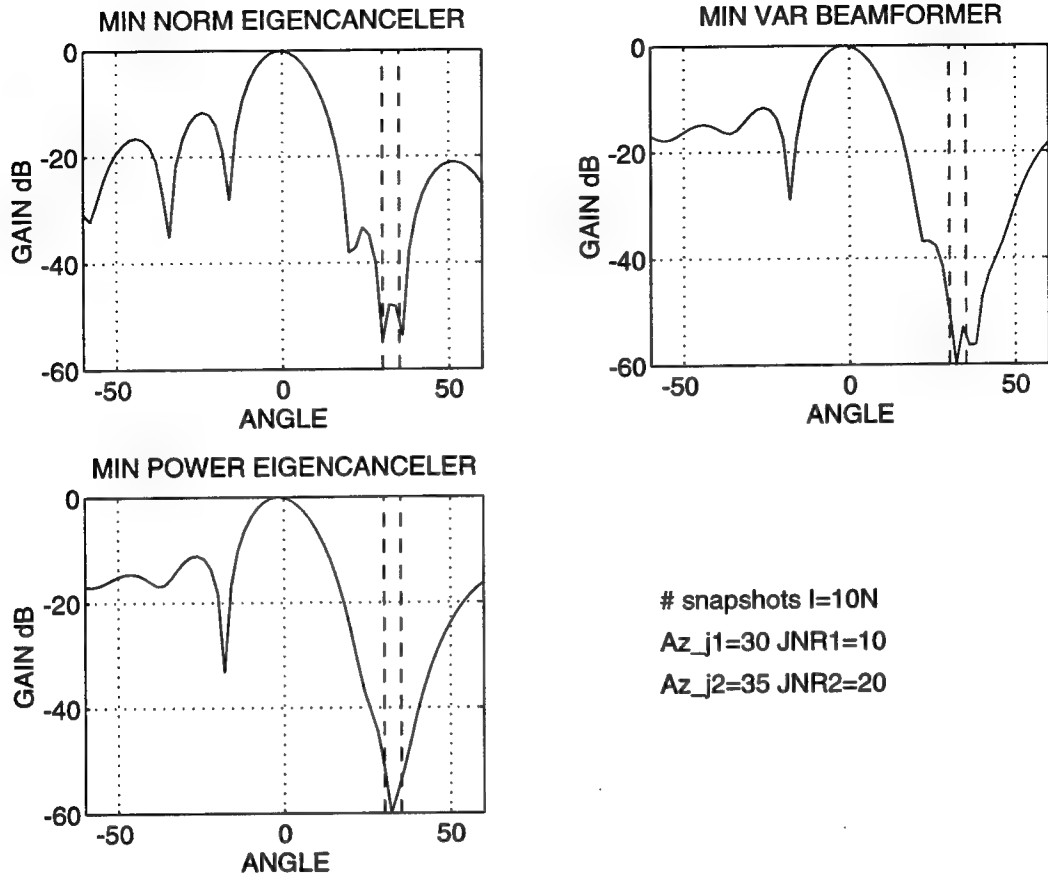


**Figure 3.4** Spatial patterns.  $K = 10N$ .

The results are grouped according to the number of samples  $K$ , used to estimate the correlation matrix  $\mathbf{R}$ . We looked at two illustrative cases: a large data record ( $K = 10N$ ), and the smallest record for which  $\mathbf{R}$  is still full rank, ( $K = N$ ). From Figure 3.1 it is seen that for the large data record the eigenspectra approaches that of the ideal correlation matrix (all noise eigenvalues are of equal size). For the small record, larger variations are observed in the spread of the noise eigenvalues.

*Large Record ( $K = 10N$ ):* Figure 3.4 provides the adapted antenna patterns for the MNE, MPE and MVB cancelers, respectively, for a sample run based on  $10N$  samples. The azimuth patterns have been calculated for Doppler frequency 0.8 (the center Doppler frequency of the jammers) and are indicative of the array's capability to cancel jammers. All cancelers place accurate nulls (jammers' azimuth shown by the vertical dashed lines). However, it can be observed that the minimum variance beamformer (MVB) and the minimum power eigencanceler (MPE) have a distorted sidelobe structure and a slightly biased mainbeam. For this large data record, the sample correlation matrix is close to the

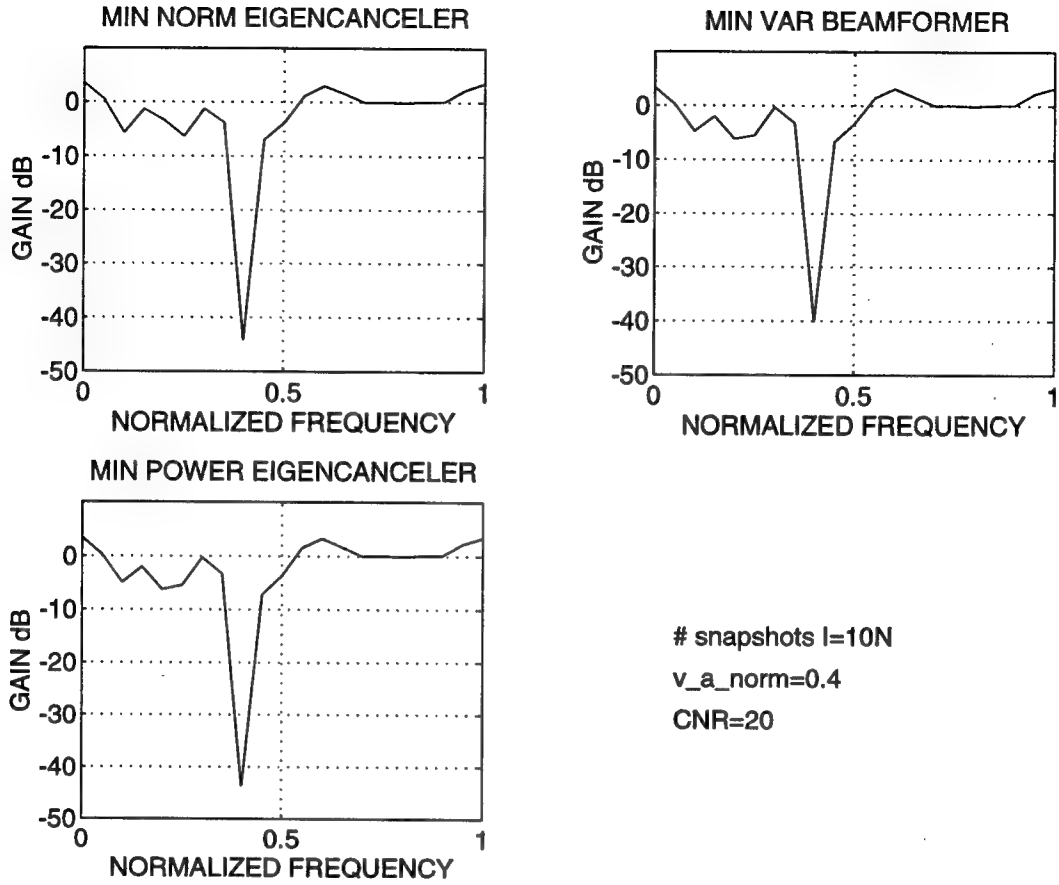


**Figure 3.5** Frequency response patterns.  $K = 10N$ .

true correlation matrix, and for high interference-to-noise ratios the differences between the three cancelers are not significant. In Figure 3.5 the MNE and MPE exhibit identical frequency response patterns (taken at zero look angle). The frequency response pattern indicates the clutter rejection performance with a notch being placed at the frequency where the clutter peaks. Significant differences among the methods become apparent for short data records.

*Short Record ( $K = N$ ):* For this case we show three angular and frequency patterns for each method resulting from three different runs. In Figure 3.6 the patterns for the MVB and the MPE methods are distorted. Note that the sidelobes are higher than the mainlobe. Yet, the MNE still manages to provide repeatable useful performance, with accurate nulls, low sidelobes, and a mainbeam. In Figure 3.7 it is shown that the MNE places a deeper null for clutter cancellation than any of the other methods. Again high sidelobes and fluctuating MPE and MVB patterns are evident. In Figure 3.8 we plot the clutter+noise improvement factor for the three methods and various input clutter-to-noise ratios. The MPE is indistinguishable from the MVB. The improvement factor for the minimum norm

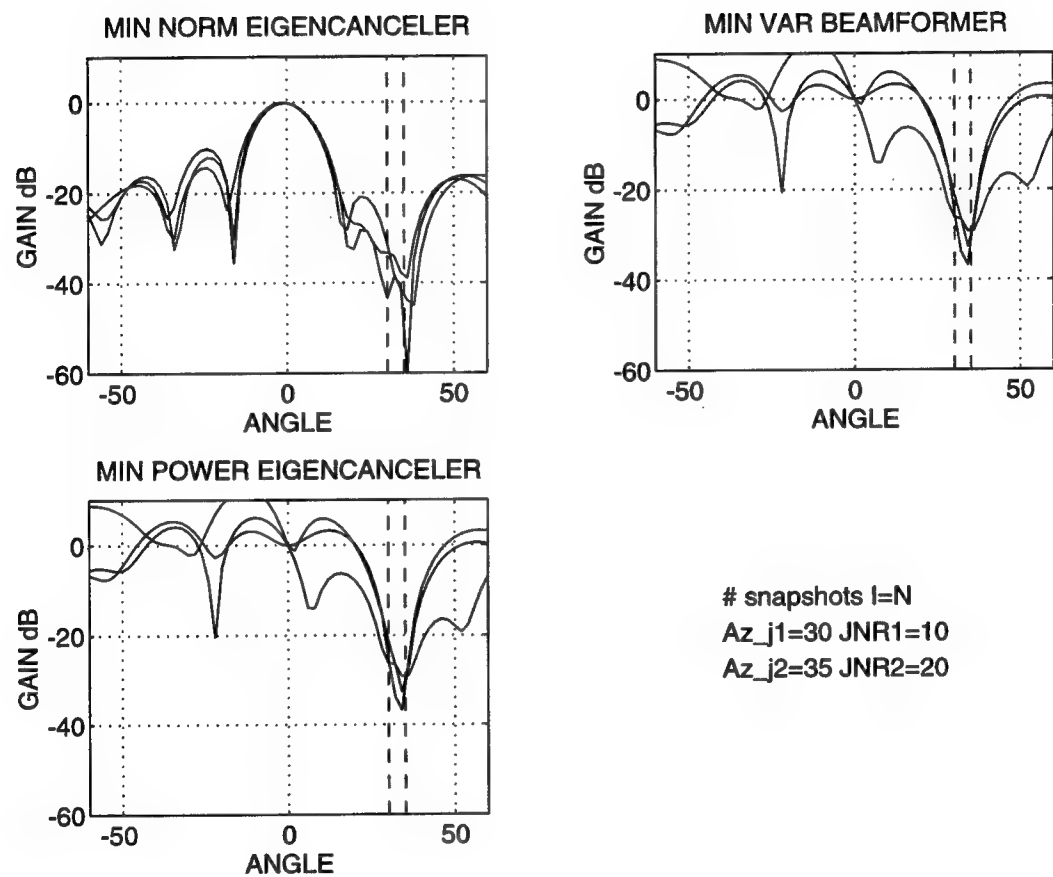


**Figure 3.6 Spatial patterns.  $K = N$ .**

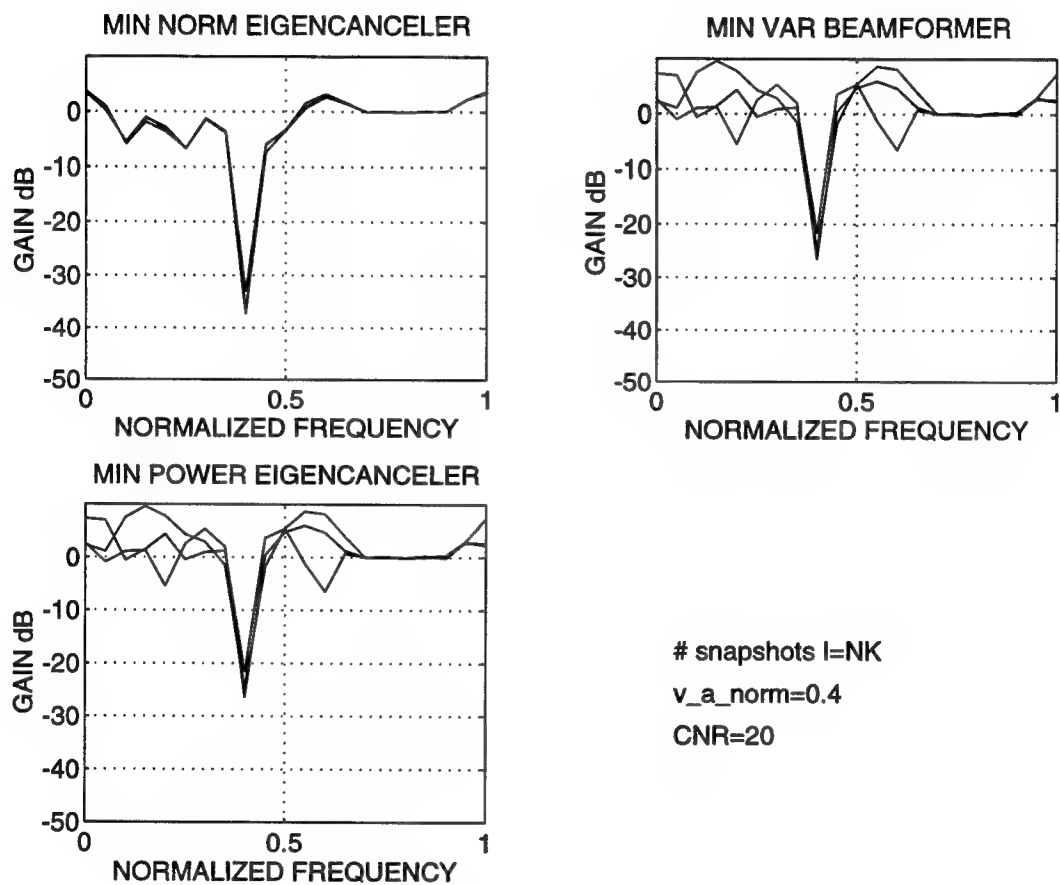


**Figure 3.7** Frequency response patterns.  $K = N$ .

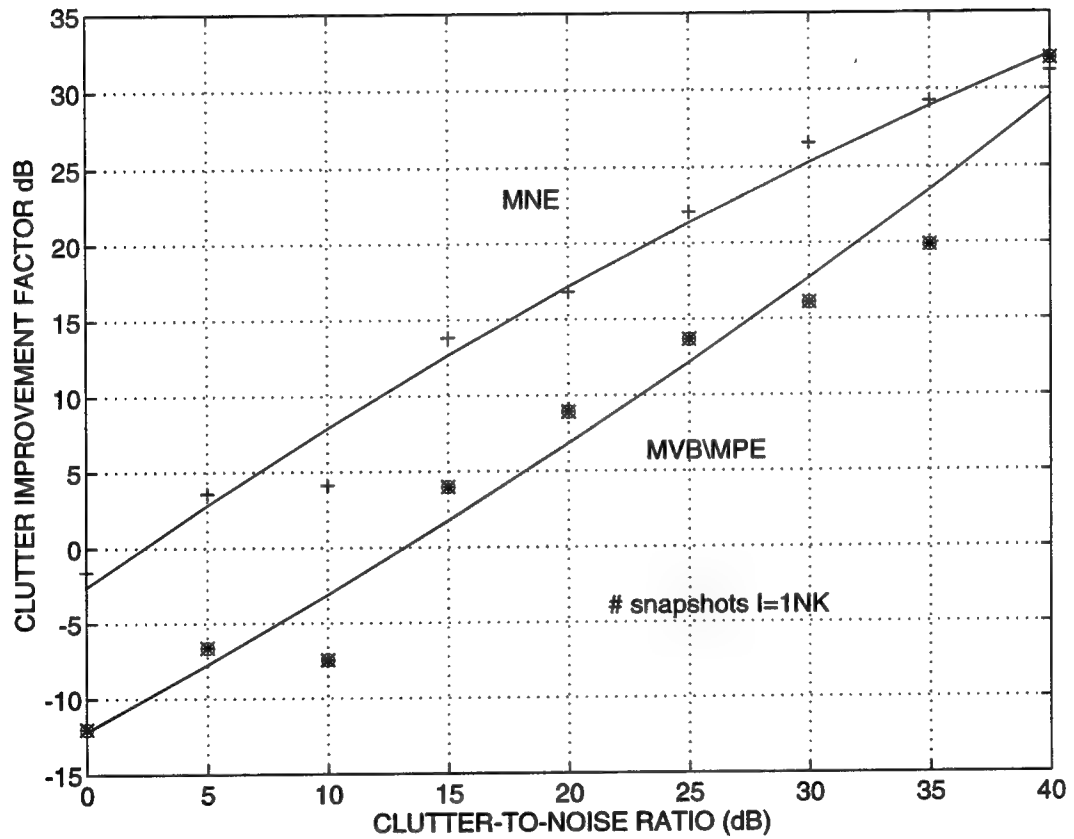
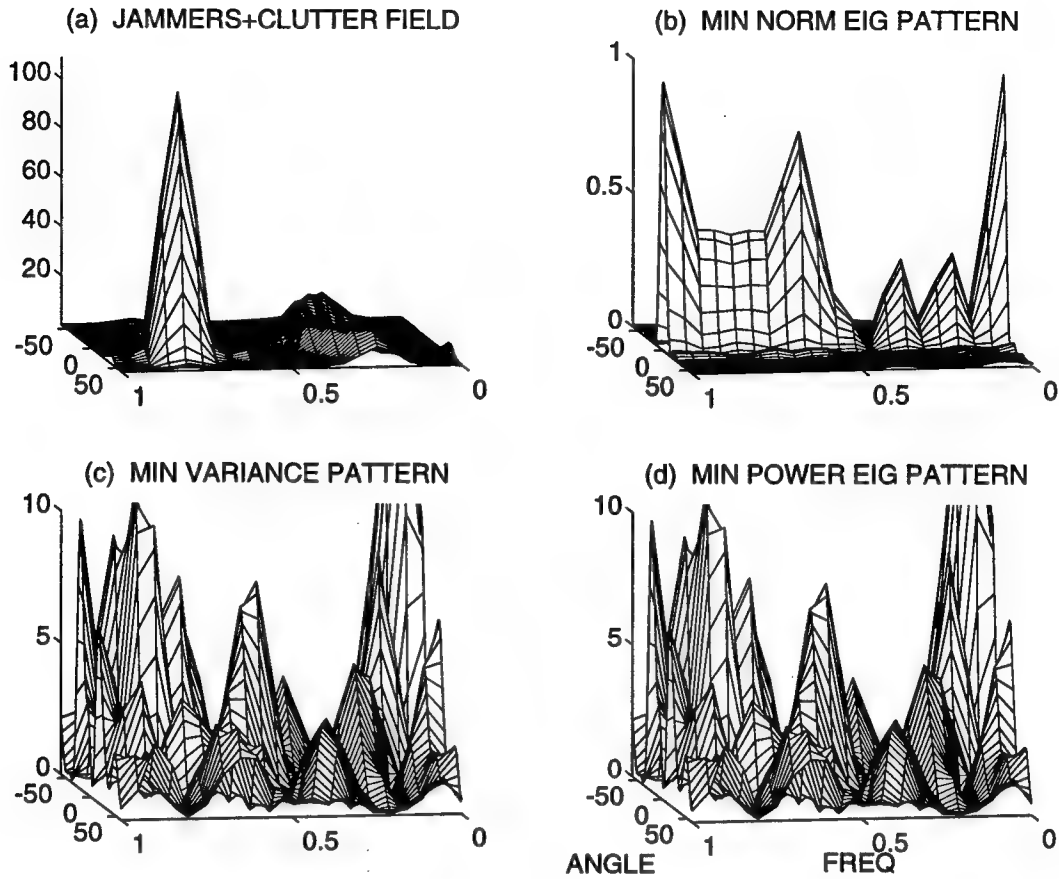


Figure 3.8 Improvement factors vs. CNR.  $K = N$ .



**Figure 3.9** 3D plots of the received signal and space-time patterns.  $K = N$ . Notice the “notch” in Figure (b) corresponding to the clutter “ridge” in (a).

eigencanceler shows a 5 to 10 dB improvement over the minimum variance beamformer. Figure 3.9 provides 3D plots of the received signals intensities (clutter and jammers) as well as the space-time patterns for each of the beamformers. The MNE clearly has the most useful pattern.

The simulation results presented in this section illustrate the robustness of the minimum norm eigencanceler method and its superior performance to the minimum variance beamformer.

### 3.3 Discussion

In this chapter we suggested a new approach, termed the eigencanceler, as an alternative method for adaptive radar processing. Two types of eigencanceler have been considered: the minimum power eigencanceler and the minimum norm eigencanceler. Each eigencanceler

has been formulated as a constrained optimization problem. To evaluate their performance, these methods were compared to the conventional minimum variance beamformer. Our analysis and simulations indicate that the minimum norm eigencanceler is a very promising alternative to the minimum variance beamformer. Particularly for short data records, the MNE provides superior clutter and jammers cancelation, lower variations in the pattern, lower distortion of the mainbeam, and can be carried out at a smaller computational cost than the MVB. Unlike the minimum norm eigencanceler, the minimum power eigencanceler has been shown to have properties similar to the conventional beamformer. The superior performance of the MNE is traced to the fact that the MNE uses only dominant eigenvectors in the formation of the weight vector, while the MPE and MVB use small noisy eigenvectors as well.

## CHAPTER 4

### ASYMPTOTIC DISTRIBUTION OF THE CONDITIONAL SIGNAL-TO-NOISE RATIO

Reed et al. suggested the use of the maximum likelihood estimate of the covariance matrix in lieu of the true covariance matrix, to detect a known signal vector in unknown colored noise [10]. This method is the SMI. While not optimal in any sense, this procedure has the advantage of being implemented as a simple linear combination of the array inputs.

The loss incurred by the estimation of the unknown colored noise can be evaluated from the conditioned signal-to-noise ratio (CSNR). The CSNR is defined as the ratio of the SNR achieved by the adaptive filter derived from the available data, to the optimal SNR (when the true data covariance matrix is available). As the data has a statistical model, the CSNR is a random variable. Reed et al. [10] determined its distribution, and used it to analyze the performance of the SMI method. This distribution turned out to have the remarkable property of being independent of the actual covariance matrix. In particular, they showed that if the signal vector dimension is  $N$ , the number of samples required to achieve performance within 3 dB of the optimal (i.e., when the true covariance matrix is known) is approximately  $K = 2N$ . Other authors provided alternative proofs or extended the SMI analysis [11], [12], and [13].

When the colored noise can be modeled as the aggregate of an interference with a low-rank covariance matrix and white noise, eigenanalysis can be exploited to design a detector with faster convergence than SMI. The detector is derived from the interference subspace and has been referred to as the *eigencanceler* [1]. The eigencanceler is formulated as a modified minimum variance beamformer. A related approach is the PCI method derived from a low-rank approximation to the data matrix [22]. The minimum variance beamformer minimizes the array output subject to a set of linear constraints [23]. The eigencanceler produces the minimum norm weight vector meeting the set of linear constraints, and the additional constraint of orthogonality to the interference subspace [24]. In the special case of a single linear constraint, the eigencanceler and PCI provide the same solution.

An expression for the probability density of the CSNR for the PCI method has been derived in [25]. It is shown therein that this probability density is the same as the probability density for the SMI method, except that the parameter  $(r + 1)$ , where  $r$  is the interference subspace rank, is substituted for the signal dimensionality. It results that the method converges within 3 dB of optimal for  $K \simeq 2r$ .

In this chapter, we suggest a new approach resulting in a different expression for the probability density of the CSNR for the eigenanalysis-based detector. The new probability density is derived from the asymptotic properties of the eigenvectors of the estimated covariance matrix. It is shown that, unlike the SMI method and the result in [25], the probability density depends on the true covariance matrix. Two simpler approximations, independent of the covariance matrix, are derived for a large interference-to-noise ratio. While not similar in form, these approximations produce numerical results close to those obtained using the probability density in [25]. It is hoped that the asymptotic analysis presented in this chapter provides new insights into the properties of reduced-rank methods.

#### 4.1 Distribution of the CSNR

Under both hypothesis models given in chapter 2,  $\mathbf{x}$  is a zero-mean,  $N \times 1$  complex-valued normal random vector with the  $N \times N$  covariance matrix  $\mathbf{R}_i$ ,  $i = 0, 1$ , where  $\mathbf{R}_0 = \mathbf{R}$  and  $\mathbf{R}_1 = \sigma_s^2 \mathbf{s} \mathbf{s}^H + \mathbf{R}$ , and the superscript stands for complex transposition. A distribution so defined is denoted  $\mathbf{x} \sim \mathcal{N}(\mathbf{0}, \mathbf{R}_i)$ . The matrix  $\mathbf{R}$  is further assumed to obey the model

$$\mathbf{R} = \mathbf{Q}_1 \Lambda_1 \mathbf{Q}_1^H + \sigma_v^2 \mathbf{Q}_2 \mathbf{Q}_2^H, \quad (4.1)$$

where  $\mathbf{Q}_1$  is the  $N \times r$  matrix of principal eigenvectors,  $\Lambda_1$  is the  $r \times r$  diagonal matrix of principal eigenvalues,  $\sigma_v^2$  is the variance of the white noise, and  $\mathbf{Q}_2$  is the  $N \times p$  matrix of noise eigenvectors, where  $p = N - r$ . The principal and noise eigenvectors are said to span the *interference* and *noise subspaces*, respectively. The eigencanceler weight vector for the case of a single steering vector linear constraint is given by [24, 1]:

$$\begin{aligned} \mathbf{w} &= (\mathbf{I}_N - \widehat{\mathbf{Q}}_1 \widehat{\mathbf{Q}}_1^H) \mathbf{s} \\ &= \widehat{\mathbf{Q}}_2 \widehat{\mathbf{Q}}_2^H \mathbf{s}, \end{aligned} \quad (4.2)$$

where  $\mathbf{I}_N$  is the  $N \times N$  unit matrix,  $\widehat{\mathbf{Q}}_1$  and  $\widehat{\mathbf{Q}}_2$  are the respective interference and noise subspaces in the spectral decomposition of the estimated covariance matrix,  $\widehat{\mathbf{R}} = \widehat{\mathbf{Q}}_1 \widehat{\Lambda}_1 \widehat{\mathbf{Q}}_1^H + \widehat{\mathbf{Q}}_2 \widehat{\Lambda}_2 \widehat{\mathbf{Q}}_2^H$ . The estimate  $\widehat{\mathbf{R}}$  is computed from a set of  $K$  independent interference  $N \times 1$  snapshot vectors  $\mathbf{x}_k$ ,  $k = 1, \dots, K$ , sometimes referred to as secondary data [10]:

$$\widehat{\mathbf{R}} = \frac{1}{K} \sum_{k=1}^K \mathbf{x}_k \mathbf{x}_k^H. \quad (4.3)$$

In this chapter we exploit some asymptotic properties of  $\widehat{\mathbf{R}}$ . Statisticians often make use of asymptotic analysis [47, 48], but this approach has found applications in signal processing as well [44, 45]. In reference [48], Gupta establishes that the asymptotic distribution of  $\mathbf{B} = \sqrt{K} [\widehat{\mathbf{R}} - \mathbf{R}]$  is normal as a direct result of the central limit theorem. We use the normality of  $\mathbf{B}$  to prove the following result.

**Lemma 1:** Let  $\widehat{\mathbf{R}} = \frac{1}{K} \sum_{k=1}^K \mathbf{x}_k \mathbf{x}_k^H$ , where  $\mathbf{x}_k$  are assumed to be zero-mean, circularly symmetric  $N$ -dimensional random vectors, i.i.d. with  $\mathcal{N}(\mathbf{0}, \mathbf{R})$  distribution. Then the limiting distribution of  $\mathbf{B} = \sqrt{K} [\widehat{\mathbf{R}} - \mathbf{R}]$ , as  $K \rightarrow \infty$ , has zero-means and covariances

$$E[b_{ij} b_{lm}^*] = \sigma_{il} \sigma_{jm}^*, \quad (4.4)$$

where  $\sigma_{im}$  are the elements of the matrix  $\mathbf{R}$ , and the Hermitian property of  $\mathbf{R}$  implies that  $\sigma_{il} = \sigma_{li}^*$ .

*Proof:* Let  $x_i(k)$  be the  $i$ -th component,  $i = 1, \dots, N$ , of the snapshot vector  $\mathbf{x}_k$ . From the definition of  $\sigma_{ij}$ ,  $E[x_i(k) x_j^*(k)] = \sigma_{ij}$ . The expected value of the product of four zero-mean Gaussian random variables is given by (for example [45, p.381]):

$$E[x_i(k) x_j^*(k) x_l^*(k) x_m(k)] = \sigma_{ij} \sigma_{lm}^* + \sigma_{il} \sigma_{jm}^*. \quad (4.5)$$

It results that

$$\begin{aligned} E[b_{ij}b_{lm}^*] &= K E \left[ \left( \frac{1}{K} \sum_{k=1}^K x_i(k) x_j^*(k) - \sigma_{ij} \right) \left( \frac{1}{K} \sum_{k=1}^K x_l^*(k) x_m(k) - \sigma_{lm}^* \right) \right] \\ &= \sigma_{il}\sigma_{jm}^*. \end{aligned} \quad (4.6)$$

In this section, the probability density of the CSNR is developed. The CSNR is the SNR obtained by the application of a specified weight vector  $\mathbf{w}$ , normalized by the SNR of the optimal case [10]:

$$\rho = \frac{|\mathbf{w}^H \mathbf{s}|^2}{\mathbf{w}^H \mathbf{R} \mathbf{w}} \frac{1}{\mathbf{s}^H \mathbf{R}^{-1} \mathbf{s}}. \quad (4.7)$$

Clearly, the CSNR is bounded,  $0 \leq \rho \leq 1$ . Substituting (4.2) in (4.7) we obtain

$$\rho = \frac{(\mathbf{s}^H \widehat{\mathbf{Q}}_2 \widehat{\mathbf{Q}}_2^H \mathbf{s})^2}{\mathbf{s}^H \widehat{\mathbf{Q}}_2 \widehat{\mathbf{Q}}_2^H \mathbf{R} \widehat{\mathbf{Q}}_2 \widehat{\mathbf{Q}}_2^H \mathbf{s}} \frac{1}{\mathbf{s}^H \mathbf{R}^{-1} \mathbf{s}} \quad (4.8)$$

for the eigencanceler. Our goal is to characterize the CSNR in (4.8) statistically. The perturbation analysis of the noise subspace  $\widehat{\mathbf{Q}}_2$  is required before the characterization of  $\rho$  can proceed.

#### 4.1.1 Perturbation Analysis of the Noise Subspace

The objective is to develop an expression for the estimated noise subspace  $\widehat{\mathbf{Q}}_2$ , in terms of the interference and noise subspaces of the true covariance matrix. The spectral decompositions of the true and estimated covariance matrices are

$$\mathbf{R} = \mathbf{Q} \Lambda \mathbf{Q}^H \quad (4.9)$$

and

$$\widehat{\mathbf{R}} = \widehat{\mathbf{Q}} \widehat{\Lambda} \widehat{\mathbf{Q}}^H. \quad (4.10)$$

respectively. Let the notation  $\mathbf{Q} = \{q_{ij}\}$  denote the matrix  $\mathbf{Q}$  with elements  $q_{ij}$ . For uniqueness,  $\mathbf{Q} = \{q_{ij}\}$  and  $\widehat{\mathbf{Q}} = \{\widehat{q}_{ij}\}$  are selected such that  $q_{ii}, \widehat{q}_{ii} > 0$ . Assume that the covariance matrix is estimated using relation (4.3).

Define the  $N \times N$  matrix

$$\tilde{\Lambda} = \mathbf{Q}^H \widehat{\mathbf{R}} \mathbf{Q}. \quad (4.11)$$

This matrix represents perturbed eigenvalues and is in general complex-valued. The perturbation from the true eigenvalues is given by

$$\mathbf{U} = \sqrt{K} (\tilde{\Lambda} - \Lambda). \quad (4.12)$$

The following theorem is formulated for the asymptotic distribution of the elements of  $\mathbf{U}$ :

**Theorem 1.** The limiting distribution of  $\mathbf{U}$  is normal with zero-mean and covariance

$$E[u_{ij}u_{lm}^*] = \lambda_i \lambda_j \delta_{il} \delta_{jm}, \quad (4.13)$$

where  $\lambda_i$  is an element of  $\Lambda$ , and  $\delta_{im}$  is the Kronecker delta.

*Proof:* The proof follows from Lemma 1 applied to the vectors  $\mathbf{z}_k = \mathbf{Q}^H \mathbf{x}_k$  and the normality of the limiting distribution of the matrix  $\mathbf{B}$ . From (4.11) and (4.12) and with  $\mathbf{B} = \sqrt{K} [\widehat{\mathbf{R}} - \mathbf{R}]$ , the matrix  $\mathbf{U}$  can be expressed as

$$\mathbf{U} = \mathbf{Q}^H \mathbf{B} \mathbf{Q}. \quad (4.14)$$

The normality of the limiting distribution of  $\mathbf{B}$  is maintained through the linear transformation  $\mathbf{Q}$ , hence the limiting distribution of  $\mathbf{U}$  is normal as well. Applying the Lemma 1, we have  $E[u_{ij} u_{lm}^*] = \mu_{il} \mu_{jm}^*$ , where  $\mu_{im}$  is an element of  $\mathbf{Q}^H \mathbf{R} \mathbf{Q} = \mathbf{\Lambda}$ . But  $\mathbf{\Lambda}$  is a non-negative diagonal matrix of the eigenvalues of  $\mathbf{R}$ , hence we have  $\mu_{il} = \lambda_i \delta_{il}$  and  $\mu_{jm}^* = \lambda_j \delta_{jm}$ . Q.E.D.

Define the  $N \times N$  matrix  $\mathbf{Y} = \mathbf{Q}^H \widehat{\mathbf{Q}}$ . Since both  $\mathbf{Q}$  and  $\widehat{\mathbf{Q}}$  are unitary, so is  $\mathbf{Y}$ . The perturbed eigenvectors can be expressed  $\widehat{\mathbf{Q}} = \mathbf{Q} \mathbf{Y}$ . From the definition of  $\mathbf{Y}$  and (4.11) we have  $\tilde{\mathbf{\Lambda}} = \mathbf{Q}^H \widehat{\mathbf{R}} \mathbf{Q} = \mathbf{Q}^H \widehat{\mathbf{Q}} \tilde{\mathbf{\Lambda}} \widehat{\mathbf{Q}}^H \mathbf{Q} = \mathbf{Y} \tilde{\mathbf{\Lambda}} \mathbf{Y}^H$ . Define

$$\mathbf{V} = \sqrt{K} (\mathbf{Y} - \mathbf{I}_N), \quad (4.15)$$

then  $\mathbf{Y} = \mathbf{I}_N + \frac{1}{\sqrt{K}} \mathbf{V}$ . From  $\tilde{\mathbf{\Lambda}} = \mathbf{Y} \tilde{\mathbf{\Lambda}} \mathbf{Y}^H$ , the previous relation and (4.12),  $\tilde{\mathbf{\Lambda}}$  can be written:

$$\begin{aligned} \tilde{\mathbf{\Lambda}} &= \mathbf{\Lambda} + \frac{1}{\sqrt{K}} \mathbf{U} \\ &= \left( \mathbf{I}_N + \frac{1}{\sqrt{K}} \mathbf{V} \right) \tilde{\mathbf{\Lambda}} \left( \mathbf{I}_N + \frac{1}{\sqrt{K}} \mathbf{V} \right)^H \\ &= \left( \mathbf{I}_N + \frac{1}{\sqrt{K}} \mathbf{V} \right) \left( \mathbf{\Lambda} + \frac{1}{\sqrt{K}} \mathbf{D} \right) \left( \mathbf{I}_N + \frac{1}{\sqrt{K}} \mathbf{V} \right)^H \\ &= \mathbf{\Lambda} + \frac{1}{\sqrt{K}} (\mathbf{V} \mathbf{\Lambda} + \mathbf{D} + \mathbf{\Lambda} \mathbf{V}^H) + \mathbf{M}, \end{aligned} \quad (4.16)$$

where  $\mathbf{D} = \sqrt{K} (\tilde{\mathbf{\Lambda}} - \mathbf{\Lambda})$  and  $\mathbf{M} = \frac{1}{K} (\mathbf{V} \mathbf{D} + \mathbf{D} \mathbf{V}^H + \mathbf{V} \mathbf{\Lambda} \mathbf{V}^H) + \frac{1}{K^{3/2}} \mathbf{V} \mathbf{D} \mathbf{V}^H$ . In the following we make use of the notation  $o(1/K)$ . The notation  $\mathbf{M} = o(1/K)$  is defined as  $\lim_{K \rightarrow \infty} \Pr[\mathbf{M} \leq (1/K) \mathbf{H}(K)] = 1$ , where the inequality is component-wise and  $\mathbf{H}(K)$  is bounded as  $K \rightarrow \infty$ . Note that according to this definition  $\mathbf{V}$ ,  $\mathbf{\Lambda}$ , and  $\mathbf{D}$  are  $o(1)$ , i.e., bounded as  $K \rightarrow \infty$ . Also note that the calculus of  $o(1/K)$  implies that if  $\mathbf{A}$  and  $\mathbf{B}$  are  $o(1/K)$ , so is  $\mathbf{A} + \mathbf{B}$ . Using the  $o(1/K)$  notion, we can define the symbol  $\cong$  to denote equality to the  $1/K$  order, i.e.,  $\mathbf{A} \cong \mathbf{B}$  implies that  $\mathbf{A} - \mathbf{B} = o(1/K)$ . The matrix  $\mathbf{M}$  in (4.16) is  $o(1/K)$ . If we neglect  $\mathbf{M}$  in the equation, the resulting equality holds to order  $1/K$  accuracy. A term by term comparison of the first and last lines in (4.16) yields:

$$\mathbf{U} \cong \mathbf{V} \mathbf{\Lambda} + \mathbf{D} + \mathbf{\Lambda} \mathbf{V}^H, \quad (4.17)$$

where the symbol  $\cong$  is used for asymptotic approximation.

According to the model assumed in (4.1), the  $N \times N$  matrix of eigenvalues  $\mathbf{\Lambda}$  can be partitioned

$$\mathbf{\Lambda} = \begin{pmatrix} \mathbf{\Lambda}_1 & \mathbf{0} \\ \mathbf{0} & \sigma_v^2 \mathbf{I}_p \end{pmatrix}. \quad (4.18)$$

Similarly, the  $N \times N$  matrix  $\mathbf{V}$  is partitioned into the following matrices:  $r \times r$   $\mathbf{V}_{11}$ ,  $r \times p$   $\mathbf{V}_{12}$ ,  $p \times r$   $\mathbf{V}_{21}$ ,  $p \times p$   $\mathbf{V}_{22}$ :

$$\mathbf{V} = \begin{pmatrix} \mathbf{V}_{11} & \mathbf{V}_{12} \\ \mathbf{V}_{21} & \mathbf{V}_{22} \end{pmatrix}. \quad (4.19)$$

Thus, if the elements of  $\mathbf{V}$  are denoted,  $v_{ij}$ , i.e.,  $\mathbf{V} = \{v_{ij}\}_{i=1,\dots,N, j=1,\dots,N}$ , then  $\mathbf{V}_{12} = \{v_{ij}\}_{i=1,\dots,r, j=r+1,\dots,N}$ . Let the matrix  $\mathbf{U}$  be partitioned in a similar way. We have from (4.17), (4.18), and (4.19), and noting that  $\mathbf{D} = \sqrt{K}(\hat{\Lambda} - \Lambda)$  is a diagonal matrix,

$$\mathbf{U}_{12} = \sigma_v^2 \mathbf{V}_{12} + \Lambda_1 \mathbf{V}_{21}^H. \quad (4.20)$$

To proceed, we show that  $\mathbf{V}_{12} + \mathbf{V}_{21}^H \cong \mathbf{0}$ . Partition  $\mathbf{Y}$  in a fashion similar to  $\mathbf{V}$ , i.e.  $\mathbf{Y} = \begin{pmatrix} \mathbf{Y}_{11} & \mathbf{Y}_{12} \\ \mathbf{Y}_{21} & \mathbf{Y}_{22} \end{pmatrix}$  with  $\mathbf{Y}_{11} r \times r$ ,  $\mathbf{Y}_{12} r \times p$ , etc. It follows from relation (4.15) that

$$\mathbf{Y} = \begin{pmatrix} \mathbf{I}_r + \frac{1}{\sqrt{K}} \mathbf{V}_{11} & \frac{1}{\sqrt{K}} \mathbf{V}_{12} \\ \frac{1}{\sqrt{K}} \mathbf{V}_{21} & \mathbf{I}_p + \frac{1}{\sqrt{K}} \mathbf{V}_{22} \end{pmatrix}. \quad (4.21)$$

Using the unitary property of the matrix  $\mathbf{Y}$  and the relation above, we have

$$\begin{aligned} \mathbf{I}_p &= \mathbf{Y}_{21} \mathbf{Y}_{21}^H + \mathbf{Y}_{22} \mathbf{Y}_{22}^H \\ &= \frac{1}{K} \mathbf{V}_{21} \mathbf{V}_{21}^H + \left( \mathbf{I}_p + \frac{1}{\sqrt{K}} \mathbf{V}_{22} \right) \left( \mathbf{I}_p + \frac{1}{\sqrt{K}} \mathbf{V}_{22} \right)^H. \end{aligned} \quad (4.22)$$

From the last relation it follows that

$$\begin{aligned} \left( \mathbf{I}_p + \frac{1}{\sqrt{K}} \mathbf{V}_{22} \right) \left( \mathbf{I}_p + \frac{1}{\sqrt{K}} \mathbf{V}_{22} \right)^H &= \mathbf{I}_p - \frac{1}{K} \mathbf{V}_{21} \mathbf{V}_{12}^H \\ &\cong \mathbf{I}_p. \end{aligned} \quad (4.23)$$

From the unitary property of  $\mathbf{Y}$  we also have

$$\begin{aligned} \mathbf{0} &= \mathbf{Y}_{11} \mathbf{Y}_{21}^H + \mathbf{Y}_{12} \mathbf{Y}_{22}^H \\ &= \frac{1}{\sqrt{K}} (\mathbf{V}_{12} + \mathbf{V}_{21}^H) + \frac{1}{K} (\mathbf{V}_{11} \mathbf{V}_{21}^H + \mathbf{V}_{12} \mathbf{V}_{22}^H) \\ &\cong \frac{1}{\sqrt{K}} (\mathbf{V}_{12} + \mathbf{V}_{21}^H), \end{aligned} \quad (4.24)$$

where  $o(1/K)$  terms were neglected to obtain the last relation. Using  $\mathbf{V}_{12} \cong -\mathbf{V}_{21}^H$  in (4.20) we obtain:

$$\mathbf{V}_{12} = -(\Lambda_1 - \sigma_v^2 \mathbf{I}_r)^{-1} \mathbf{U}_{12}. \quad (4.25)$$

The next theorem establishes the asymptotic distribution of the components of  $\mathbf{V}_{12}$ .

**Theorem 2.** The limiting distribution of the  $r \times p$  matrix  $\mathbf{V}_{12}$  is normal with zero-mean and

$$E[v_{ij} v_{lm}^*] = \frac{\lambda_i \sigma_v^2}{(\lambda_i - \sigma_v^2)^2} \delta_{il} \delta_{jm}, \quad (4.26)$$

where  $\mathbf{V} = \{v_{ij}\}_{i=1,\dots,N, j=1,\dots,N}$ , and  $\mathbf{V}_{12} = \{v_{ij}\}_{i=1,\dots,r, j=r+1,\dots,N}$ .

*Proof:* A term by term listing of (4.25) yields

$$v_{ij} = -\frac{u_{ij}}{\lambda_i - \sigma_v^2}, \quad (4.27)$$

for  $i = 1, \dots, r$  and  $j = r + 1, \dots, N$ . Therefore,

$$\begin{aligned} E[v_{ij}v_{lm}^*] &= \frac{E[u_{ij}u_{lm}^*]}{(\lambda_i - \sigma_v^2)^2} \\ &= \frac{\lambda_i \sigma_v^2}{(\lambda_i - \sigma_v^2)^2} \delta_{il} \delta_{jm}. \end{aligned} \quad (4.28)$$

The last relation was obtained applying Theorem 1. Q.E.D.

A consequence of Theorem 2 is that the elements of  $\mathbf{V}_{12}$  are asymptotically independent. The columns of the matrices  $\mathbf{Q}$  and  $\widehat{\mathbf{Q}}$  are the eigenvectors of  $\mathbf{R}$  and  $\widehat{\mathbf{R}}$ , respectively. Define the  $N \times r$  matrix  $\mathbf{Q}_1$  and the  $N \times p$ , ( $r + p = N$ ) matrix  $\mathbf{Q}_2$  such that  $\mathbf{Q} = [\mathbf{Q}_1 \mid \mathbf{Q}_2]$ . Note that  $\mathbf{Q}_1$  and  $\mathbf{Q}_2$  are orthogonal, i.e.,  $\mathbf{Q}_1^H \mathbf{Q}_2 = 0$ . The matrix  $\widehat{\mathbf{Q}}$  is partitioned similarly,  $\widehat{\mathbf{Q}} = [\widehat{\mathbf{Q}}_1 \mid \widehat{\mathbf{Q}}_2]$ . From the relations above, and from  $\widehat{\mathbf{Q}} = \mathbf{Q}\mathbf{Y}$  and (4.15), we find that

$$\begin{aligned} \widehat{\mathbf{Q}}_2 &= \mathbf{Q}_1 \mathbf{Y}_{12} + \mathbf{Q}_2 \mathbf{Y}_{22} \\ &= \mathbf{Q}_2 \left( \mathbf{I}_p + \frac{1}{\sqrt{K}} \mathbf{V}_{22} \right) + \frac{1}{\sqrt{K}} \mathbf{Q}_1 \mathbf{V}_{12}. \end{aligned} \quad (4.29)$$

Note that  $\mathbf{Q}_2 \left( \mathbf{I}_p + \frac{1}{\sqrt{K}} \mathbf{V}_{22} \right)$  and  $\mathbf{Q}_1$  are orthogonal, i.e.,  $\left( \mathbf{I}_p + \frac{1}{\sqrt{K}} \mathbf{V}_{22} \right)^H \mathbf{Q}_2^H \mathbf{Q}_1 = \mathbf{0}$ . The last expression provides the perturbation analysis of the estimated noise subspace  $\widehat{\mathbf{Q}}_2$  in terms of the true noise and interference subspaces,  $\mathbf{Q}_2$  and  $\mathbf{Q}_1$ , respectively. This relation is used to derive the probability density of the conditioned SNR.

#### 4.1.2 Computation of the PDF

Define the transformed noise subspace, the  $N \times p$  matrix  $\mathbf{C} = \mathbf{R}^{1/2} \widehat{\mathbf{Q}}_2$ , where the square root is defined such that  $\mathbf{R}^{1/2} \mathbf{R}^{1/2} = \mathbf{R}$ . Starting from the definition of the CSNR  $\rho$ , substituting  $\mathbf{R}^{-1/2} \mathbf{C} = \widehat{\mathbf{Q}}_2$ , and defining the transformed steering vector  $\mathbf{a} = \mathbf{R}^{-1/2} \mathbf{s}$ , we get

$$\begin{aligned} \rho &= \frac{\left( \mathbf{s}^H \widehat{\mathbf{Q}}_2 \widehat{\mathbf{Q}}_2^H \mathbf{s} \right)^2}{\mathbf{s}^H \widehat{\mathbf{Q}}_2 \widehat{\mathbf{Q}}_2^H \mathbf{R} \widehat{\mathbf{Q}}_2 \widehat{\mathbf{Q}}_2^H \mathbf{s}} \frac{1}{\mathbf{s}^H \mathbf{R}^{-1} \mathbf{s}} \\ &= \frac{\left( \mathbf{s}^H \mathbf{R}^{-1/2} \mathbf{C} \mathbf{C}^H \mathbf{R}^{-1/2} \mathbf{s} \right)^2}{\mathbf{s}^H \mathbf{R}^{-1/2} \mathbf{C} \mathbf{C}^H \mathbf{C} \mathbf{C}^H \mathbf{R}^{-1/2} \mathbf{s}} \frac{1}{\mathbf{s}^H \mathbf{R}^{-1} \mathbf{s}} \\ &= \frac{\left( \mathbf{a}^H \mathbf{C} \mathbf{C}^H \mathbf{a} \right)^2}{\mathbf{a}^H \mathbf{C} \mathbf{C}^H \mathbf{C} \mathbf{C}^H \mathbf{a}} \frac{1}{\mathbf{a}^H \mathbf{a}}. \end{aligned} \quad (4.30)$$

Substituting the unit magnitude vector  $\mathbf{b} = \mathbf{a} / |\mathbf{a}|$  for  $\mathbf{a}$  above and letting  $\mathbf{z} = \mathbf{C}^H \mathbf{b}$  yields

$$\rho = \frac{\left( \mathbf{z}^H \mathbf{z} \right)^2}{\mathbf{z}^H \mathbf{C}^H \mathbf{C} \mathbf{z}}. \quad (4.31)$$

Using the relation  $\mathbf{R}^{1/2} = \mathbf{Q}_1 \Lambda_1^{1/2} \mathbf{Q}_1^H + \sigma_v \mathbf{Q}_2 \mathbf{Q}_2^H$ , (4.29), and the orthogonality between  $\mathbf{Q}_1$  and  $\mathbf{Q}_2$ , we get

$$\mathbf{C} = \sigma_v \mathbf{Q}_2 \left( \mathbf{I}_p + \frac{1}{\sqrt{K}} \mathbf{V}_{22} \right) + \frac{1}{\sqrt{K}} \mathbf{Q}_1 \Lambda_1^{1/2} \mathbf{V}_{12}. \quad (4.32)$$

Expand the term  $\mathbf{z}$  using (4.32) and the orthogonality relations  $\mathbf{Q}_2^H \mathbf{Q}_2 = \mathbf{I}_p$  and  $\mathbf{Q}_2^H \mathbf{Q}_1 = 0$ :

$$\mathbf{z} = \sigma_v \left( \mathbf{I}_p + \frac{1}{\sqrt{K}} \mathbf{V}_{22} \right)^H \mathbf{Q}_2^H \mathbf{b} + \frac{1}{\sqrt{K}} \mathbf{V}_{12}^H \Lambda_1^{1/2} \mathbf{Q}_1^H \mathbf{b}. \quad (4.33)$$

We make the assumption that the projection of the steering vector on the true interference subspace is negligible with respect to its projection on the true noise subspace, i.e.,  $|\mathbf{Q}_1^H \mathbf{s}| \ll |\mathbf{Q}_2^H \mathbf{s}|$ . This assumption is reasonable and is just an expression of the requirement that the interference be received in the sidelobe region. Mainlobe interference is not addressed here. From the definition of vectors  $\mathbf{a}$  and  $\mathbf{b}$  we have:  $|\mathbf{Q}_1^H \mathbf{s}| = |\mathbf{Q}_1^H \mathbf{R}^{1/2} \mathbf{a}| = |\mathbf{a}| |\Lambda_1^{1/2} \mathbf{Q}_1^H \mathbf{b}| \geq |\mathbf{a}| |\sigma_v \mathbf{Q}_1^H \mathbf{b}|$ , where the last inequality follows from the observation that  $\sigma_v$  is smaller than any element of  $\Lambda_1^{1/2}$ . Likewise,  $|\mathbf{Q}_2^H \mathbf{s}| = |\mathbf{a}| |\sigma_v \mathbf{Q}_2^H \mathbf{b}|$ . Since,  $|\mathbf{a}| |\sigma_v \mathbf{Q}_1^H \mathbf{b}| \leq |\mathbf{Q}_1^H \mathbf{s}| \ll |\mathbf{Q}_2^H \mathbf{s}| = |\mathbf{a}| |\sigma_v \mathbf{Q}_2^H \mathbf{b}|$ , it follows that  $|\mathbf{Q}_1^H \mathbf{b}| \ll |\mathbf{Q}_2^H \mathbf{b}|$ . The vector  $\mathbf{b}$  has unity length, hence  $1 = \mathbf{b}^H \mathbf{b} = \mathbf{b}^H (\mathbf{Q}_1 \mathbf{Q}_1^H + \mathbf{Q}_2 \mathbf{Q}_2^H) \mathbf{b}$  implies that

$$\mathbf{b}^H \mathbf{Q}_2 \mathbf{Q}_2^H \mathbf{b} \cong 1. \quad (4.34)$$

With this result, and using (4.23), we have

$\mathbf{z}^H \mathbf{z} \cong \sigma_v^2 \mathbf{b}^H \mathbf{Q}_2 \left( \mathbf{I}_p + \frac{1}{\sqrt{K}} \mathbf{V}_{22} \right) \left( \mathbf{I}_p + \frac{1}{\sqrt{K}} \mathbf{V}_{22} \right)^H \mathbf{Q}_2^H \mathbf{b} \cong \sigma_v^2$ , and the numerator of (7.17) becomes

$$(\mathbf{z}^H \mathbf{z})^2 \cong \sigma_v^4. \quad (4.35)$$

To evaluate the denominator, first compute the  $p \times p$  matrix  $\mathbf{C}^H \mathbf{C}$ . From (4.32) and (4.23):

$$\begin{aligned} \mathbf{C}^H \mathbf{C} &= \sigma_v^2 \left( \left( \mathbf{I}_p + \frac{1}{\sqrt{K}} \mathbf{V}_{22} \right)^H \mathbf{Q}_2^H \mathbf{Q}_2 \left( \mathbf{I}_p + \frac{1}{\sqrt{K}} \mathbf{V}_{22} \right) + \frac{1}{K} \sigma_v^{-2} \mathbf{V}_{12}^H \Lambda_1 \mathbf{V}_{12} \right) \\ &\cong \sigma_v^2 \left( \mathbf{I}_p + \frac{1}{K} \sigma_v^{-2} \mathbf{V}_{12}^H \Lambda_1 \mathbf{V}_{12} \right). \end{aligned} \quad (4.36)$$

As a result, the denominator of (7.17) is evaluated:

$$\begin{aligned} \mathbf{z}^H \mathbf{C}^H \mathbf{C} \mathbf{z} &\cong \sigma_v^2 \mathbf{z}^H \left( \mathbf{I}_p + \frac{1}{K} \sigma_v^{-2} \mathbf{V}_{12}^H \Lambda_1 \mathbf{V}_{12} \right) \mathbf{z} \\ &\cong \sigma_v^2 \mathbf{z}^H \mathbf{z} + \frac{1}{K} \mathbf{z}^H \mathbf{V}_{12}^H \Lambda_1 \mathbf{V}_{12} \mathbf{z} \\ &\cong \sigma_v^4 + \frac{1}{K} \mathbf{z}^H \mathbf{V}_{12}^H \Lambda_1 \mathbf{V}_{12} \mathbf{z}, \end{aligned} \quad (4.37)$$

where we made use of the relation  $\mathbf{z}^H \mathbf{z} \cong \sigma_v^2$  (from (4.35)). Using (4.33) in (4.37) and neglecting terms  $o(1/K^{3/2})$  and higher, the term  $\frac{1}{K} \mathbf{z}^H \mathbf{V}_{12}^H \Lambda_1 \mathbf{V}_{12} \mathbf{z}$  is asymptotically equal

to  $\frac{1}{K}\sigma_v^2\mathbf{b}^H\mathbf{Q}_2\mathbf{V}_{12}^H\Lambda_1\mathbf{V}_{12}\mathbf{Q}_2^H\mathbf{b}$ . Thus we have

$$\mathbf{z}^H\mathbf{C}^H\mathbf{C}\mathbf{z} \cong \sigma_v^4 + \frac{1}{K}\mathbf{t}^H\mathbf{V}_{12}^H\Lambda_1\mathbf{V}_{12}\mathbf{t}, \quad (4.38)$$

where  $\mathbf{t} = \sigma_v\mathbf{Q}_2^H\mathbf{b}$  and  $\mathbf{t}^H\mathbf{t} \cong \sigma_v^2$  (see (4.34)). Write the  $r \times p$  matrix  $\mathbf{V}_{12}$  in terms of its rows:  $\mathbf{V}_{12} = \{\mathbf{v}_{ij}\}_{i=1,\dots,r; j=r+1,\dots,N} = \begin{pmatrix} \mathbf{v}_1^H \\ \vdots \\ \mathbf{v}_r^H \end{pmatrix}$ . Then the following expression is obtained:

$$\Lambda_1\mathbf{V}_{12}\mathbf{t} = \begin{pmatrix} \lambda_1\mathbf{v}_1^H\mathbf{t} \\ \vdots \\ \lambda_r\mathbf{v}_r^H\mathbf{t} \end{pmatrix}. \quad (4.39)$$

It follows that the CSNR can be written as

$$\begin{aligned} \rho &= \frac{1}{1 + \sigma_v^{-4}\frac{1}{K}\mathbf{t}^H\mathbf{V}_{12}^H\Lambda_1\mathbf{V}_{12}\mathbf{t}} \\ &= \frac{1}{1 + \frac{1}{K}\zeta}, \end{aligned} \quad (4.40)$$

where from (4.39),  $\zeta = \sigma_v^{-4}\mathbf{t}^H\mathbf{V}_{12}^H\Lambda_1\mathbf{V}_{12}\mathbf{t} = \sigma_v^{-4}\sum_{i=1}^r \lambda_i |\mathbf{v}_i^H\mathbf{t}|^2$ . From Theorem 2, the terms  $\mathbf{v}_i^H\mathbf{t}$  in the previous relation are complex Gaussian random variables, with  $E[\mathbf{v}_i^H\mathbf{t}] = 0$  and variance  $E[|\mathbf{v}_i^H\mathbf{t}|^2] = \mathbf{t}^H E[\mathbf{v}_i\mathbf{v}_i^H]\mathbf{t}$ . To find an expression for the variance, we first evaluate the  $p \times p$  covariance matrix  $E[\mathbf{v}_i\mathbf{v}_i^H]$ :

$$\begin{aligned} E[\mathbf{v}_i\mathbf{v}_i^H] &= E\left(\begin{array}{ccc} v_{i,r+1}v_{i,r+1}^* & \cdots & v_{i,r+1}v_{i,N}^* \\ \vdots & & \\ v_{i,N}v_{i,r+1}^* & & v_{i,N}v_{i,N}^* \end{array}\right) \\ &= \frac{\lambda_i\sigma_v^2}{(\lambda_i - \sigma_v^2)^2}\mathbf{I}_p, \end{aligned} \quad (4.41)$$

where the last relation is a direct consequence of Theorem 2. Using this relation we obtain

$$\begin{aligned} E[|\mathbf{v}_i^H\mathbf{t}|^2] &= \frac{\lambda_i\sigma_v^2}{(\lambda_i - \sigma_v^2)^2}\mathbf{t}^H\mathbf{t} \\ &\cong \sigma_v^4 \frac{\lambda_i}{(\lambda_i - \sigma_v^2)^2}, \end{aligned} \quad (4.42)$$

where we used  $\mathbf{t}^H\mathbf{t} \cong \sigma_v^2$ . Next we obtain the probability density of the Hermitian form  $\mu_i = \mathbf{v}_i^H\mathbf{t}\mathbf{t}^H\mathbf{v}_i$ . According to a lemma by Goodman [49], the characteristic function (c.f.) of the variate  $\mu_i$  with respect to the density of  $\mathbf{v}_i$  is given by

$$\Phi_{\mu_i}(\theta) = \frac{1}{\det(\mathbf{I}_p - j\theta\Sigma_i\mathbf{t}\mathbf{t}^H)}, \quad i = 1, \dots, r, \quad (4.43)$$

where  $\Sigma_i = E [\mathbf{v}_i \mathbf{v}_i^H]$ . From (4.42),  $\Sigma_i = \lambda_i \sigma_v^2 / (\lambda_i - \sigma_v^2)^2 \mathbf{I}_p$ . The determinant in the relation above can be computed by recognizing that the  $p \times p$  matrix  $(\mathbf{I}_p - j\theta \Sigma_i \mathbf{t} \mathbf{t}^H)$  is the sum of an identity matrix and the rank-one matrix  $j\theta \Sigma_i \mathbf{t} \mathbf{t}^H = j\theta \lambda_i \sigma_v^2 / (\lambda_i - \sigma_v^2)^2 \mathbf{t} \mathbf{t}^H$ . The only non-zero eigenvalue of the rank-one matrix is  $j\theta \lambda_i \sigma_v^2 / (\lambda_i - \sigma_v^2)^2 \mathbf{t}^H \mathbf{t} = j\theta \lambda_i \sigma_v^4 / (\lambda_i - \sigma_v^2)^2$ . Consequently, the matrix  $(\mathbf{I}_p - j\theta \Sigma_i \mathbf{t} \mathbf{t}^H)$  has an eigenvalue equal to  $(1 - j\theta \lambda_i \sigma_v^4 / (\lambda_i - \sigma_v^2)^2)$  and  $(p-1)$  unit eigenvalues. It follows that  $\det(\mathbf{I}_p - j\theta \Sigma_i \mathbf{t} \mathbf{t}^H) = 1 - j\theta \lambda_i \sigma_v^4 / (\lambda_i - \sigma_v^2)^2$ . From the last relation and (4.43) it follows that the c.f. of  $\mu_i$  is given by

$$\Phi_{\mu_i}(\theta) = (1 - j\bar{\mu}_i \theta)^{-1}, \quad (4.44)$$

where  $\bar{\mu}_i = \lambda_i \sigma_v^4 / (\lambda_i - \sigma_v^2)^2$ . This c.f. is that of an exponential random variable (also a non-normed chi-square variate with 2 degrees of freedom) and with mean  $E[\mu_i] = \bar{\mu}_i$ . The variate  $\nu_i = \sigma_v^{-4} \lambda_i \mu_i$  then has an exponential distribution with mean

$$\bar{\nu}_i = E[\nu_i] = \lambda_i^2 / (\lambda_i - \sigma_v^2)^2. \quad (4.45)$$

The random variable  $\zeta$  in (4.40) can now be written

$$\zeta = \sum_{i=1}^r \nu_i. \quad (4.46)$$

The statistical independence of the  $\nu_i$  variates follows from Theorem 2 and the independence of the vectors  $\mathbf{v}_i$ . Consequently, the c.f. of  $\zeta$  is given by

$$\begin{aligned} \Phi_\zeta(\theta) &= \prod_{i=1}^r \Phi_{\nu_i}(\theta) \\ &= \prod_{i=1}^r (1 - j\bar{\nu}_i \theta)^{-1}. \end{aligned} \quad (4.47)$$

The product appearing in the expression of the c.f. can be converted to a sum by applying the following partial fraction expansion:

$$\prod_{i=1}^r \frac{1}{1 - j\bar{\nu}_i \theta} = \sum_{i=1}^r \frac{\pi_i}{1 - j\bar{\nu}_i \theta}, \quad (4.48)$$

where  $\pi_i = \prod_{j=1, j \neq i}^r \bar{\nu}_j / (\bar{\nu}_j - \bar{\nu}_i)$ , [50]. The inverse Fourier transform of the c.f.  $\Phi_\zeta(\theta)$  yields the density of the random variable  $\zeta$  in the form of a sum of exponential densities weighted by the factors  $\pi_i$ :

$$f(\zeta) = \sum_{i=1}^r \frac{\pi_i}{\bar{\nu}_i} e^{-\zeta/\bar{\nu}_i}, \quad \zeta \geq 0. \quad (4.49)$$

It follows that the density of the CSNR  $\rho = (1 + (1/K) \zeta)^{-1}$  is given by the expression

$$f(\rho) = K \rho^{-2} \sum_{i=1}^r \frac{\pi_i}{\bar{\nu}_i} \exp\left(\frac{-K \left(\frac{1}{\rho} - 1\right)}{\bar{\nu}_i}\right), \quad 0 \leq \rho \leq 1. \quad (4.50)$$

### 4.1.3 Discussion

The expression for the CSNR probability density in (4.50) merits further consideration. It is observed that the probability density depends on the number of samples  $K$ , the number of dominant modes  $r$ , and the eigenvalues of the true covariance matrix (through the quantities  $\bar{\nu}_i$ ). Since the sum of the eigenvalues equals the total power in the received signal (interference+noise), it follows that the probability density is parameterized by the interference-to-noise ratio (INR). This result is different in form, as well as in substance, from the distribution of the SMI method in [10]. That expression, provided below for reference, is that of a beta distribution and is independent of the covariance matrix:

$$f(\rho) = \frac{\Gamma(K+1)}{\Gamma(N-1)\Gamma(K+2-N)} (1-\rho)^{N-2} \rho^{K+1-N}, \quad (4.51)$$

where  $\Gamma(K+1) = K!$  is the gamma function. Another interesting comparison is with the density of the PCI method in [25]. As mentioned in the introduction, the eigencanceler and the PCI method of reference [22] provide the same weight vector in the case of a single linear constraint. The density of PCI's CSNR is similar in form to that of the SMI method, with the difference that in (4.51) the signal dimensionality  $N$  is replaced by the quantity  $(r+1)$ , [25], i.e.,

$$f(\rho) = \frac{\Gamma(K+1)}{\Gamma(r)\Gamma(K+1-r)} (1-\rho)^{r-1} \rho^{K-r}. \quad (4.52)$$

Like SMI's density, this density is independent of the covariance matrix and the CNR. An additional difference between the densities of (4.50) and (4.51) is the asymptotic nature of the former. A closer look at expressions where the asymptotic approximation is applied (such as (4.16)) reveals that the nature of the approximation is to neglect  $o(1/\sqrt{K})$  terms relative to  $o(1)$  terms. However, this expression is later squared ((4.40)), thus the asymptotic approximation implies neglecting terms  $o(1/K)$  terms relative to  $o(1)$ . To achieve an order of magnitude ratio between the terms, the number of samples in data set needs to meet  $K \geq 10$ . Thus a modest number of samples is sufficient to satisfy the asymptotic approximation. Further analysis of the newly developed probability density, as well as comparisons with other densities and an assessment of the effect of the asymptotic approximations, are provided in the numerical results section.

### 4.1.4 Approximation for Large INR

An approximation to the expression in (4.50) can be obtained for the case of a large interference-to-noise ratio,  $\lambda_i \gg \sigma_v^2$ . Earlier in this section it was shown that the quantity  $\mu_i$  is an exponential variate (see (4.44)). For  $\lambda_i \gg \sigma_v^2$ , we have  $\bar{\mu}_i = \lambda_i \sigma_v^4 / (\lambda_i - \sigma_v^2)^2 \simeq \sigma_v^4 / \lambda_i$ . It follows that  $\bar{v}_i = \sigma_v^{-4} \lambda_i \bar{\mu}_i = 1$ . Then from (4.46),  $\zeta$  is the sum of  $r$  i.i.d., unit-mean, exponential variates; i.e.,  $\zeta$  has a gamma distribution with parameters  $r$  and 1. The density of  $\zeta$  is then given by

$$f(\zeta) = \frac{1}{\Gamma(r)} \zeta^{r-1} e^{-\zeta}, \quad \zeta \geq 0. \quad (4.53)$$

Using this density in conjunction with the relation between the variates  $\rho$  and  $\zeta$  in (4.40) yields the density for the CSNR in the case of large INR:

$$f(\rho) = \frac{K^r e^K}{\Gamma(r)} e^{-K/\rho} (1 - \rho)^{r-1} \rho^{-(r+1)}, \quad 0 \leq \rho \leq 1. \quad (4.54)$$

It should be noted that as  $\lambda_i/\sigma_v^2 \rightarrow \infty$ , (4.50)  $\rightarrow$  (4.54).

A further simplification can be obtained by keeping only the first two terms of the series  $(1 + \frac{1}{K}\zeta)^{-1} = \sum_{i=0}^{\infty} (-\zeta/K)^i$ :

$$\rho = \frac{1}{1 + \frac{1}{K}\zeta} \cong 1 - \frac{1}{K}\zeta. \quad (4.55)$$

The last formulation does not strictly guarantee that  $0 \leq \rho$ . However, since  $E[\zeta] = r$  and  $\text{var}[\zeta] = (2r)^2$ , then for  $K \gg r$ ,  $\rho$  is almost certain to be non-negative. The density of the CSNR is obtained from (4.53) and (4.55):

$$f(\rho) = \frac{K^r}{\Gamma(r)} e^{-K(1-\rho)} (1 - \rho)^{r-1}, \quad 0 \leq \rho \leq 1. \quad (4.56)$$

It should be noted that with the large INR approximation, the dependency on INR is not present in either (4.54) or (4.56). Finally, we note that if we define the CSNR loss,  $\gamma = 1 - \rho$ , then it follows that the probability density of the loss is given by the gamma function with parameters  $r$  and  $K$ :

$$f(\gamma) = \Gamma(r, K) = \frac{K^r}{\Gamma(r)} e^{-K\gamma} \gamma^{r-1}, \quad 0 \leq \gamma \leq 1. \quad (4.57)$$

The CSNR loss is thus distributed as the incomplete gamma function.

## 4.2 Numerical Results

Computer simulations were conducted to support the theory presented in the previous section. The simulation scenario consisted of distributed clutter, white Gaussian noise, and a space-time array. The clutter consisted of 120 point sources randomly distributed in the angular sector 0 - 20 degrees with respect to the array boresight. The array boresight was assumed perpendicular to the platform motion. The clutter signals were summed non-coherently to form the signal received at the array. The space-time processor was fed by an  $N_s = 8$  element linear array with  $N_t = 4$  tap delay lines at each element, resulting in a signal space dimensionality of  $N = N_s N_t = 32$ . The steering vector was pointed at 50 degrees and a normalized Doppler frequency of 0.4. The clutter map in angle-Doppler coordinates is shown in Figure 4.1. For this scenario, the interference subspace was found to have rank  $r = 4$ . The space-time covariance matrix was estimated from a specified number of snapshots of those signals ((4.3)), and weight vectors were derived for SMI and eigencanceler processors ((4.2) for the latter). The CSNR was then evaluated from (4.7). Maintaining the same scenario, the process was then repeated numerous times to yield independent realizations of the CSNR variate. The numerical results were compared to the theory as described below.

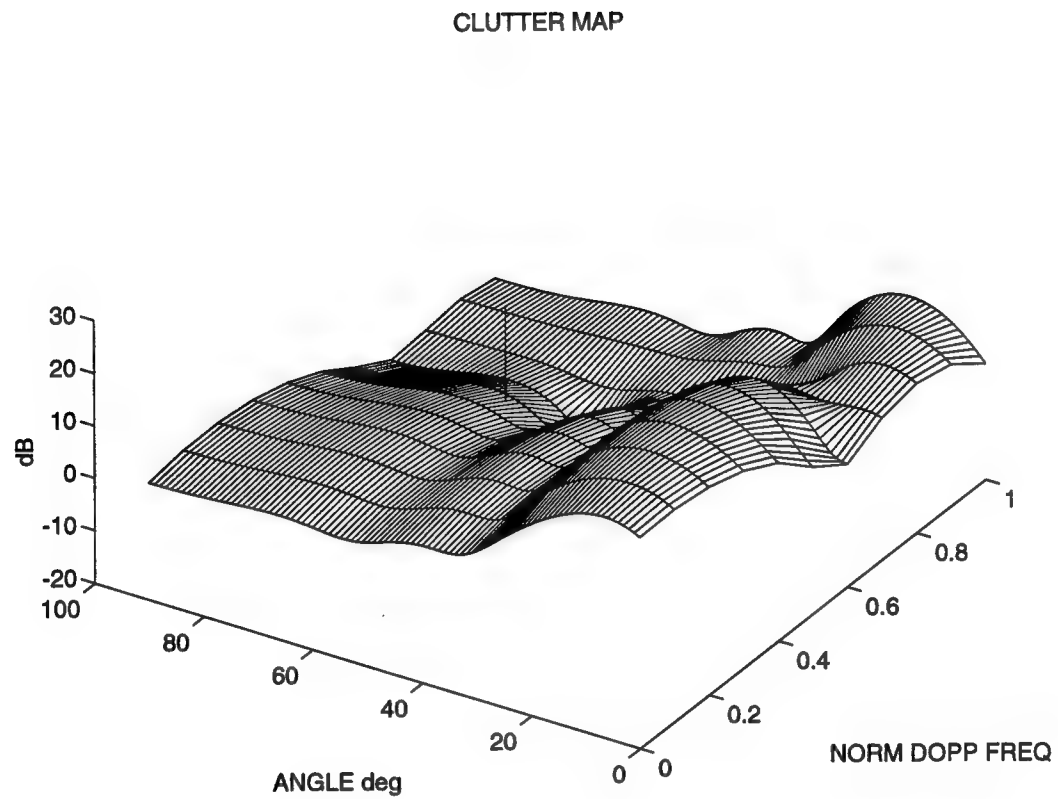


**Figure 4.1** Simulation clutter map. The vertical line indicates the steering vector.

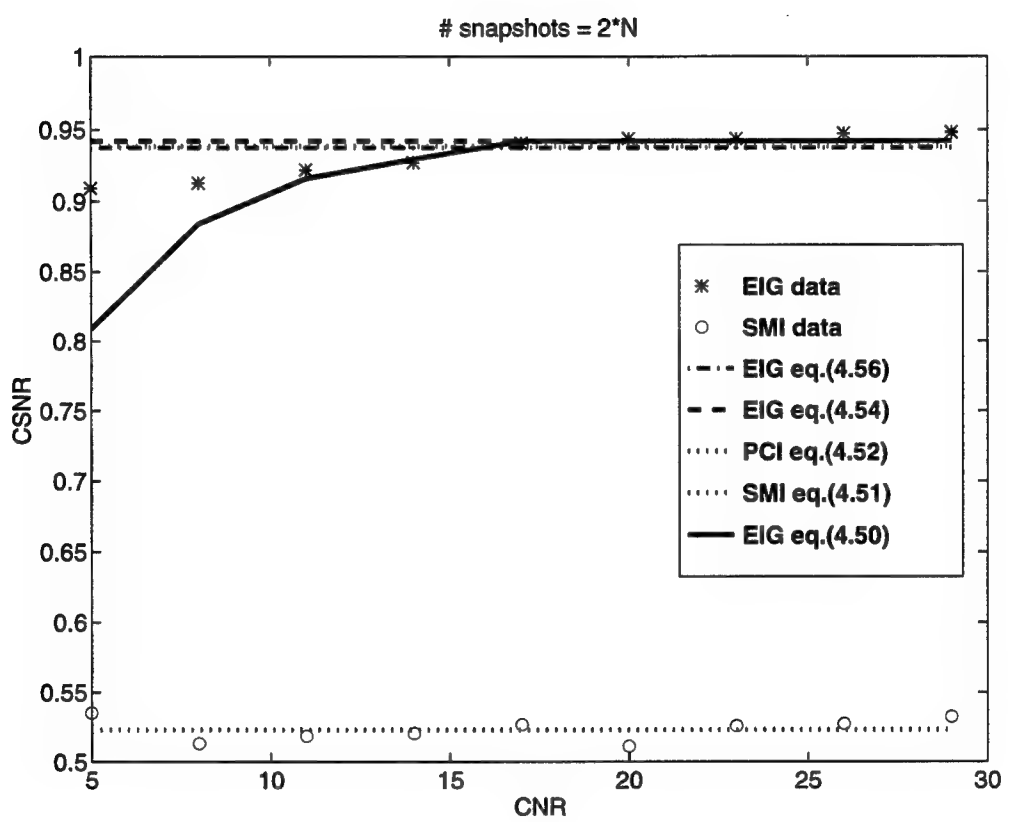


**Figure 4.2** The mean conditioned signal to noise ratio as a function of the clutter to noise ratio for covariance matrix estimates using  $K = 2N$  samples.

Figure 4.2 plots the mean CSNR for different clutter-to-noise ratios (CNR). The covariance matrix was estimated from  $K = 2N = 2N_s N_t = 64$  snapshots. For each CNR, the mean was computed from 100 runs. The simulation results are shown together with values of  $E[\rho]$  computed using numerical integration of the following densities: for the SMI, (4.51), and for the eigencanceler, (4.50), (4.54), and (4.56). Also shown are results obtained using the PCI density, (4.52). For this case (single linear constraint embodied by the steering vector), the PCI and eigencanceler methods produce the same weight vectors, and thus the same CSNR  $\rho$ . The objective is to evaluate the accuracy of the four probability density expressions for eigenanalysis-based processing ((4.50), (4.54), (4.56) and the PCI density). From the figure it can be seen that for  $\text{CNR} \geq 20$  dB, all four expressions provide a good representation of the data. The approximation in (4.56) and the PCI method provide almost indistinguishable mean values. For large CNR's, the expectations yielded by (4.50) and (4.54) are also indistinguishable, as they should be. However, the most interesting observation is that for  $\text{CNR} \leq 15$  dB, the approximations in (4.54) and (4.56) as well as the PCI expression, fail to represent the data. Expression (4.50), however, provides a better fit to the data, at least for  $10 \text{ dB} \leq \text{CNR} \leq 15$  dB. This observation supports the assertion that, unlike SMI processing, for eigenanalysis-based processing the CSNR is *not* independent of the covariance matrix. It is clearly evident in the figure that the CSNR of SMI-processed data is independent of the CNR, while the CSNR is CNR-dependent for the eigencanceler. It is also clear from the figure that the eigencanceler theory provides a lesser fit to the data for  $\text{CNR} \leq 10$  dB. That is due to the asymptotic nature of the expressions. Indeed, when the number of snapshots was increased to  $K = 3N = 3N_s N_t$ , Figure 4.3 shows that the expectation using the new probability density in eq. (4.50) represents the data down to  $\text{CNR} = 8$  dB.

Figure 4.4 shows the result of a further increase in the number of samples to  $K = 4N$ . The theory now provides a good fit to the data down to  $\text{CNR} = 5$  dB.

As noted above, the asymptotic approximations seem to have little adverse effects at  $\text{CNR} \geq 10$ . Further support to this can be found in Figures 4.5 and 4.6. Each of the data points in the figure is an average of 100 Monte-Carlo runs. In Figure 4.5 the mean CSNR is shown as a function of the number of snapshots  $K$ , at  $\text{CNR} = 10$  dB.

The new probability density provides an accurate fit to the data, down to a sample size of  $K = N$  samples. The two approximations to the probability density, as well as the PCI density, show a slight bias. The SMI density provides a good fit as well. For  $K < N$  the SMI cannot be applied, since the estimated covariance matrix  $\widehat{\mathbf{R}}$  becomes singular. Figure 4.6 shows the mean CSNR of the eigencanceler only, as a function of the number of samples  $K$ , down to  $K = N/16$ .

Again there is good agreement between the new probability density and the data. The approximation given by (4.54) maintains only a slight bias. The bias of approximation (4.56) is slightly larger, while the PCI density is more significantly off at very low number of samples. We can conclude from these plots that at  $\text{CNR} \geq 10$ , (4.50) provides a very accurate description of the data down to a very low number of samples.

Figure 4.7 provides the histograms of  $\rho$  for the SMI and the eigencanceler produced by 10,000 runs at  $\text{CNR} = 10$  dB. The number of samples used to estimate each covariance matrix was  $K = 4N$ .

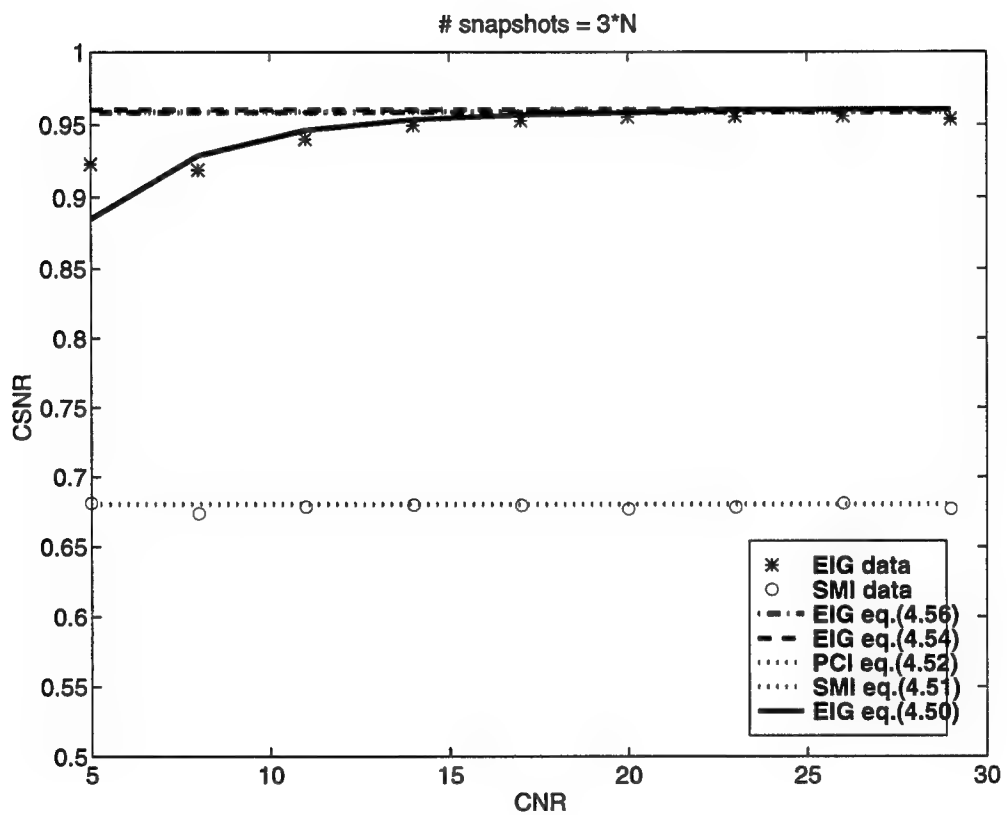


**Figure 4.3** The mean conditioned signal to noise ratio as a function of the clutter to noise ratio for covariance matrix estimates using  $K = 3N$  samples.

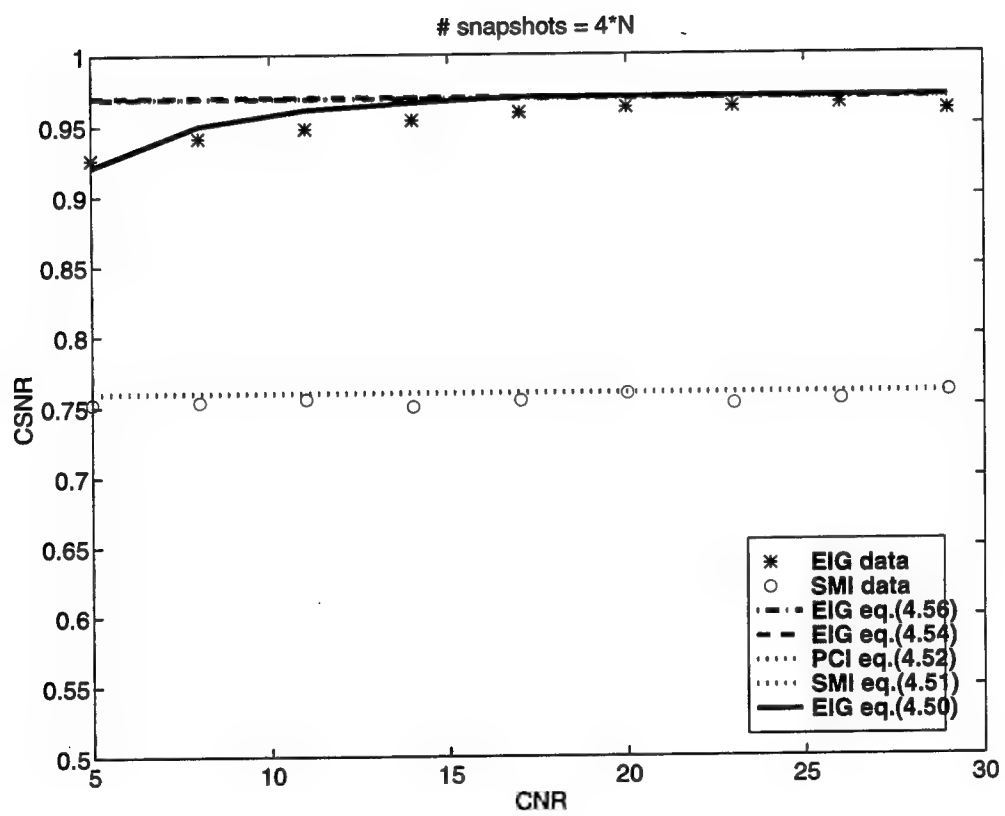


**Figure 4.4** The mean conditioned signal to noise ratio as a function of the clutter to noise ratio for covariance matrix estimates using  $K = 4N$  samples.

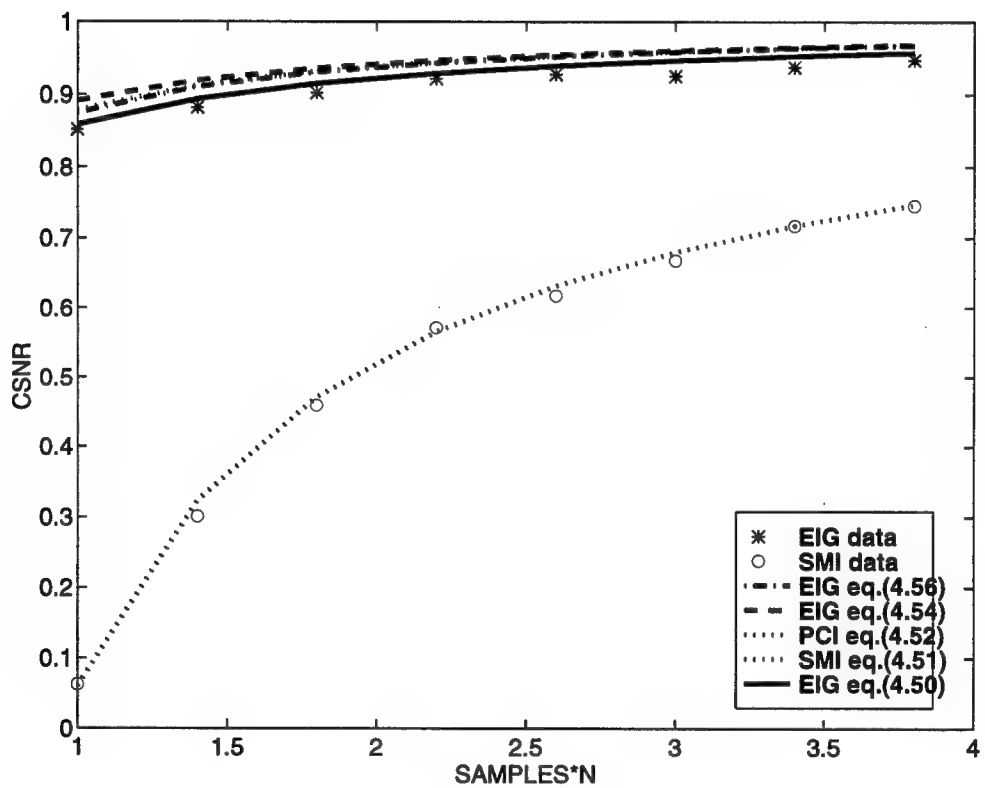


**Figure 4.5** The mean conditioned signal to noise ratio as a function of the number of snapshots for CNR = 10 dB.

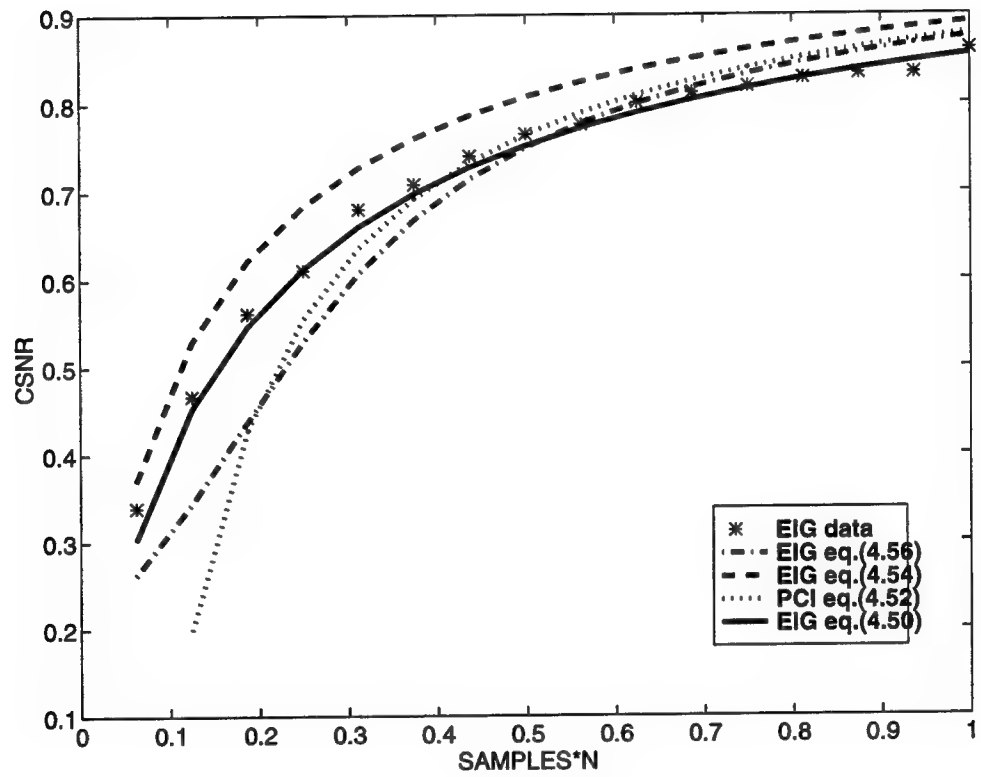


**Figure 4.6** The mean conditioned signal to noise ratio as a function of the number of snapshots for CNR = 10 dB for low number of samples.

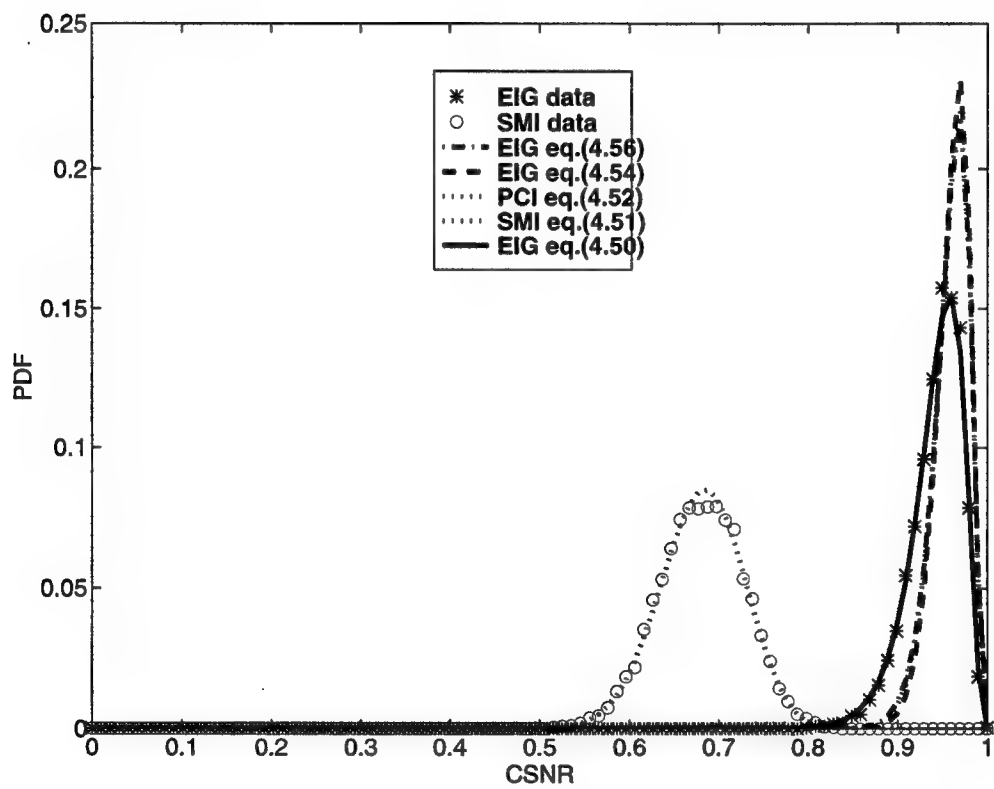


**Figure 4.7** Density functions of the CSNR for CNR = 10 dB and  $K = 4N$  snapshots.

A good match is observed between the probability density in (4.50) and the data. Likewise, the SMI density also provides an accurate representation of the data. The approximations to the eigencanceler's probability density as well as the PCI's provide a reasonable, though markedly less accurate, match to the data.

### 4.3 Discussion

A new expression has been developed for the probability density function of the CSNR of eigenanalysis-based array processing. The new expression is derived from the asymptotic theory of the principal components of the estimated covariance matrix. It is shown that, unlike the case for the SMI method, the eigencanceler's CSNR probability density is *not* independent of the covariance matrix. The new probability density provides a better fit to the data than expressions which are independent of the covariance matrix, for a wide range of interference to noise powers. Two simpler approximations are derived for the case of large INR. These approximations are shown to be independent of the covariance matrix and to provide a good fit to the data for  $\text{INR} \geq 15$  dB. The asymptotic nature of the expressions seems to have little effect for  $\text{INR} \geq 15$  dB. However, by increasing the number of samples to  $K = 4N = 128$ , the new density produces a good match to the data down to  $\text{INR} = 5$  dB.

## CHAPTER 5

### PERFORMANCE ANALYSIS

Airborne surveillance radars are faced with the difficult task of detecting weak moving targets in strong clutter and interference environments. Typically, the spatial and temporal spectra of the clutter is unknown and varying, hence adaptive techniques with fast convergence rates are important to the designers of next generation air surveillance radars. The airborne radar problem is two dimensional, with echoes of a moving target being a function of both angle and Doppler. A *space-time* receiver architecture that consists of an antenna array and provides temporal filtering of each spatial channel is capable of exploiting the information in both domains.

Previously, in chapter 1, it was mentioned that the SMI detector suggested by Brennan and Reed has a number of drawbacks like its detection performance, convergence rate for large  $N$ , sensitivity to calibration errors, and not being CFAR. Kelly's GLR [14] based detector is more complex and has convergence properties similar to the SMI detector. Calibration errors are also a problem. The SMI method was shown to be sensitive to calibration errors [15, 16]. In this chapter we advance that most of these drawbacks can be avoided in the case of STAP radar, by a linear eigenanalysis-based detector.

This chapter analyses the performance of the eigenanalysis-based detector with respect to convergence rate and sensitivity to calibration errors. Theoretical probability of detection expressions derived analytically are corroborated by simulations. Convergence rate and robustness are analyzed and compared to the SMI method. The analysis and numerical results clearly indicate the advantages of the eigenanalysis approach for space-time radar. These results are further supported by processing and analysis of Mountain-Top dataset.

#### 5.1 Performance Analysis

This section provides the performance analysis for the eigenanalysis-based method with respect to detection and robustness to calibration errors. Results are interpreted through a performance comparison with the SMI method.

##### 5.1.1 Detection

A widely accepted measure of performance for radar systems is the probability of detection curves. These curves show the probability of detection with the input SNR as an independent variable and the probability of false alarm as a parameter. In adaptive radar, detection probability is a function of the weight vectors. In turn, weight vectors are derived from estimates of the covariance matrix of the secondary data, and as such are random variables. This makes the detection probability realization-dependent. To assess the receiver operation under a wide variety of conditions, it is desired to generate average probability of detection curves. A convenient procedure consists of expressing the detection probability as a function of the CSNR defined in the previous chapter. The definition of the CSNR is repeated here

for convenience:

$$\rho = \frac{\text{SNR}_{\text{eff}}}{\text{SNR}_{\text{opt}}} = \frac{|\mathbf{w}^H \mathbf{s}|^2}{\mathbf{w}^H \mathbf{R} \mathbf{w} \mathbf{s}^H \mathbf{R}^{-1} \mathbf{s}} \quad (5.1)$$

where  $\text{SNR}_{\text{eff}}$  is the effective SNR and is defined as the ratio between the target power and the colored noise power at the array output, i.e.,

$$\text{SNR}_{\text{eff}} = \frac{|\mathbf{w}^H \mathbf{s}|^2}{\mathbf{w}^H \mathbf{R} \mathbf{w}} \quad (5.2)$$

and  $\text{SNR}_{\text{opt}} = \mathbf{s}^H \mathbf{R}^{-1} \mathbf{s}$  is the optimal SNR. The conditioned SNR is a random variable, always bounded  $0 \leq \rho \leq 1$ . The density of the conditioned SNR for the SMI method with Gaussian data has been characterized in [10]:

$$f(\rho) = \text{const} \times (1 - \rho)^{N-2} \rho^{K+1-N}, \quad 0 \leq \rho \leq 1. \quad (5.3)$$

The density of the conditioned SNR for the eigenanalysis-based detector has been derived in [1]. The development is based on the asymptotic expansion of the distribution of the principal components of the covariance matrix. Therein it is shown that the conditioned SNR can be expressed as

$$\rho = \frac{1}{1 + \frac{1}{K}\zeta} \quad (5.4)$$

where  $\zeta = \sum_{i=1}^r \nu_i$ , and  $\nu_i$  are i.i.d. random variables with exponential distribution and hence,  $\zeta$  is a Gamma random variable with  $r$  degrees of freedom and parameter 1. This characterization results in the density

$$f(\rho) = K \rho^{-2} \sum_{i=1}^r \frac{\pi_i}{\bar{\nu}_i} \exp\left(\frac{-K\left(\frac{1}{\rho} - 1\right)}{\bar{\nu}_i}\right) \quad (5.5)$$

where  $\pi_i = \prod_{j=1, j \neq i}^r \bar{\nu}_j / (\bar{\nu}_j - \bar{\nu}_i)$ . The usefulness of this expression has been demonstrated by Monte Carlo simulations presented in the reference. Also shown in the reference is that for large clutter-to-noise ratio and large  $K$  ( $K \geq 10$ ),

$$\rho \cong 1 - \frac{1}{K}\zeta. \quad (5.6)$$

From (5.6), and using the property of the gamma distribution,  $E[\zeta] = r$ , the condition  $E[\rho] = 1/2$  is met for  $K = 2r$ . This property is significant in the space-time array since  $r = \nu + \kappa - 1 \ll \nu\kappa = N$  holds even for moderate size arrays. A higher convergence rate is tantamount for achieving the same performance level using estimates based on smaller secondary datasets. Since the clutter environment can be assumed only locally homogeneous, an increased convergence rate could be essential to the proper operation of the system. The decision statistic for detection conditioned on the weight vector is given by the instantaneous output power:

$$\eta = |\mathbf{w}^H \mathbf{x}|^2 \quad (5.7)$$

When  $\mathbf{x}$  is the signal received from the cell under test and is modeled as a complex Gaussian random vector with circular symmetry under both hypothesis models, the statistic  $\eta$  has a chi-square like density:

$$f_\eta(\eta | H_i, \mathbf{w}) = \frac{1}{\bar{\eta}_i} e^{-\eta/\bar{\eta}_i} \quad (5.8)$$

where  $i = 0, 1$ , and the statistic mean values are  $\bar{\eta}_1 = E_{H_1}[\eta] = \sigma_s^2 |\mathbf{w}^H \mathbf{s}|^2 + \mathbf{w}^H \mathbf{R} \mathbf{w}$  and  $\bar{\eta}_0 = E_{H_0}[\eta] = \mathbf{w}^H \mathbf{R} \mathbf{w}$ . Scaling of the weight vector does not affect the conditioned SNR. To simplify notation, it is assumed that the gain of  $\mathbf{w}$  has been set such that  $\mathbf{w}^H \mathbf{s} = 1$ . For a given threshold  $\eta_T$ , the probability of detection is given by

$$\begin{aligned} P_d &= \int_{\eta_T}^{\infty} f_\eta(\eta | H_1, \mathbf{w}) d\eta \\ &= e^{-\eta_T/\bar{\eta}_1} \end{aligned} \quad (5.9)$$

The probability of false alarm is given by

$$\begin{aligned} P_f &= \int_{\eta_T}^{\infty} f_\eta(\eta | H_0, \mathbf{w}) d\eta \\ &= e^{-\eta_T/\bar{\eta}_0} \end{aligned} \quad (5.10)$$

The mean value of the decision statistic is equal to the average output power. An upper bound on the performance can be obtained from the case when the true noise covariance matrix is known. Then, the optimal weight vector with the unity signal gain constraint is given by  $\mathbf{w} = k \mathbf{R}^{-1} \mathbf{s}$ , with  $k = (\mathbf{s}^H \mathbf{R}^{-1} \mathbf{s})^{-1}$ . The output power under  $H_0$  is given by:

$$\bar{\eta}_0 = \frac{1}{\mathbf{s}^H \mathbf{R}^{-1} \mathbf{s}} = k \equiv \frac{1}{\alpha} \quad (5.11)$$

From which the probability of false alarm is

$$P_f = e^{-\alpha \eta_T} \quad (5.12)$$

The probability of detection can be expressed directly in terms of the probability of false alarm by noting that the output power under  $H_1$  is:

$$\bar{\eta}_1 = \sigma_s^2 + \frac{1}{\mathbf{s}^H \mathbf{R}^{-1} \mathbf{s}} = \sigma_s^2 + \frac{1}{\alpha} \quad (5.13)$$

from which it follows that the probability of detection, expressed as a function of the probability of false alarm, is

$$\begin{aligned} P_d &= e^{-\eta_T/\bar{\eta}_1} \\ &= P_f^{1/(1+\alpha\sigma_s^2)} \end{aligned} \quad (5.14)$$

To obtain expressions for the detection probability of the SMI and the eigenanalysis methods, we observe that, under either hypothesis, the output power can be expressed in terms of the

conditioned SNR  $\rho$  and the parameter  $\alpha$ . From (5.1) and (5.7) the conditional output power under  $\mathbf{H}_0$  is:

$$\bar{\eta}_0 = \frac{1}{\rho\alpha} \quad (5.15)$$

It follows that the conditioned probability of false alarm is given by:

$$P_{f|\rho} = e^{-\rho\alpha\eta_T} \quad (5.16)$$

The average probability of false alarm is then computed from

$$P_f = \int_0^1 P_{f|\rho} f_\rho(\rho) d\rho \quad (5.17)$$

where  $f_\rho(\rho)$  is given by (5.3) for the SMI method, and by (5.5) for the eigenanalysis method. The conditioned output power under  $\mathbf{H}_1$  is given by,

$$\bar{\eta}_1 = \sigma_s^2 + \frac{1}{\rho\alpha} \quad (5.18)$$

and the conditional probability of detection is

$$P_{d|\rho} = \exp\left(\frac{\eta_T}{\sigma_s^2 + 1/\rho\alpha}\right) \quad (5.19)$$

The average probability of detection is then expressed:

$$P_d = \int_0^1 P_{d|\rho} f_\rho(\rho) d\rho \quad (5.20)$$

These expressions are used later to generate the theoretical probability of detection curves for each of the methods.

### 5.1.2 Robustness

It is well known that the performance of adaptive arrays is affected by calibration errors. Analysis of the Mountaintop data reported in chapter 6 reveals target cancelation due to the mismatch between the true received signal vector and the steering vector used in calculating the weights. Also noted in chapter 6 is the fact that the target cancelation is more pronounced for the SMI than for the eigenanalysis method. This observation motivates the analysis in this section.

Target cancelation occurs when there are calibration errors and the target signal is present during training (estimation of the noise covariance matrix). Since the steering vector is mismatched to the signal vector, the target is interpreted as an interference and the array proceeds to cancel it. To isolate signal cancelation from noise covariance matrix estimation effects, we assume that the true covariance matrix is known. In fact, this assumption accurately represents the case when the weight vector is applied to the data it was derived from. Additionally, we make the following simplifying assumptions for analytical tractability:

1. Processing is carried out only in the spatial domain.

2. Calibration errors are limited to the angle of the steering vector. Thus, the target and the presumed steering vector are represented by vectors of the type

$$\mathbf{s}(\theta) = \frac{1}{\sqrt{N}} [1, e^{j\theta}, \dots, e^{j(N-1)\theta}]^T.$$

3. There is a single interference represented by the vector  $\mathbf{s}_i$ .

4. The interference vector is orthogonal to the true target vector,  $\mathbf{s}_i^H \mathbf{s} = 0$ .

The perturbation model presented above represents the case when the steering vector sweeping an angular sector searching for targets is pointing off-target. A method sensitive to such errors would require a dense search pattern. However, it should be noted that this model is a simplification which does not cover angle errors randomly distributed over the array. These errors lead to waveform distortions rather than an angle error. Thus the simple model used here provides some, if limited, indication of the robustness of the eigencanceler. The Mountain-Top data analysis presented in the next section lends further support to the robustness claims.

The analysis will be shown to be invariant to a scaling constant, hence we define the normalized covariance matrix,

$$\mathbf{R} = \mathbf{I} + \bar{\sigma}_s^2 \mathbf{s} \mathbf{s}^H + \bar{\sigma}_i^2 \mathbf{s}_i \mathbf{s}_i^H \quad (5.21)$$

where  $\bar{\sigma}_s^2 = \text{SNR}$  and  $\bar{\sigma}_i^2 = \text{INR}$  (interference-to-noise ratio). Performance is investigated through the gain term

$$G = \frac{|\mathbf{w}^H \mathbf{s}|^2}{\mathbf{w}^H \mathbf{R}_i \mathbf{w}} \quad (5.22)$$

where  $\mathbf{R}_i$  is the noise-plus-interference covariance matrix,  $\mathbf{R}_i = \mathbf{I} + \bar{\sigma}_i^2 \mathbf{s}_i \mathbf{s}_i^H$ . This gain is the ratio of the array output SNIR to the input SNR. In the ideal case, when there are no calibration errors, and due to the orthogonality assumed between the interference and the target, it is readily shown that  $G = 1$ . Consequently, in the presence of calibration errors  $0 \leq G \leq 1$ . The goal is to characterize  $G$  for the SMI and eigenanalysis methods. The SMI weight vector is given by

$$\mathbf{w} = \mathbf{R}^{-1} \tilde{\mathbf{s}} \quad (5.23)$$

where  $\tilde{\mathbf{s}}$  is the presumed steering vector. The eigenccanceler weight vector is given by:

$$\mathbf{w} = (\mathbf{I} - \mathbf{s}_i \mathbf{s}_i^H) \tilde{\mathbf{s}} \quad (5.24)$$

The gain  $G$  for each of the methods is computed in the appendix. For the SMI it is found:

$$G_o = \frac{|\rho_1|^2 (1 - \gamma_s)^2}{1 - \gamma_s (2 - \gamma_s) |\rho_1|^2 - \gamma_i (2 - \gamma_i) |\rho_2|^2} \quad (5.25)$$

where  $\rho_1 = \tilde{\mathbf{s}}^H \mathbf{s}$ ,  $\rho_2 = \tilde{\mathbf{s}}^H \mathbf{s}_i$ ,  $\gamma_s = \text{SNR}/(1 + \text{SNR})$ , and  $\gamma_i = \text{INR}/(1 + \text{INR})$ . Note that  $0 \leq \gamma_s, \gamma_i \leq 1$ . As observed by other authors through similar analysis,  $G_o$  degrades as SNR increases. In the extreme case,  $\text{SNR} = \infty$  ( $\gamma_s = 1$ ), and  $G_o = 0$ . The other extreme is

$G_o = |\rho_1|^2 / (1 - |\rho_2|^2)$ , obtained for  $\gamma_s = 0$  and  $\gamma_i = 1$ . The eigencanceler's gain term is computed in the appendix and is given by:

$$G_e = \frac{|\rho_1|^2}{1 - |\rho_2|^2} \quad (5.26)$$

From (5.25) and (5.26) it is observed that  $G_o \leq G_e$ , with the equality for  $\gamma_s = 0$  and  $\gamma_i = 1$ . Consequently, the eigenanalysis method is less affected by angle calibration errors than the SMI method. This is illustrated in Figure 5.1, where  $G_e$  and  $G_o$  are plotted for a 14-element array, several values of the SNR factor  $\gamma_s$ , an error angle of  $\pi/10$  radians, and an angle of  $4\pi/10$  between the presumed steering vector and the interference.

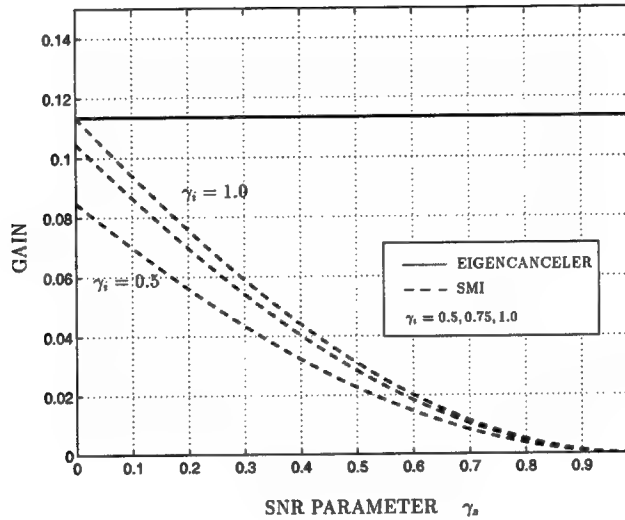


Figure 5.1 Signal cancelation effects:  $G_e$ ,  $G_o$  vs.  $\gamma_s$  with  $\gamma_i$  as parameter.

### 5.1.3 Numerical Results

In this subsection, theoretical probability of detection curves are generated for each of the methods, and are compared to simulation. The array has eight elements and four tap delays at each channel. The signal environment consists of clutter distributed in an angular sector. The clutter is distributed between 20 degrees and 40 degrees. The total input CNR of the distributed clutter equals 15 dB. The look direction steering vector points to 50 degrees and 0.5 normalized Doppler frequency. Eq. (5.20), together with (5.5) and (5.3), provides the means to analyze the detection performance numerically. Theory and simulations are compared in Figures 5.2 and 5.3. The densities of the conditioned SNR for the eigenanalysis and SMI methods, for  $K = 2N$  samples, and as given in (5.5) and (5.3), are shown in the lower part of Figure 5.2. The eigencanceler was computed using  $r = 6$  principal eigenvalues. The upper part of Figure 5.2 consists of histograms developed from 10,000 simulation runs.

A good fit is observed between the theoretical and the simulation curves. Figure 5.3 plots the probability of detection for the various methods, i.e., the average probability of detection versus the input SNR.

The detection threshold  $\eta_T$  is found from the solution to (5.17) when the average probability of false alarm is set to  $10^{-5}$ . The probability of detection is computed using (5.20). The curve labeled “opt” is the optimal case obtained from (5.14). The probability of detection curves also show a good fit between theory and simulations.

## 5.2 Discussion

In this chapter we studied eigenanalysis-based detection for airborne surveillance radars and compared the performance to that of the SMI method. Analytical expressions for the receiver operating characteristics were obtained based on the asymptotic expansion of the distribution of the principal components of the covariance matrix and were corroborated by simulations. The results clearly indicate the higher convergence rate of the eigenanalysis method. Expressions were developed to characterize the robustness with respect to the pointing error. This model is a simplification of the more general case of random angle errors.

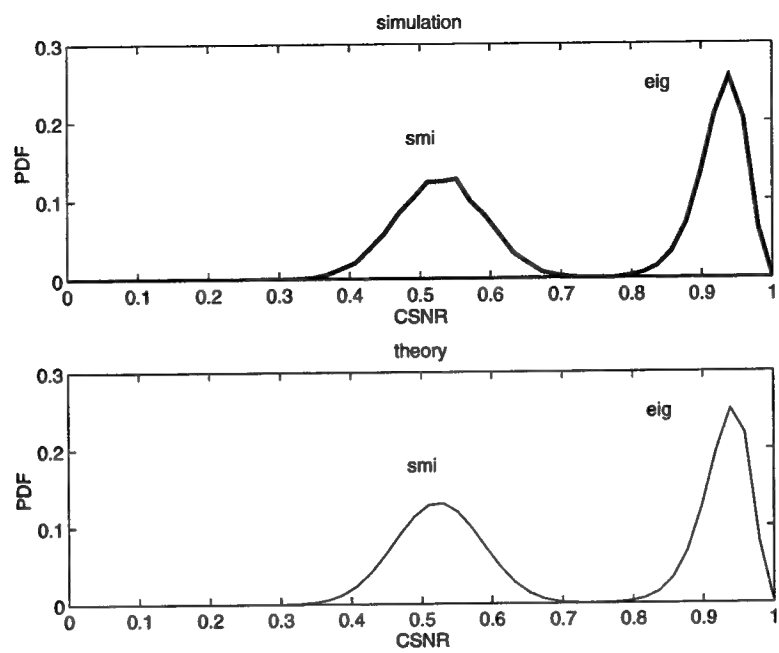


**Figure 5.2** Probability density of the CSNR. Top: simulations. Bottom: theoretical.

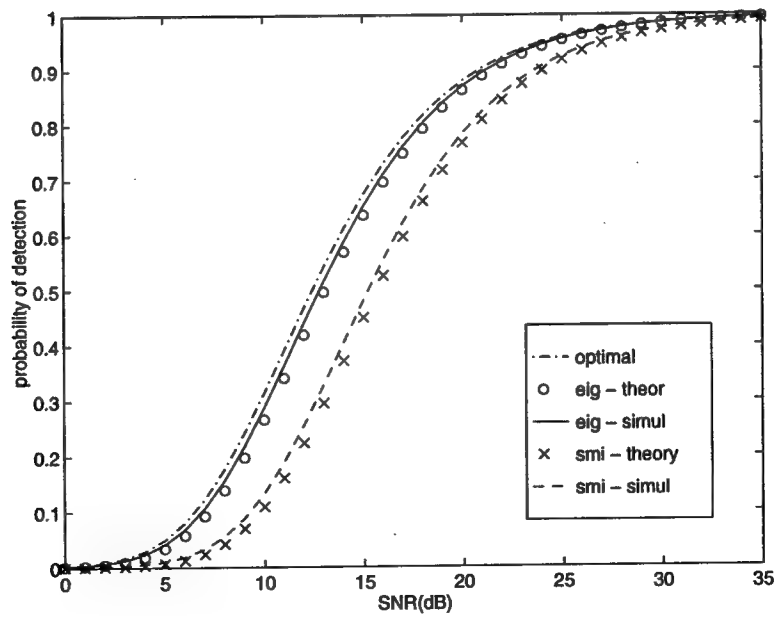


**Figure 5.3** Probability of detection from theory and simulations.

## CHAPTER 6

### PERFORMANCE ANALYSIS USING EXPERIMENTAL DATA

Conventional beamformers cancel the interference without considering a desired signal. A linearly constrained adaptive array, however, tries to preserve signals at a given angle and/or Doppler frequency. To preserve a presumed desired signal, a steering vector is formed using theoretical output of the antenna array under ideal conditions. This steering vector is used to calculate the weights for a given adaptive criteria, such that there is some gain in the *direction* of the desired signal. However, due to practical limitations the presumed steering vector and the true desired signal do not necessarily match. This mismatch, also known as the perturbation problem, causes signal cancellation when the optimum array processor is used.

The perturbation problem, which has many sources, has been an active research topic. The perturbation due to pointing errors, mismatch between the presumed and true angle of arrival, was studied by Er [17]. Hybrid techniques were suggested by Habu [51] to overcome pointing errors. Another source of mismatch is the calibration errors that results in random gain and phase errors at every element. The gain and phase mismatches are caused by unmatched antennas and receiver electronics, producing a different response at every channel. Previous work on calibration effects includes the problem of small phase errors at each element [52], and the more general case of amplitude and phase errors [53, 54, 55]. Certain array processing criteria also requires a prior knowledge of the interference correlation matrix, i.e. the Weiner solution. In general, the true correlation matrix of the interference and noise is not available and it needs to be estimated from a finite record of the data. The estimation error, due to training set size limitation, affects the performance of the array. Using a larger training set for a better estimate, may also result in problems if the data is not completely stationary. If the training data set includes the desired signal, the estimated correlation matrix has a desired signal component. If the desired signal component is large, the processor interprets the desired signal portion mismatched to the steering vector as interference, and signal suppression is observed even with a small steering vector perturbation [15, 56].

#### **6.1 The Mountaintop Data Package**

The Mountaintop Program was initiated to study advanced processing techniques and technologies required to support the mission requirements of the next generation airborne early warning platform. In this chapter, the radar and the data processing aspects such as calibration and pulse compression are discussed.

##### **6.1.1 Description of the Assets**

Two major assets of the Mountaintop Program are Radar Surveillance Technology Experimental Radar (RSTER) and Inverse Display Phase Central Array (IDPCA). RSTER is a 5 meter by 10 meter vertically polarized array made up of 14 row elements with an independent

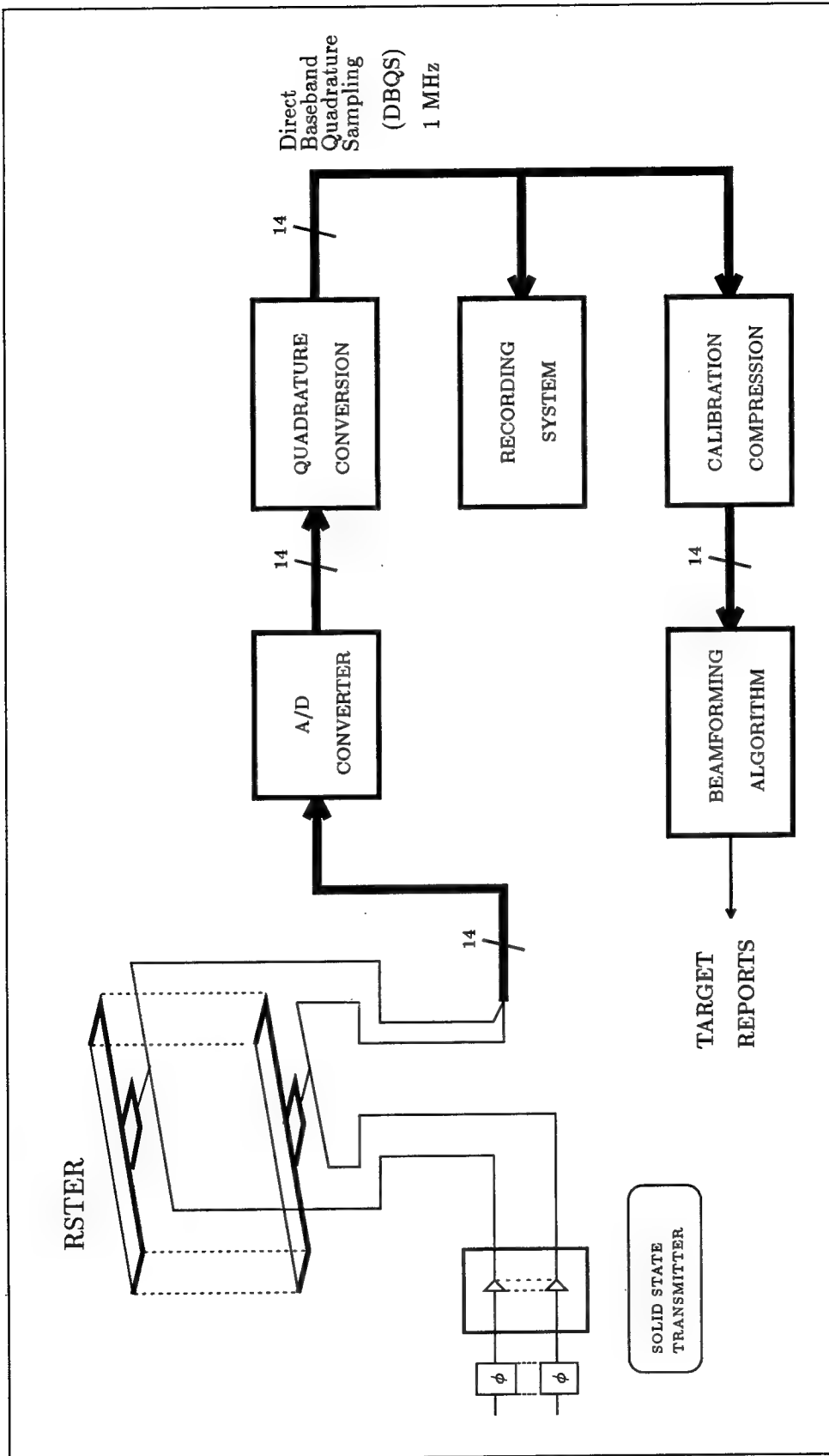


Figure 6.1 The Radar Surveillance Technology Experimental Radar (RSTER)

phase shifter, transmitter and receiver. This original configuration, with adaptivity in elevation, is referred to as the RSTER configuration. The antenna was designed to be mounted vertically to achieve azimuth adaptivity. This configuration is referred to as RSTER-90. The basic set up of the data collection is given in Figure 6.1. IDPCA was developed to overcome the challenge of providing a meaningful emulation of the airborne surveillance environment. For a fixed radar, IDPCA produces clutter returns with the same spatial and temporal characteristics as observed from an airborne surveillance platform. Since clutter profile in azimuth-Doppler space is due to the motion of the aperture's phase center, to effect the emulation one can move an antenna or deploy several antennas and move between them. Apparent motion occurs along the length of the array. The IDPCA is a transmit-only device and the clutter returns are received through the larger RSTER-90 antenna. The effectiveness of the IDPCA's motion was demonstrated by comparing the clutters returns of IDPCA to clutter returns using a Lear jet [57].

### 6.1.2 Calibration

Theory of array processing is developed assuming ideal elements (channels) with omnidirectional, identical and equally spaced antennas and perfectly matched channel receiver electronics. However, to satisfy these ideal conditions is an impossible challenge. The hardware calibration is limited by the current available technology, but the calibration can be enhanced by using digital filters to compensate for the differences in the receiver electronics, and the antenna mismatches. In this section, the design of the digital calibration filters are discussed.

Calibration is done in two stages: Receiver Calibration (RCAL) and Antenna Calibration (ACAL). RCAL covers differences in amplitude and phase ripple between channels at intermediate frequency (IF). ACAL compensates for amplitude and phase match differences between channels at radio frequency (RF). RCAL and ACAL files are recorded while two different, known test signals are injected into antenna/receiver hardware. For RCAL, a 1 MHz LFM is injected into all channels of RSTER in the IF portion of the receiver, after the RF channel equalizer filters. During the injection of this test signal, data is recorded after A/D conversion and direct baseband quadrature sampling (DBQS) at a 1 MHz rate. For ACAL a 500 KHz LFM signal is injected at the antenna immediately after the duplexer assembly. Data is recorded after the A/D, using DBQS at 1 MHz sampling. Complex weights are determined from this data set in order to equalize the channels.

#### 6.1.2.1 Design of Receiver Calibration Filters

The band limited receiver is modeled with a transfer function. RCAL files are used to design a transversal filter, which estimates the receiver transfer functions and equalizes to match each channel to the reference channel. The output of a transversal filter, as shown in Figure 6.2 is given by the finite convolution sum

$$y_i(n) = \sum_{k=0}^{N_t-1} w_k^* u_i(n - k), \quad (6.1)$$

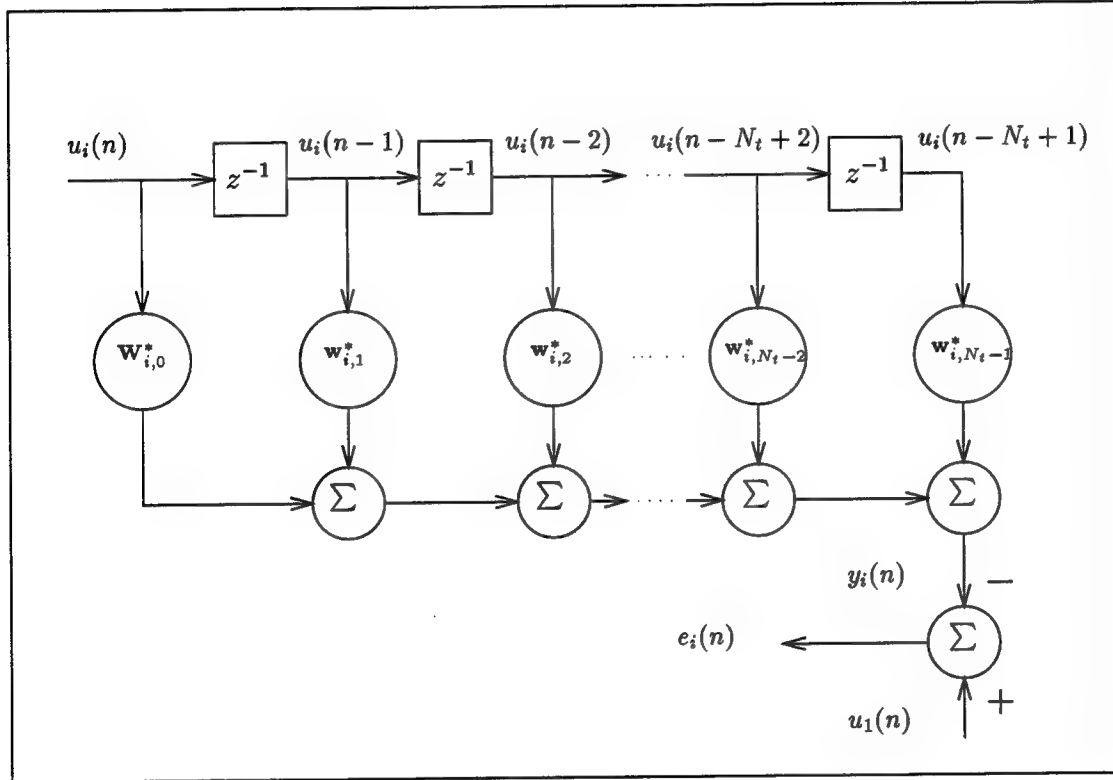


**Figure 6.2** Transversal Linear Prediction Filter

where  $N_t$  denotes the number of tabs,  $u(n)$  is the input to the filter and  $w_k$  are the weights calculated using the least squares (LS) algorithm. The output of the first antenna,  $u_1(n)$ , is used as the reference signal. To calculate the weights for the  $i^{th}$  element, the LS algorithm minimizes the power of the error function given by

$$e_i(n) = u_1(n) - \sum_{k=0}^{N_t-1} w_{i,k}^* u_i(n-k). \quad (6.2)$$

Assuming  $N$  samples of data are recorded, it can be easily shown [58][59] that the error function,  $e_i(n)$ , is minimized when

$$\mathbf{w}_i = A^+ \mathbf{u}_1, \quad (6.3)$$

where

$$\mathbf{w}_i = \begin{bmatrix} w_{i,0} \\ w_{i,1} \\ \vdots \\ w_{i,N_t-1} \end{bmatrix}, \quad \mathbf{u}_1 = \begin{bmatrix} u_1^*(N_t-1) \\ u_1^*(N_t) \\ \vdots \\ u_1^*(N-1) \end{bmatrix}, \quad (6.4)$$

$$\mathbf{A}^H = \begin{bmatrix} u_i(N_t-1) & u_i(N_t) & \cdots & u_i(N-1) \\ u_i(N_t-2) & u_i(N_t-1) & \cdots & u_i(N-2) \\ \vdots & \vdots & \ddots & \vdots \\ u_i(0) & u_i(1) & \cdots & u_i(N-N_t) \end{bmatrix}, \quad (6.5)$$

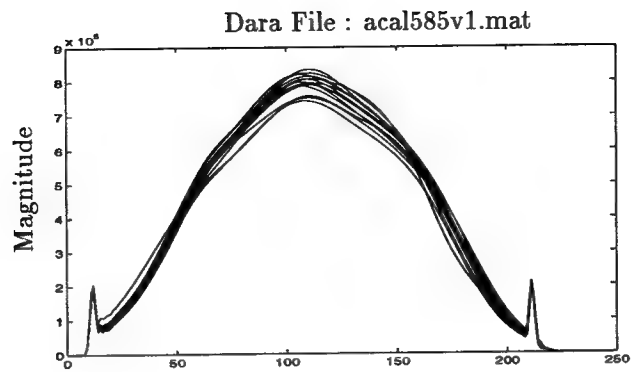
and (+) denotes pseudo-inverse for an over determined system given by

$$\mathbf{A}^+ = (\mathbf{A}^H \mathbf{A})^{-1} \mathbf{A}^H. \quad (6.6)$$

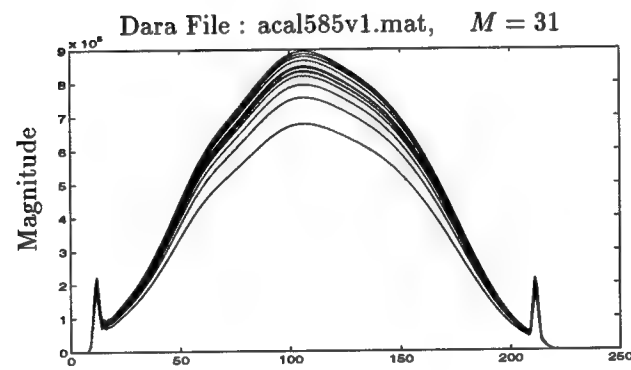
### 6.1.2.2 Design of Antenna Calibration Filters

The antenna calibration is the second stage of the calibration. Amplitude and phase correction is utilized to overcome mismatches between signals at the receiver inputs. The antenna mismatch is modeled as a single complex weight, since the antenna has a large bandwidth. A known test signal is injected immediately after the duplexer assembly, and the output is recorded at the output of A/D into ACAL files. Since the ACAL signal travels through both the channel front end and the receiver portion, prior to determining the antenna calibration weights, the data is equalized using RCAL weights. This equalization step is only needed if the injected test signal is LFM, and not needed if it is a single frequency. To calculate the single weight needed for the  $i^{th}$  element of the array, (6.3) is used with  $N_t = 1$ . Again, the output of the first antenna,  $u_1(n)$ , is used as the reference signal.

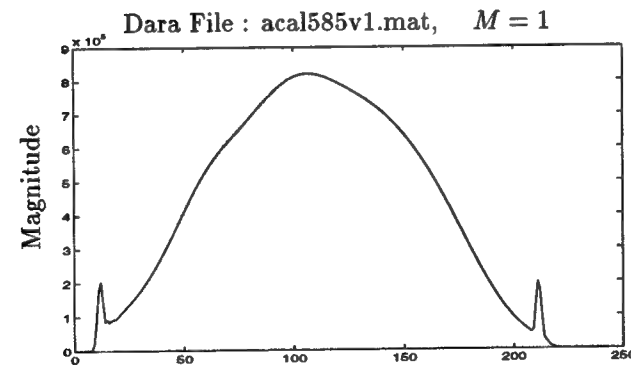
Figure 6.3 illustrates the effects of the calibration process. Shown is CPI 1 of ACAL file acal585v1.mat before and after calibration. In Figure 6.3(a), the magnitude of channel outputs are plotted on top of each other. Every channel's output has a different shape and amplitude for the same injected test signal. In Figure 6.3(b), the same data is plotted after receiver equalization using RCAL weights designed with the RCAL file rcal585v1.mat and  $N_t = 31$ . Compared with Figure 6.3(a) the equalized channel outputs have the same shape but different amplitude. The amplitude differences are calibrated using ACAL weights,



(a) Uncalibrated PRI1 of CPI1



(b) After Receiver Calibration



(c) After Antenna Calibration

**Figure 6.3** Results of Receiver and Antenna Calibration

which are designed using the ACAL file after receiver calibration. In Figure 6.3(c) the output of the channels are plotted after the antenna calibration, where all the outputs have the same shape and amplitude.

### 6.1.3 Pulse Compression

In order to receive measurable target returns, the transmitted pulse must have enough energy. A signal with a larger amplitude may be transmitted to increase the energy of the signal but the amplitude of the signal is limited by the transmitter power. An other approach is to use a longer pulse, but this causes problems with the resolution of the radar. For example, if a  $100 \mu s$  pulse is transmitted, a 15 km resolution would result which is not practical. The Mountaintop radar uses pulse compression to achieve high range resolution. The radar transmits a wideband Chirp pulse. The chirp radar concept is described in detail by Klauder [60] and Wehner [56]. Samples of the complex envelope of a chirp signal is given by the relation

$$s(n) = e^{j2\pi(wn^2/2-n/2)} \quad n = 0, 1, \dots, N-1, \quad (6.7)$$

where  $N$  is the number of samples taken during the pulse and assuming Nyquist sampling rate,  $w = 1/(N-1)$ . A plot of the transmitted pulse envelope, pulse frequency, and RF wave form as a function of time, is given in Figure 6.4 (a), (b), and (c), respectively. The matched filter to this pulse is given by

$$s(n) = e^{j2\pi(wn^2/2+n/2)} \quad n = -N+1, -N+2, \dots, 0. \quad (6.8)$$

The output of the matched filter is plotted in Figure 6.5. To generate these plots, a  $100 \mu s$  pulse is used with a  $1 \mu s$  sampling period which results in 100 samples,  $N = 100$ . Using this method the  $100 \mu s$  pulse is compressed to give a resolution of  $1 \mu s$  which corresponds to 150 m. The largest sidelobe is 13 dB below the main lobe. Windowing can be used to get lower sidelobes, but this will cause a wider mainlobe. In this chapter, none of the plots generated using the experimental data used windowing on pulse compression.

## 6.2 Joint Domain and Cascade Processors

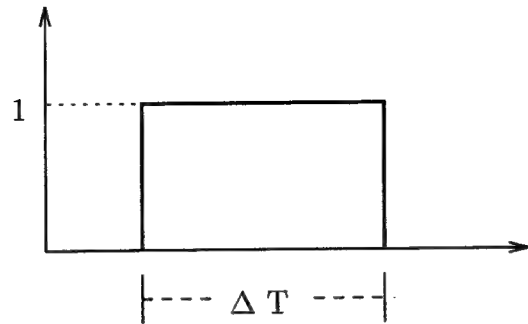
This section gives some background into joint domain and cascade processing. Also we shall introduce and define some parameters that will be used through out this chapter.

Define the data matrix  $\mathbf{X}$  which is made up of  $N_t \times N_s$  samples of returned data and is given by

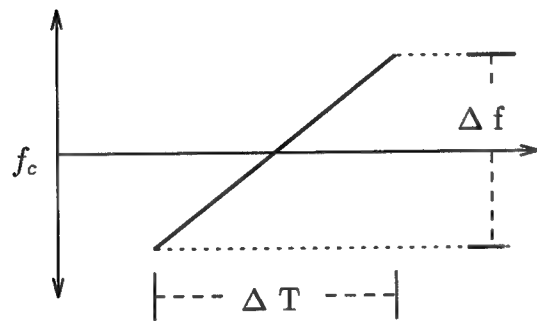
$$\mathbf{X} = \begin{bmatrix} x_{1,1} & x_{1,2} & \cdots & x_{1,N_s} \\ x_{2,1} & x_{2,2} & \cdots & x_{2,N_s} \\ \vdots & \vdots & \ddots & \vdots \\ x_{N_t,1} & x_{N_t,2} & \cdots & x_{N_t,N_s} \end{bmatrix}. \quad (6.9)$$

If a target is present at a given range cell,  $\mathbf{X}$  has the form

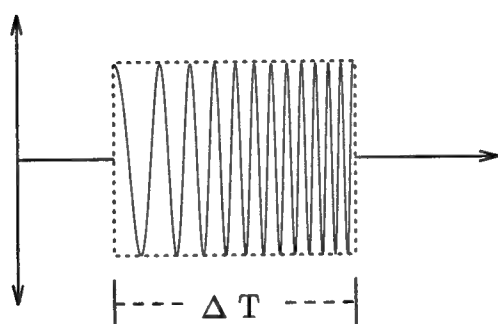
$$\mathbf{X} = \mathbf{X}_d + \mathbf{X}_i + \mathbf{X}_n, \quad (6.10)$$



(a) Transmitted Pulse Envelope

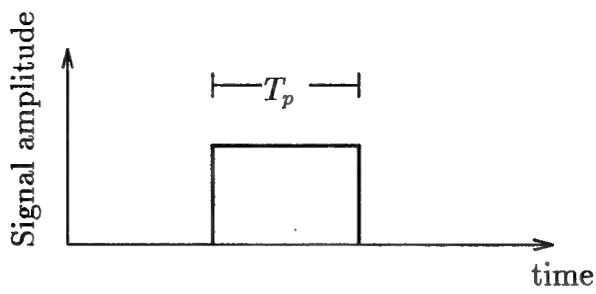


(b) Transmitted Pulse Frequency

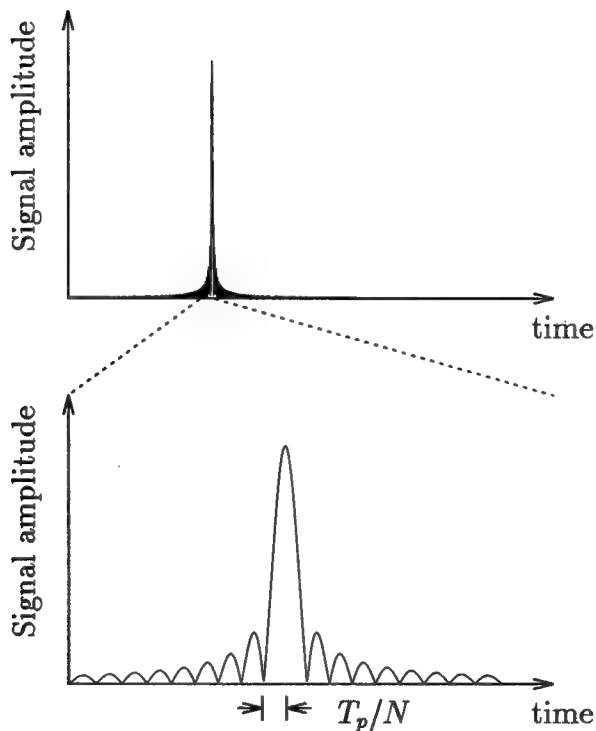


(c) Transmitted Pulse RF Waveform

**Figure 6.4 Chirp Signal**



(a) Received Pulse Envelope



(b) Output of the Matched Filter

**Figure 6.5 Chirp Signal Matched Filter Output**

where  $\mathbf{X}_d$  is the target signal (desired signal),  $\mathbf{X}_i$  is the interference, and  $\mathbf{X}_n$  is the noise matrix. If a target is not present in a given range cell then

$$\mathbf{X} = \mathbf{X}_i + \mathbf{X}_n. \quad (6.11)$$

The columns of  $\mathbf{X}_d$  are samples in time that give information about the velocity of the target. The rows of this matrix are samples in space that give information about the angle of the received signal. In the ideal case, when the spatial channels are co-linear, identical, omni-directional and equally spaced with spacing  $d$ , the entries of matrix  $\mathbf{X}_d$  are given by

$$x_d(k, n) = \frac{\sigma_d}{\sqrt{N_s N_t}} e^{j2\pi((k-1)\psi_t + (n-1)\psi_s)}, \quad (6.12)$$

where  $\sigma_d^2$  is the desired signal power,  $\psi_s$  is the normalized spatial frequency and  $\psi_t$  is the normalized Doppler frequency. The normalized spatial frequency is given by

$$\psi_s = \frac{2\pi d \sin \theta_d}{\lambda}, \quad (6.13)$$

where  $\lambda$  is the wavelength of the transmitted signal and  $\theta_d$  is angle of the target. The normalized Doppler frequency is given by

$$\psi_t = \frac{2vPRI}{\lambda}, \quad (6.14)$$

where  $v$  is the radial velocity of the target. The desired signal component of the matrix  $\mathbf{X}$ , under ideal conditions, can also be written as

$$\mathbf{X}_d = \sigma_d \mathbf{s}_t \mathbf{s}_s^T, \quad (6.15)$$

where  $\mathbf{s}_t$ , the  $N_t \times 1$  normalized temporal steering vector, and  $\mathbf{s}_s$ , the  $N_s \times 1$  normalized spatial steering vector, are given by

$$\mathbf{s}_t = \frac{1}{\sqrt{N_t}} \begin{bmatrix} 1 \\ e^{j2\pi\psi_t} \\ \vdots \\ e^{j2\pi(K-1)\psi_t} \end{bmatrix} \quad \text{and} \quad \mathbf{s}_s = \frac{1}{\sqrt{N_s}} \begin{bmatrix} 1 \\ e^{j2\pi\psi_s} \\ \vdots \\ e^{j2\pi(N-1)\psi_s} \end{bmatrix}. \quad (6.16)$$

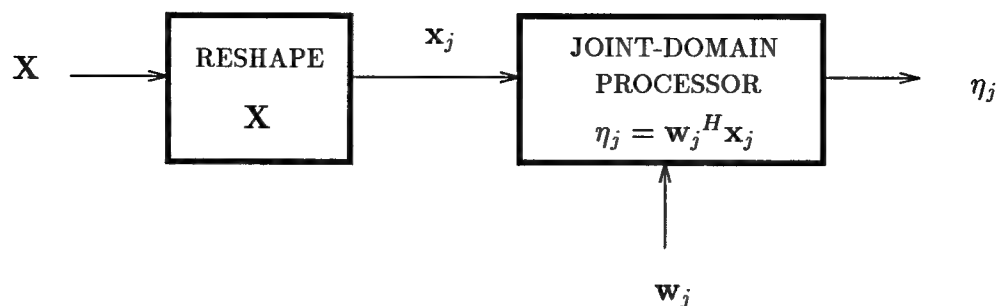
The  $N_s N_t \times 1$  normalized joint-domain steering vector is formed by stacking the transpose of the rows of  $\mathbf{X}_d$  and it is given by

$$\mathbf{s}_j = \mathbf{s}_t \otimes \mathbf{s}_s, \quad (6.17)$$

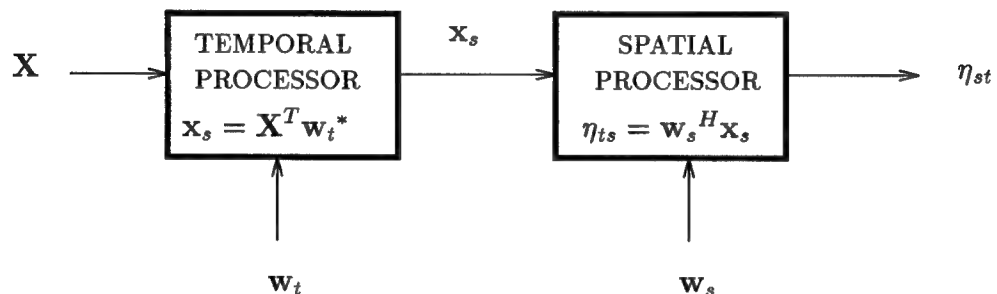
where  $\otimes$  is the Kronecker product. Assuming  $PRI$ ,  $d$ , and  $\lambda$  have been properly chosen to meet the Nyquist sampling criterion,  $\psi_s$  and  $\psi_t$  are confined within  $[-0.5, 0.5]$ .

For space-time radar, joint-domain and cascade processing are two possible configurations. With the joint-domain linear processor (see Figure 6.2(a)), the data is processed as follows,

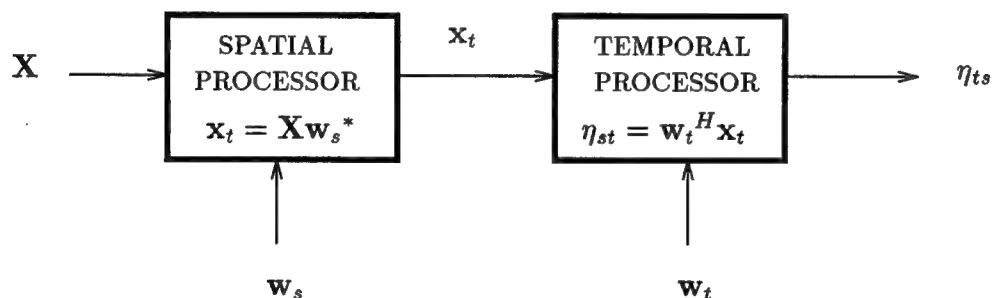
$$\eta_j = \mathbf{w}_j^H \mathbf{x}_j, \quad (6.18)$$



(a) Joint-Domain Configuration



(b) Time-Space Configuration



(c) Space-Time Configuration

**Figure 6.6** Block Diagram of Joint-Domain and Cascade Processors

where  $\mathbf{w}_j$  is the  $N_s N_t \times 1$  joint domain weight vector and  $\mathbf{x}_j$  is the  $N_s N_t \times 1$  joint-domain data vector formed by stacking the transpose of the rows of the data matrix  $\mathbf{X}$ . There are two cascade configurations: time-space (T-S) and space-time (S-T). The T-S configuration consists of  $K$ -dimensional temporal processing followed by  $N_s$ -dimensional spatial processing. S-T configuration processes the data in the opposite order. Block diagrams of cascade configurations are shown in Figure 6.2 (b) and (c). In the T-S configuration the input to the temporal processing stage is data matrix  $\mathbf{X}$ . The output of this stage is the  $N_s \times 1$  spatial data vector:

$$\mathbf{x}_s = \mathbf{X}^T \mathbf{w}_t^*, \quad (6.19)$$

where  $\mathbf{w}_t$  is the  $N_t \times 1$  temporal weight vector and  $(*)$  means complex conjugate. The output of the temporal processor is used by the spatial processor, which produces

$$\eta_{ts} = \mathbf{w}_s^H \mathbf{x}_s, \quad (6.20)$$

where  $\mathbf{w}_s$  is an  $N_s \times 1$  spatial weight vector. Similarly, for the S-T configuration the output of the spatial beamformer is

$$\mathbf{x}_t = \mathbf{X} \mathbf{w}_s^*, \quad (6.21)$$

where  $\mathbf{x}_t$  is the  $N_t \times 1$  temporal data vector and the output of the temporal beamformer is

$$\eta_{st} = \mathbf{w}_t^H \mathbf{x}_t. \quad (6.22)$$

Both of these cascade configurations may use different adaptive criteria for processing in both domains. The performance of the cascade should approach that of the optimum processor with the same configuration. Cascade processing, especially the S-T configuration, has been very popular in recent years, but it has been shown that joint-domain processing performs better than both cascade configurations [61].

Later in this chapter, the joint-domain and the post-Doppler processors are applied to the Mountaintop data. The post-Doppler processor has a cascade configuration with a non-adaptive temporal processor followed by an adaptive spatial processor.

### 6.3 Array Improvement Factor

Under the assumption of uncorrelated signal, interference and noise, the correlation matrix of the data vector  $\mathbf{x}$ , which may have the form of  $\mathbf{x}_j$ ,  $\mathbf{x}_t$  or  $\mathbf{x}_s$ , is given by

$$\mathbf{R} = E [\mathbf{x} \mathbf{x}^H] = \sigma_d^2 \mathbf{R}_d + \sigma_i^2 \mathbf{R}_i + (\sigma_n^2 / N) \mathbf{I}, \quad (6.23)$$

where  $N$  is the length of the data vector  $\mathbf{x}$ ,  $\sigma_d^2$  is the desired signal power and  $\mathbf{R}_d$  is the autocorrelation of the desired signal given by

$$\mathbf{R}_d = \mathbf{x}_d \mathbf{x}_d^H. \quad (6.24)$$

$\mathbf{R}_i$  is the autocorrelation of the interference,  $\sigma_i^2$  is the interference power, and  $\sigma_n^2$  is the power of the white Gaussian noise.  $\mathbf{R}_d$  and  $\mathbf{R}_i$  are normalized to have a trace of one.

The output power of the beamformer as a function of  $\mathbf{w}$  is given by

$$\begin{aligned} P_{BF}(\mathbf{w}) &= E \left[ |\mathbf{w}^H \mathbf{x}_d|^2 \right] = E \left[ \mathbf{w}^H \mathbf{x} \mathbf{x}^H \mathbf{w} \right] \\ &= \mathbf{w}^H \mathbf{R}_d \mathbf{w} \\ &= \sigma_d^2 \mathbf{w}^H \mathbf{R}_d \mathbf{w} + \sigma_i^2 \mathbf{w}^H \mathbf{R}_i \mathbf{w} + (\sigma_n^2/N) \mathbf{w}^H \mathbf{w}. \end{aligned} \quad (6.25)$$

The first term of  $P_{BF}$  is the signal power and the remaining is the interference-plus-noise power. Signal-to-interference-plus-noise ratio at the output of the beamformer is given by

$$\text{SNIR}_{BF} = \frac{\sigma_d^2 |\mathbf{w}^H \mathbf{x}_d|^2}{\sigma_i^2 \mathbf{w}^H \mathbf{R}_i \mathbf{w} + (\sigma_n^2/N) \mathbf{w}^H \mathbf{w}} = \frac{\text{SNR} |\mathbf{w}^H \mathbf{x}_d|^2}{\text{INR} \mathbf{w}^H \mathbf{R}_i \mathbf{w} + (1/N) \mathbf{w}^H \mathbf{w}}, \quad (6.26)$$

where  $\text{SNR} = \sigma_d^2/\sigma_n^2$  and  $\text{INR} = \sigma_i^2/\sigma_n^2$ .

The array improvement factor (AIF) is defined as the ratio of  $\text{SNIR}_{BF}$  to SNR at the input of the beamformer as a function of the weight vector:

$$G(\mathbf{w}) = \frac{|\mathbf{w}^H \mathbf{x}_d|^2}{\mathbf{w}^H \mathbf{R}_{i+n} \mathbf{w}}, \quad (6.27)$$

where  $\mathbf{R}_{i+n}$  is the interference-plus-noise correlation matrix defined as

$$\mathbf{R}_{i+n} = \text{INR} \mathbf{R}_i + (1/N) \mathbf{I}. \quad (6.28)$$

Assuming  $\mathbf{x}_d$  and  $\mathbf{R}_{i+n}$  are known,  $\text{SNIR}_{BF}$  is maximized by the Weiner solution given by

$$\mathbf{w}_o = k \mathbf{R}_{i+n}^{-1} \mathbf{x}_d \quad \text{and} \quad G(\mathbf{w}_o) = \mathbf{x}_d^H \mathbf{R}_{i+n}^{-1} \mathbf{x}_d, \quad (6.29)$$

where  $k$  is a gain constant and does not have an effect on the AIF. To study the behavior of the AIF, first consider a noise only correlation matrix ( $\sigma_i^2 = 0$ ). For this case the weight vector and the AIF are given by

$$\mathbf{w}_o = k \mathbf{x}_d \quad \text{and} \quad G_n(\mathbf{w}_o) = N. \quad (6.30)$$

With a single interferer ( $\mathbf{R}_i = \mathbf{x}_i \mathbf{x}_i^H$ ), inverse of the correlation matrix is given by

$$\mathbf{R}_{i+n}^{-1} = (\text{INR} \mathbf{x}_i \mathbf{x}_i^H + (1/N) \mathbf{I})^{-1} = N \mathbf{I} - \frac{\text{INR} \cdot L}{1 + \text{INR} \cdot L} \mathbf{x}_i \mathbf{x}_i^H, \quad (6.31)$$

and the AIF is given by

$$G_{i+n}(\mathbf{w}_o) = N - \frac{\text{INR} \cdot L}{1 + \text{INR} \cdot L} |\mathbf{x}_d^H \mathbf{x}_i|^2. \quad (6.32)$$

$G_{i+n}$  is confined within  $[(N-1), N]$ ; the maximum value is achieved when the  $\text{INR} = 0$  or  $\mathbf{x}_d^H \mathbf{x}_i = 0$  and the lower limit is obtained when the  $\text{INR} = \infty$  and  $\mathbf{x}_d^H \mathbf{x}_i = 1$ .

However, in many cases of practical importance the available information about the desired signal vector is imprecise. Also, the correlation matrix of interference-plus-noise is estimated using a finite set of data. These two practical problems cause a decrease in performance of the Weiner solution. Later, the AIF will be used as the figure of merit to compare the performance of the SMI and the eigencanceler methods under these conditions.

## 6.4 Array Improvement Factor Calculations

In this section the effects of calibration errors in terms of the AIF dependency on the desired signal component of the correlation matrix are studied. For analytical tractability, the special case of a single interference and the spatial processor is considered. The results are provided in terms of the SNR, INR, and the projections between the desired, presumed and interference steering vectors.

Consider the estimated correlation matrix given by

$$\widehat{\mathbf{R}} = \sigma_d^2 \mathbf{s}_d \mathbf{s}_d^H + \sigma_i^2 \mathbf{s}_i \mathbf{s}_i^H + (\sigma_n^2/N) \mathbf{I}, \quad (6.33)$$

where  $\sigma_d^2$ ,  $\sigma_i^2$ ,  $\sigma_n^2$  are desired signal, interference and noise power, and  $\mathbf{s}_d$  and  $\mathbf{s}_i$  are desired signal and interference vectors, respectively. For the spatial processor the presumed steering vector has the form

$$\mathbf{s}_m = \sqrt{1/N} \begin{bmatrix} 1 \\ e^{j2\pi\psi_m} \\ \vdots \\ e^{j2\pi(N-1)\psi_m} \end{bmatrix}, \quad (6.34)$$

where  $N$  is the number of antenna elements.  $\psi_m$  is the normalized spatial frequency of the presumed look direction, and it is related to the presumed target angle,  $\theta_m$ , by:

$$\psi_s = \frac{d \sin \theta_d}{\lambda}, \quad (6.35)$$

where  $\lambda$  is the wavelength of the transmitted signal and  $\theta_d$  is angle of the target. The desired signal vector has the form

$$\mathbf{s}_d = \frac{1}{|\mathbf{c}|} \begin{bmatrix} c_0 \\ c_1 e^{j2\pi\psi_d} \\ \vdots \\ c_{N-1} e^{j2\pi(N-1)\psi_d} \end{bmatrix} \quad \text{and} \quad \mathbf{c} = \begin{bmatrix} c_0 \\ c_1 \\ \vdots \\ c_{N-1} \end{bmatrix}, \quad (6.36)$$

where  $c$  is a complex random variable with Gaussian-distributed magnitude and phase. The vector  $\mathbf{c}$  is used to model the amplitude and phase errors. Assuming good calibration, both the magnitude and the phase of  $c_l$  have small variance. The mean of the magnitude is  $\sqrt{1/N}$  and the mean of the phase error is zero. In case of the ideal calibration,  $c_l = \sqrt{1/N}$ . The difference between the true target angle and presumed target angle,  $\theta_m - \theta_d$ , is the pointing error. Under ideal conditions (no errors), the desired signal vector equals the presumed steering vector. Since the interference signal goes through the same channels as the desired signal, the interference steering vector has the form

$$\mathbf{s}_i = \frac{1}{|\mathbf{c}|} \begin{bmatrix} c_0 \\ c_1 e^{j2\pi\psi_i} \\ \vdots \\ c_{N-1} e^{j2\pi(N-1)\psi_i} \end{bmatrix}, \quad (6.37)$$

where  $\psi_i$  is the normalized spatial frequency of the interference. The projections between the steering vectors are defined as

$$\rho_{md} = \mathbf{s}_m^H \mathbf{s}_d, \quad \rho_{mi} = \mathbf{s}_m^H \mathbf{s}_i \quad \text{and} \quad \rho_{id} = \mathbf{s}_i^H \mathbf{s}_d. \quad (6.38)$$

Without loss of generality, assume  $\sigma_n^2 = N$ . Then,  $\widehat{\mathbf{R}}$  can be written as

$$\widehat{\mathbf{R}} = \sigma_d^2 \mathbf{s}_d \mathbf{s}_d^H + \sigma_i^2 \mathbf{s}_i \mathbf{s}_i^H + \mathbf{I} \quad (6.39)$$

In terms of its eigenvectors,  $\widehat{\mathbf{R}}$  is given by

$$\widehat{\mathbf{R}} = (\lambda_1 - 1) \mathbf{q}_1 \mathbf{q}_1^H + (\lambda_2 - 1) \mathbf{q}_2 \mathbf{q}_2^H + \mathbf{I}, \quad (6.40)$$

where  $\mathbf{q}_l$  is the  $l^{th}$  eigenvector and  $\lambda_l$  is the  $l^{th}$  eigenvalue for  $l \in [1, 2]$ . For  $l \in [3, N]$ , the eigenvalues are equal to 1. The signal-plus-interference subspace is 2-dimensional and the noise subspace is  $(N - 2)$ -dimensional. Using  $\sigma_i^2$ ,  $\sigma_d^2$ , and  $\rho_{id}$  (see Appendix A), first two eigenvalues of  $\widehat{\mathbf{R}}$  are given by

$$\lambda_{1,2} = \frac{\sigma_i^2 + \sigma_d^2}{2} \left( 1 \pm \sqrt{1 - \frac{4\sigma_i^2\sigma_d^2(1 - |\rho_{id}|^2)}{(\sigma_i^2 + \sigma_d^2)^2}} \right) + 1. \quad (6.41)$$

The eigenvectors corresponding to these eigenvalues are given by

$$\mathbf{q}_{1,2} = \frac{\mathbf{s}_d + \alpha_{1,2} \mathbf{s}_i}{\sqrt{1 + |\alpha_{1,2}|^2 + 2\operatorname{Re}(\alpha_{1,2} \rho_{id}^*)}}, \quad (6.42)$$

where  $\alpha$  is

$$\alpha_{1,2} = \frac{\lambda_{1,2} - \sigma_d^2}{\sigma_d^2 \rho_{id}^*} = \frac{\sigma_i^2 \rho_{id}}{\lambda_{1,2} - \sigma_i^2}. \quad (6.43)$$

The inverse of the estimated correlation matrix is given by

$$\widehat{\mathbf{R}}_x^{-1} = \mathbf{I} - \beta_1 \mathbf{q}_1 \mathbf{q}_1^H - \beta_2 \mathbf{q}_2 \mathbf{q}_2^H, \quad (6.44)$$

where

$$\beta_{1,2} = \frac{\lambda_{1,2} - 1}{\lambda_{1,2}}. \quad (6.45)$$

The AIF for SMI is calculated using (6.27) and (2.7) as follows:

$$G_{smi} = \frac{|\mathbf{s}_m^H \widehat{\mathbf{R}}_x^{-1} \mathbf{s}_d|^2}{\mathbf{s}_m^H \widehat{\mathbf{R}}_x^{-1} \mathbf{R}_{i+n} \widehat{\mathbf{R}}_x^{-1} \mathbf{s}_m}, \quad (6.46)$$

where

$$\mathbf{R}_{i+n} = \sigma_i^2 \mathbf{s}_i \mathbf{s}_i^H + \mathbf{I}. \quad (6.47)$$

The numerator of  $G_{smi}$  is given by

$$|\mathbf{s}_m^H \widehat{\mathbf{R}}_x^{-1} \mathbf{s}_d|^2 = |\rho_{md} - \beta_1 \mathbf{s}_m^H \mathbf{q}_1 \mathbf{q}_1^H \mathbf{s}_d - \beta_2 \mathbf{s}_m^H \mathbf{q}_2 \mathbf{q}_2^H \mathbf{s}_d|^2, \quad (6.48)$$

and the denominator is given by

$$\begin{aligned}
\mathbf{s}_m^H \widehat{\mathbf{R}}_x^{-1} \mathbf{R}_{i+n} \widehat{\mathbf{R}}_x^{-1} \mathbf{s}_m = & 1 + \sigma_i^2 |\rho_{mi}|^2 \\
& + (\beta_1^2 - 2\beta_1 + \beta_1^2 \sigma_i^2 |\mathbf{q}_1^H \mathbf{s}_i|^2) \mathbf{s}_m^H \mathbf{q}_1 \mathbf{q}_1^H \mathbf{s}_m \\
& + (\beta_2^2 - 2\beta_2 + \beta_2^2 \sigma_i^2 |\mathbf{q}_2^H \mathbf{s}_i|^2) \mathbf{s}_m^H \mathbf{q}_2 \mathbf{q}_2^H \mathbf{s}_m \\
& + 2\beta_1 \beta_2 \sigma_i^2 \operatorname{Re}(\mathbf{s}_m^H \mathbf{q}_1 \mathbf{q}_1^H \mathbf{s}_s \mathbf{s}_s^H \mathbf{q}_2 \mathbf{q}_2^H \mathbf{s}_m) \\
& - 2\sigma_i^2 \beta_1 \operatorname{Re}(\mathbf{s}_s^H \mathbf{q}_1 \mathbf{q}_1^H \mathbf{s}_m \rho_{mi}) \\
& - 2\sigma_i^2 \beta_2 \operatorname{Re}(\mathbf{s}_s^H \mathbf{q}_2 \mathbf{q}_2^H \mathbf{s}_m \rho_{mi}).
\end{aligned} \tag{6.49}$$

In the same manner, the array gain for the eigencanceler is calculated using (6.27) and (4.2), with  $r = 1$  (single interference), as follows:

$$G_{eig} = \frac{|\mathbf{s}_m^H (\mathbf{I} - \mathbf{q}_1 \mathbf{q}_1^H) \mathbf{s}_d|^2}{\mathbf{s}_m^H (\mathbf{I} - \mathbf{q}_1 \mathbf{q}_1^H) \mathbf{R}_{i+n} (\mathbf{I} - \mathbf{q}_1 \mathbf{q}_1^H) \mathbf{s}_m}. \tag{6.50}$$

The numerator of  $G_{eig}$  is given by

$$|\mathbf{s}_m^H (\mathbf{I} - \mathbf{q}_1 \mathbf{q}_1^H) \mathbf{s}_d|^2 = |\rho_{md} - \mathbf{s}_m^H \mathbf{q}_1 \mathbf{q}_1^H \mathbf{s}_d|^2, \tag{6.51}$$

and the denominator is given by

$$\mathbf{w}_{eig}^H \mathbf{R}_{i+n} \mathbf{w}_{eig} = 1 + \sigma_i^2 |\rho_{mi}|^2 + (\sigma_i^2 |\mathbf{s}_i^H \mathbf{q}_1|^2 - 1) |\mathbf{s}_m^H \mathbf{q}_1|^2 - 2 \operatorname{Re}(\sigma_i^2 \rho_{mi} \mathbf{s}_i^H \mathbf{q}_1 \mathbf{q}_1^H \mathbf{s}_m). \tag{6.52}$$

To study the effects of the SNR, INR, calibration and pointing errors, the  $G_{smi}$  and  $G_{eig}$  are plotted. For all of the plots  $\sigma_n^2 = N$ , where  $N = 14$ , and the  $G_{smi}$  and  $G_{eig}$  are normalized by  $N$ .

In Figure 6.7,  $G_{smi}$  and  $G_{eig}$  are plotted as a function of the presumed target angle,  $\theta_d$ , for the case of ideal phase and gain calibration,  $c_i = \sqrt{1/N}$ . In Figure 6.7(a), the correlation matrix has no signal component,  $\sigma_d^2 = 0$ . Under these conditions, SMI is the optimal solution, since  $\widehat{\mathbf{R}}$  is the true correlation matrix of the interference and Gaussian noise. The  $G_{smi}$  and  $G_{eig}$  overlap for  $\sigma_i^2 = 1400$  (INR = 20 dB). In Figure 6.7(b) the desired signal component is present in the correlation matrix,  $\sigma_d^2 = 140$  (SNR = 10 dB). For this case, SMI works only if  $\theta_m = \theta_d$ . A slight pointing error causes a large decrease in the AIF. The eigencanceler, however, is much less affected by the increase of the SNR.

In Figure 6.8, effects of the phase errors, and pointing error are studied. There are no amplitude errors,  $|c_i| = \sqrt{1/N}$ , and the phase errors are modeled as a zero-mean Gaussian random variable. Phase errors are averaged over 50 iterations. As the standard deviation (STD) of the phase errors increases,  $G_{smi}$  starts to decrease, due to the mismatch between the desired and presumed steering vectors. The mainlobe is again very narrow due to the presence of the desired signal. The eigencanceler is very robust against the phase errors as seen in Figure 6.8(b), where the mainlobe is hardly changed even for high phase errors.

In Figure 6.9, effects of the amplitude errors and pointing error are investigated. There are no phase errors,  $\angle c_i = 0$ . The STD of the amplitude errors are normalized by the mean of the amplitude, which is  $1/\sqrt{N}$ . Again the SMI method performs if there are no pointing errors

and the STD of the amplitude errors are very small. Performance is degraded, however, if the STD of amplitude errors are increased or a small pointing error is introduced. The eigencanceler is again robust with respect to amplitude errors and maintains the ideal shape for the mainlobe shape even with amplitude errors of 10% STD from the mean. To generate these plots, 50 iterations are used for every point.

In Figure 6.10, effects of the desired signal power,  $\sigma_d^2$ , on the pointing error is studied. There are no phase and amplitude errors,  $c_i = \sqrt{1/N}$ . When the  $\sigma_d^2 = 0$ , both  $G_{smi}$  and  $G_{eig}$  have the same mainlobe as Figure 6.7(a), which is the ideal solution. As the desired signal power is increased, the SMI's mainlobe becomes narrower and the performance is decreased for even a small pointing error. The eigencanceler's performance is acceptable up to a SNR of 10 dB, but  $G_{eig}$  goes down rapidly as the SNR gets closer to the INR. This behavior is due to the shift of the first eigenvector, which starts to look like the desired signal as the SNR approaches the INR. When the SNR is equal to the INR, the eigencanceler fails even when there are no pointing errors, because the first eigenvector has a large projection on the desired signal, which causes desired signal cancelation.

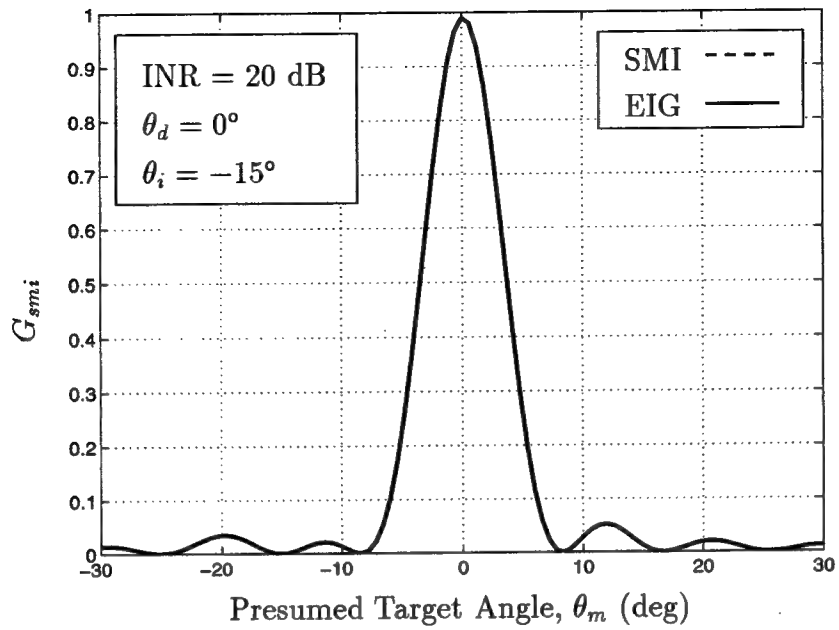
In Figure 6.11, effects of the desired signal angle on the pointing errors is plotted. The desired signal angle does not have a very significant effect on the shape of the mainlobe. As seen in Figure 6.11(b), the mainlobe gets slightly larger as the desired signal angle is increased. This is due to the nonlinear mapping, from the physical to the electrical angle, given by (6.35). As  $\theta_d$  gets larger, the electrical pointing error is smaller for the same physical pointing error. Therefore, the mainlobe related to the electrical pointing errors becomes larger.

## 6.5 Mountaintop Data Analysis

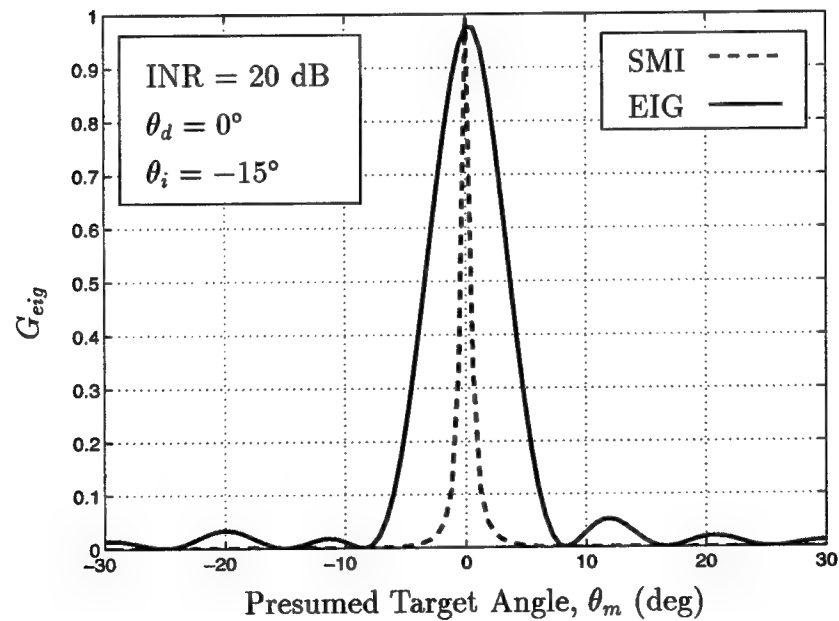
Analytical results presented in the previous sections show that the eigencanceler is robust with respect to steering vector perturbations. In this chapter, the performance of the eigencanceler and SMI are compared using the Mountaintop dataset. After describing the specific data file used, range detection with corresponding antenna response and angle detection of the target are studied. Training sets of different sizes from different regions are used. The last section considers the signal suppression issue when the cell under test is included in the training.

### 6.5.1 Description of the Data Files

Data analysis was done on IDPCA data recorded on Feb 10, 1994 at North Oscura Peak, White Sands Missile Range (WSMR), New Mexico. For this data set, namely t38pre01v1.mat, IDPCA was used to emulate clutter at 245° and 156 Hz in Doppler. The injected target is at 154 km in range, 275° in angle, and 156 Hz in Doppler. The bore side angle is 260°. The transmitted pulse is an LFM signal with 500 KHz of bandwidth, a central frequency of 435 MHz, and a 100  $\mu$ s duration. Distance between the elements is half the wavelength,  $d = \lambda/2$ . Recorded data is sampled at the Nyquist rate of 1 MHz. The PRI is 1600  $\mu$ s, which gives a pulse repetition frequency (PRF) of 625 Hz. Data is recorded from 865  $\mu$ s to 1298  $\mu$ s after the pulse is transmitted, corresponding to range cells from 130 km to 195 km with a range resolution of 150 m. Data is recorded into CPI's

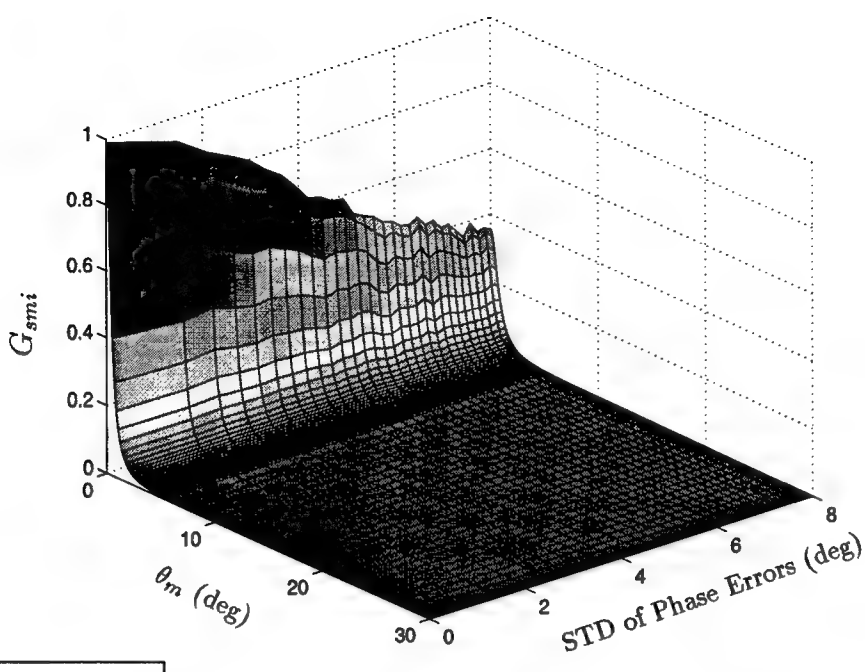


(a) No Desired Signal Component,  $\sigma_d^2 = 0$



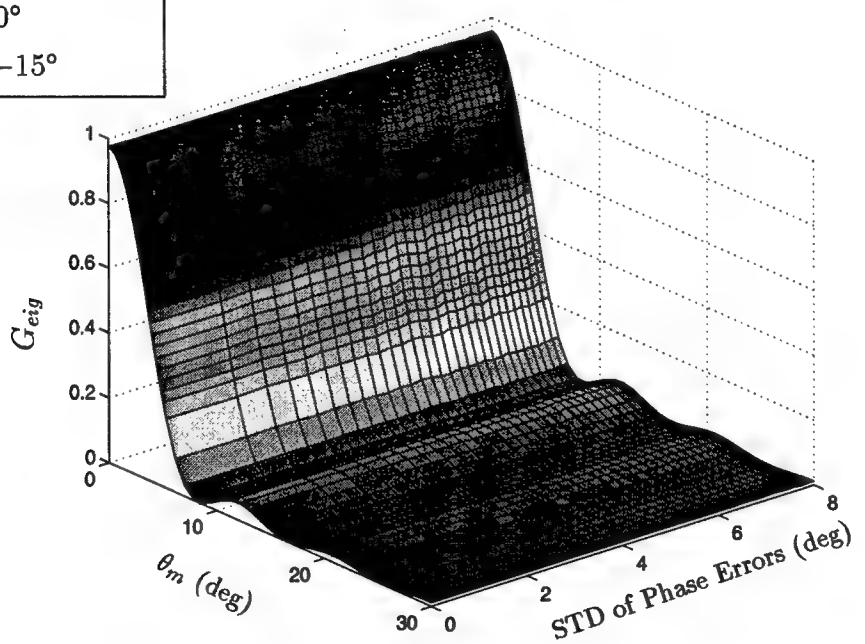
(b) With Desired Signal Component,  $\sigma_d^2 = 10$

**Figure 6.7** Effects of Desired Signal Component and Pointing Error on the AIF



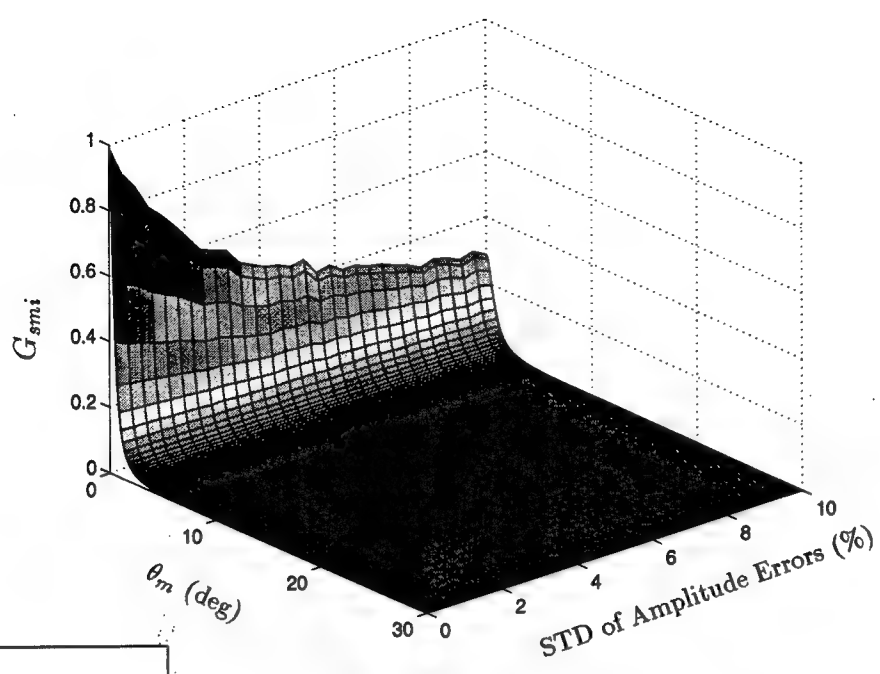
$\text{SNR} = 10 \text{ dB}$   
 $\text{INR} = 20 \text{ dB}$   
 $\theta_d = 0^\circ$   
 $\theta_i = -15^\circ$

(a) Sample Matrix Inversion



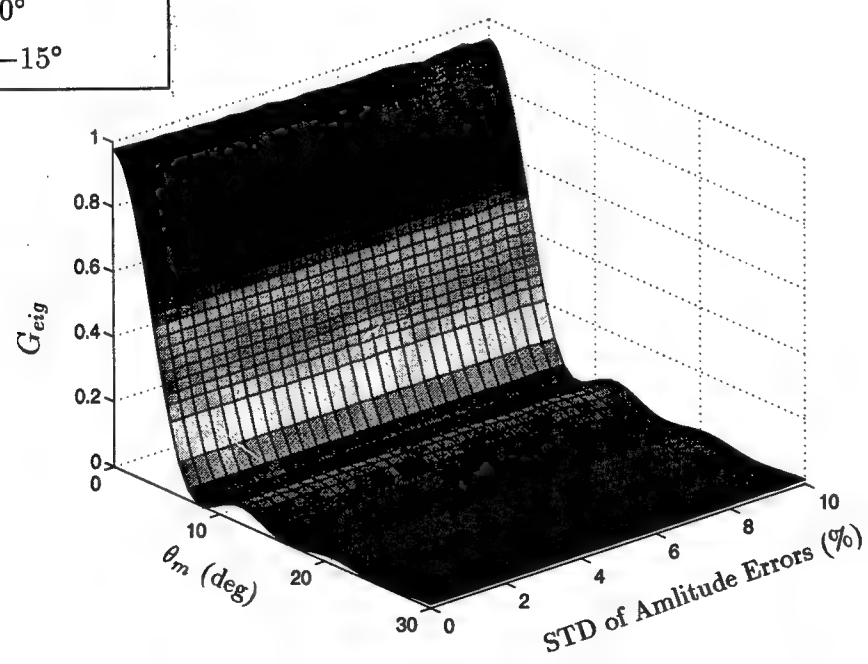
(b) Eigencanceler

**Figure 6.8** Effects of Phase Errors and Pointing Error on the AIF



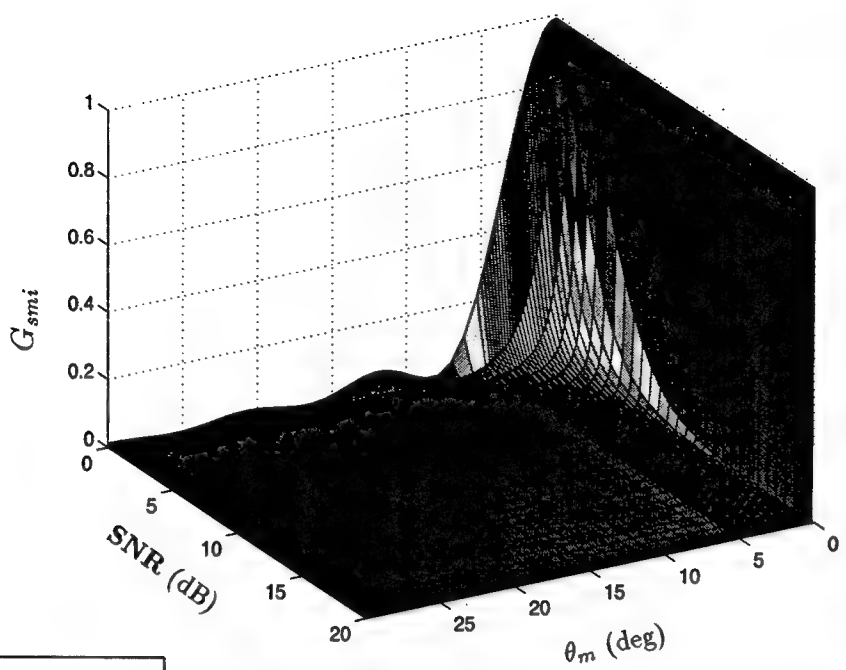
(a) Sample Matrix Inversion

$\text{SNR} = 10 \text{ dB}$   
 $\text{INR} = 20 \text{ dB}$   
 $\theta_d = 0^\circ$   
 $\theta_i = -15^\circ$

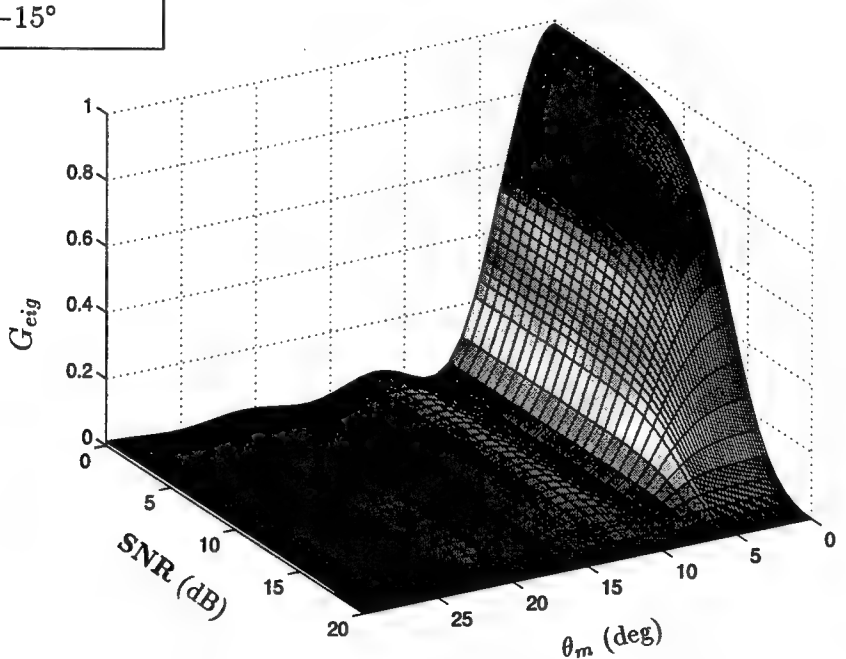


(b) Eigencanceler

**Figure 6.9** Effects of Amplitude Errors and Pointing Error on the AIF

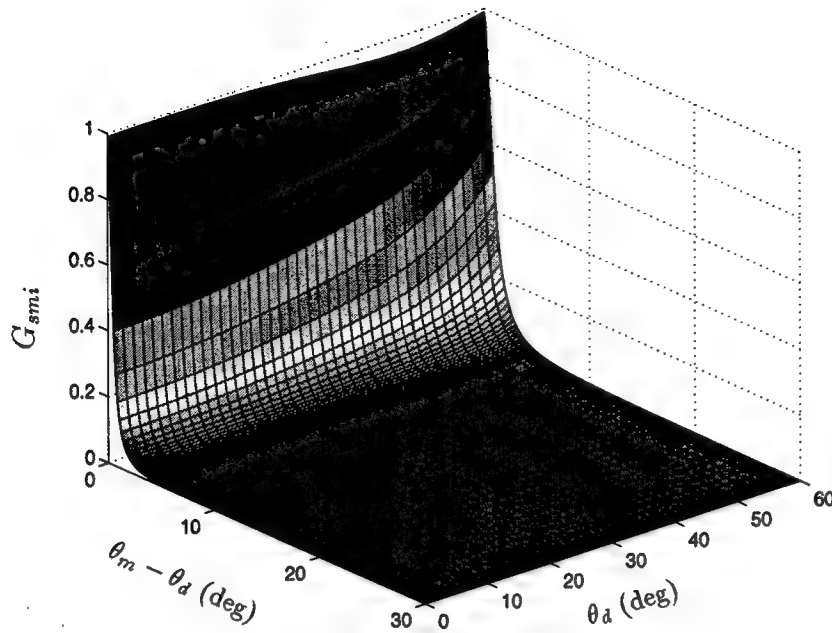


(a) Sample Matrix Inversion



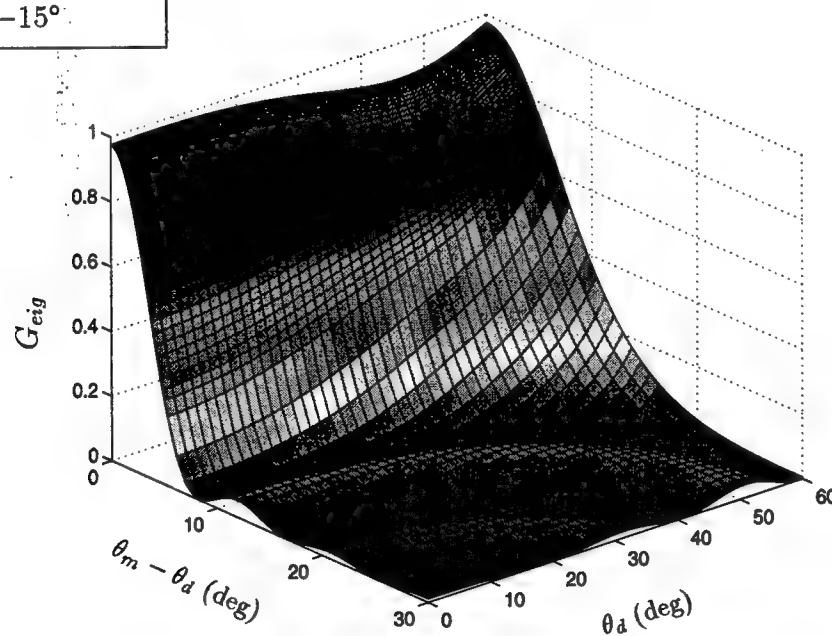
(b) Eigencanceler

**Figure 6.10** Effects of Signal-to-Noise Ratio and Pointing Error on the AIF



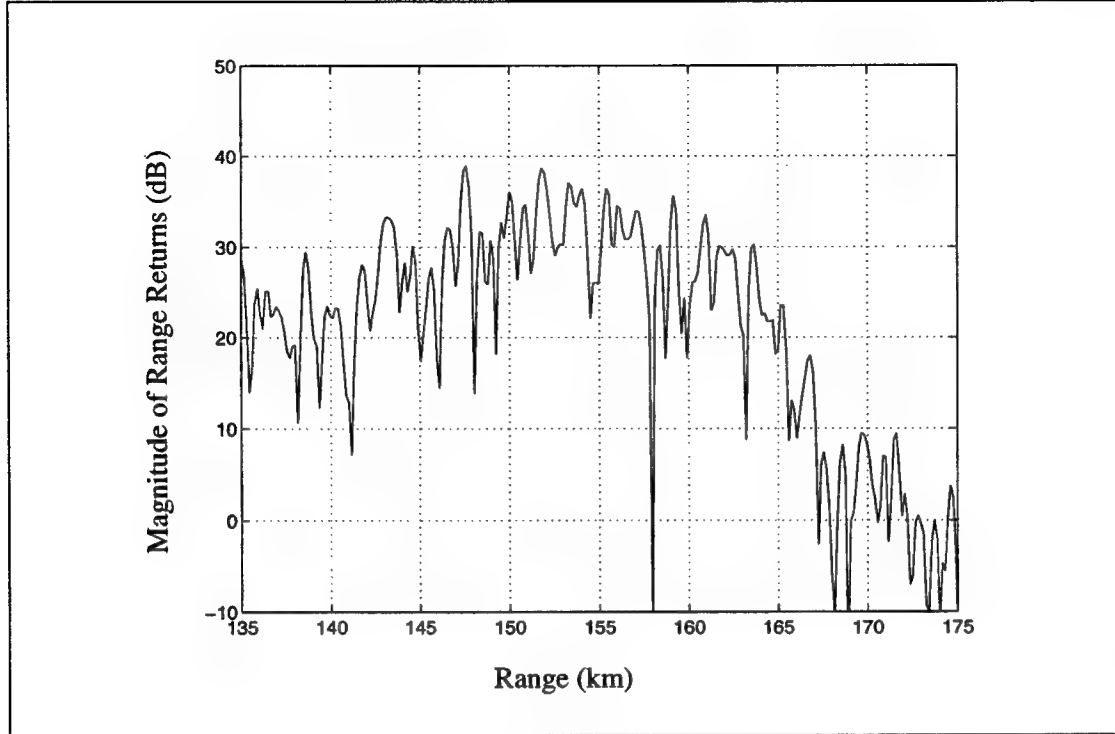
$\text{SNR} = 10 \text{ dB}$   
 $\text{INR} = 20 \text{ dB}$   
 $\theta_i = -15^\circ$

(a) Sample Matrix Inversion



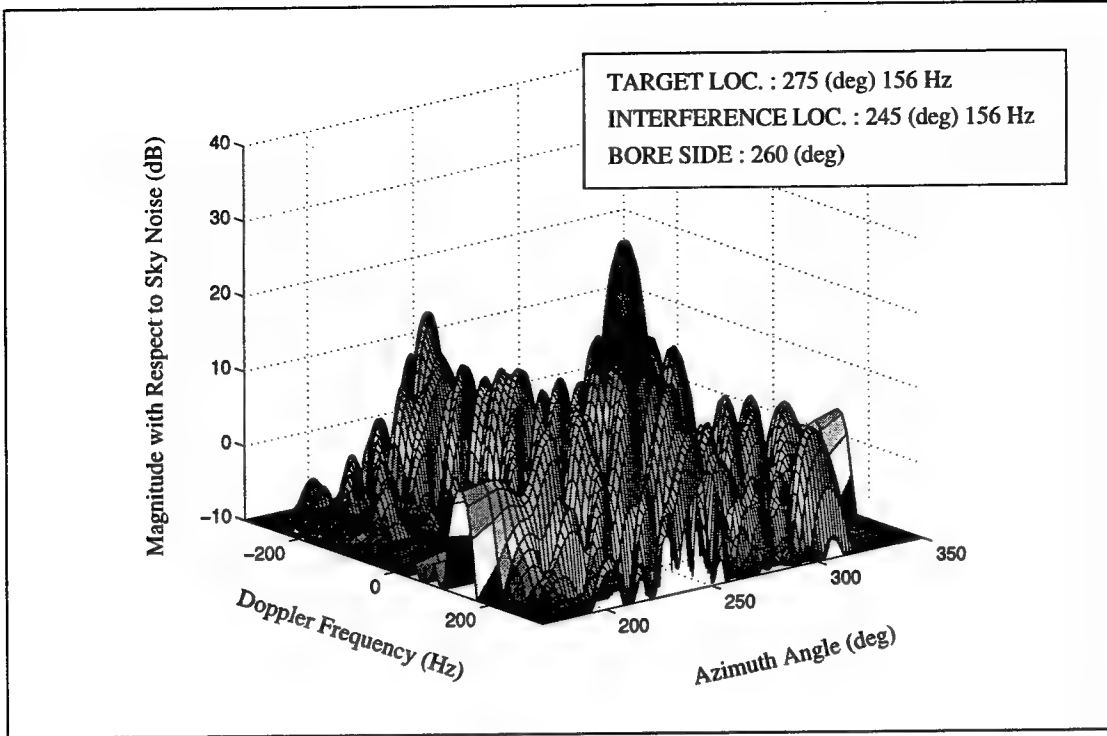
(b) Eigencanceler

Figure 6.11 Effects of Desired Signal Angle and Pointing Error on the AIF



**Figure 6.12** Magnitude Plot of Range Returns on IDPCA Data, CPI 6, PRI 1

with 16 PRI's. Using (6.14), the normalized Doppler frequency of the target is 0.250. Since 14 antennas are employed, there are 14 samples in space. For each range cell a  $16 \times 14$  space-time data matrix is formed. Using (6.35), the normalized spatial frequency of the target is 0.129 and the normalized spatial frequency of the interference is  $-0.129$ . Notice that both the target and the interference are at the same Doppler frequency, and they are only separated spatially. Using CPI 6 of the data, the magnitude of the first PRI as a function of range is plotted in Figure 6.12. The returns from the ranges are plotted with respect to the sky noise level. The clutter is located from 140 km to 165 km. In Figure 6.13, the Doppler-azimuth plot of the target range cell at 154 km is plotted. As expected, the energy is concentrated at 156 Hz and  $245^\circ$  due to the interference power. To study the eigenvalue distribution of joint-domain processing, each range matrix is reshaped to a joint-domain stacked data vector of size  $224 \times 1$ . To estimate the correlation matrix, 1200 training data vectors from matrix CPI's 6, 7, 8 and 9 were used. The eigenvalues of this correlation matrix are plotted in Figure 6.14(a), where the few interference eigenvalues are well above the sky noise level. For post-Doppler processing, each range data matrix is first processed temporally with the non-adaptive weight vector, which has the form of  $s_t$  in (6.20). Then beamforming algorithms are applied to the  $14 \times 1$  spatial data vectors. The correlation matrix of post-Doppler data is estimated using 300 data points from CPI 6. The eigenvalues are plotted in Figure 6.14(b), where most of the energy is concentrated in the first 4-5 eigenvectors.

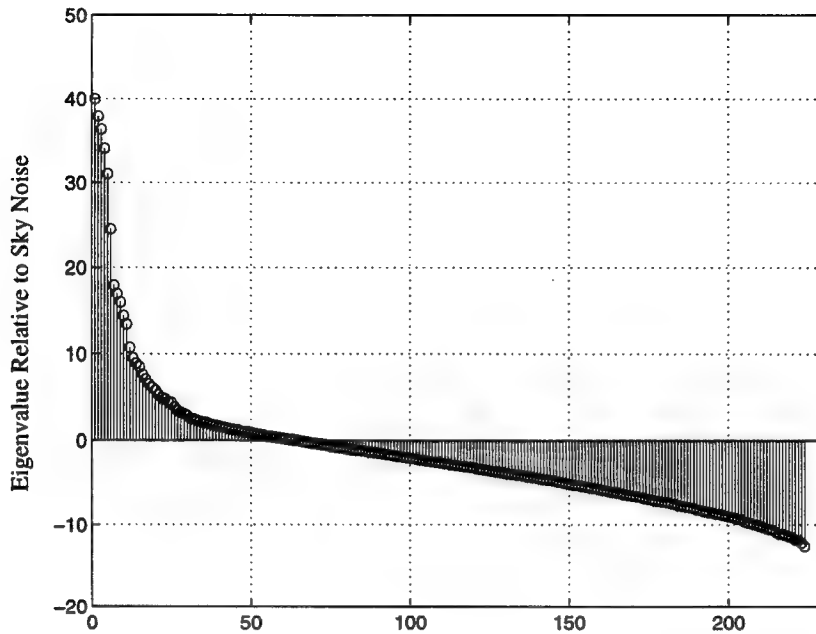


**Figure 6.13** Doppler-Azimuth Plot for Target Range Cell

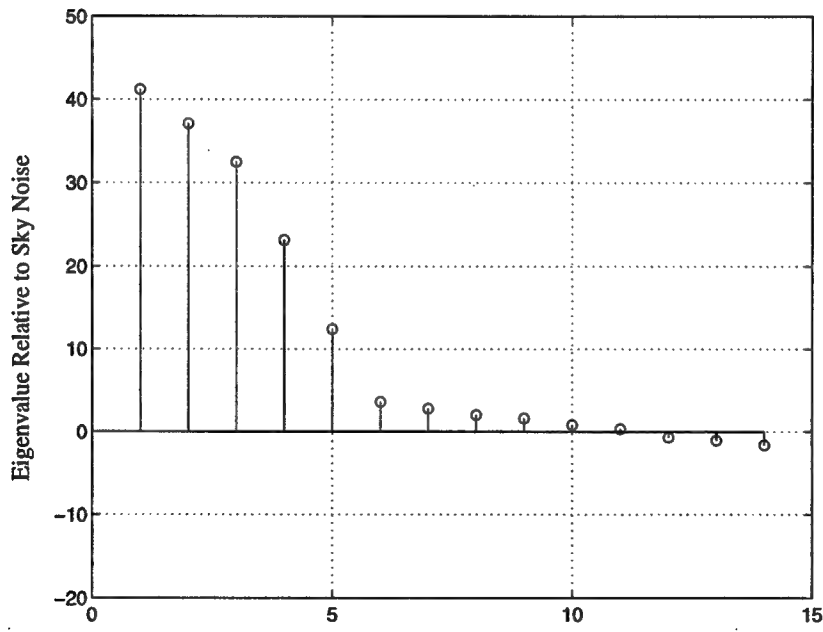
### 6.5.2 Target Range Detection

In this section, the target angle and Doppler frequency are assumed to be known and the target range is detected. The data is plotted relative to sky noise. Sky noise data, namely ncal585v1.mat, is recorded right after the experiment with the transmitter turned off. To calculate the sky noise level at the output of the beamformer, the weights calculated for a specific experiment are applied to the sky noise data. The mean of the sky noise output is taken as the sky noise reference. If the beamformer is adaptive, the weight vector changes with the training region and number of points used. For every plot, the sky noise level is updated using the corresponding weight vector. For these plots CPI 6 is used, which has 300 data vectors.

First, the joint-domain processor with 14 antenna elements and 4 PRIs is studied. The joint-domain data vector for this case is  $56 \times 1$ . In Figure 6.15(a), training is done over 300 points from 135 km to 175 km, and the target range cells are excluded from the training set. The target is located at 154 km and the power of the target spills over 5 range cells. Clearly, the non-adaptive beamformer fails due to a large sidelobe. Both SMI and the eigencanceler have the same performance. But this is not a realistic approach since *a-priori* knowledge of the target location was used when estimating the correlation matrix. A more realistic approach is given in Figure 6.15(b), where all the data vectors are used for training, including the target region. Presence of the target region in the training set causes an increase in the desired signal component of the estimated correlation matrix. The SMI method fails to preserve the desired signal, and signal cancellation of 12 dB is observed. Performance of the eigencanceler is not affected by high signal power in the estimate.



(a) Joint Domain



(b) Time-Space

**Figure 6.14** Eigenvalues of the Data

Next, the post-Doppler beamformer is studied. After temporal processing, the post-Doppler data vectors are  $14 \times 1$ . In Figure 6.16(a), training is over 300 data points, and the target region is not included in the estimate. The performance of the post-Doppler processor is better than the joint-domain processor because both the desired signal and the interference have the same Doppler frequency. The joint-domain processor, which is adaptive both in time and space, cancels the interference temporally and spatially. Because the interference and target signal are in the same Doppler bin, some signal power is lost. The post-Doppler processor performs cancelation in the spatial domain, where the target and interference are separated. Therefore, the post-Doppler processor performs better for this specific data set. In Figure 6.16(b), the target region is included in the training. The SMI method is affected by the high desired signal component and the performance is degraded by 7 dB. The eigencanceler, on the other hand, is not affected by the presence of the desired signal, as shown analytically in section 6.4 and plotted in Figure 6.10. In Figure 6.17, training with 50 data points is considered. In part (a), the training is done from 145 km to 152 km, which is outside the target region. Both adaptive methods cancel most of the clutter. The non-adaptive beamformer output does not change due to the fixed weights, and it is plotted again as the clutter reference. An important observation is that the SMI method performs more cancelation around the training region. This is due to the limited number of training samples, which causes a correlation matrix to be a good estimate of the training region, but very bad estimate globally. In parts (b) and (c), the training is done around the target region from 150 km to 158 km. As before, when the target is omitted from the training set, a very good performance is observed. Again the training region is nulled by the SMI method, where the eigencanceler lowers the output but does not null out. In part (c), where the target is included in the training set, the SMI method fails by treating the desired signal as interference. Unlike the SMI, the eigencanceler does not null out the desired signal, but the interference cancelation of the eigencanceler is degraded. Presence of the desired signal shifts the largest eigenvectors towards the desired signal, causing a corrupt estimation of the interference subspace. In Figure 6.18, training with 28 points-double the vector size-is considered. This is the lower limit for SMI to work. In part (a), a deeper null is placed by the SMI method in the training region. The performance of the eigencanceler is better than SMI, which shows that the eigencanceler has a faster convergence rate. In part (c), both methods fail. The signal cancelation problem of the SMI is magnified. The eigencanceler still manages to save some of the signal power, but fails to cancel the interference. In fact, interference cancelation is worse than with the non-adaptive method from 140 km to 150 km.

### 6.5.3 Antenna Pattern

In this section, the spatial response of the weights calculated for the post-Doppler range plots of the previous section is studied. Assuming an ideal desired signal, the spatial data vector will have the form of  $\mathbf{s}_s$  in (6.34). The normalized spatial frequency,  $\psi_s$ , is related to the physical angle by (6.35). The antenna patterns are generated by applying a given weight vector to steering vectors for different angles. A desirable weight vector has a main

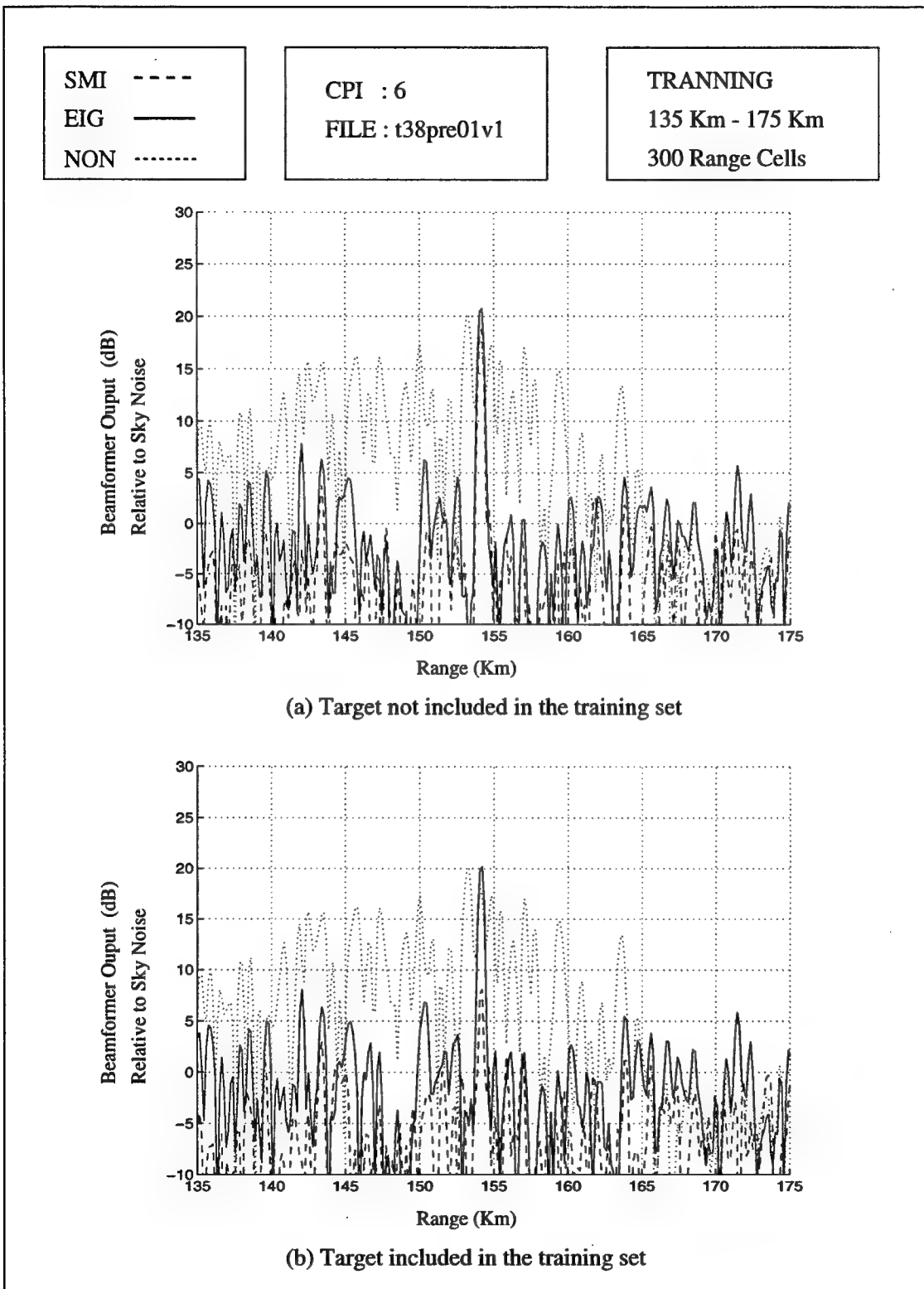


**Figure 6.15 Joint-Domain Range Plots Using 300 Training Points**

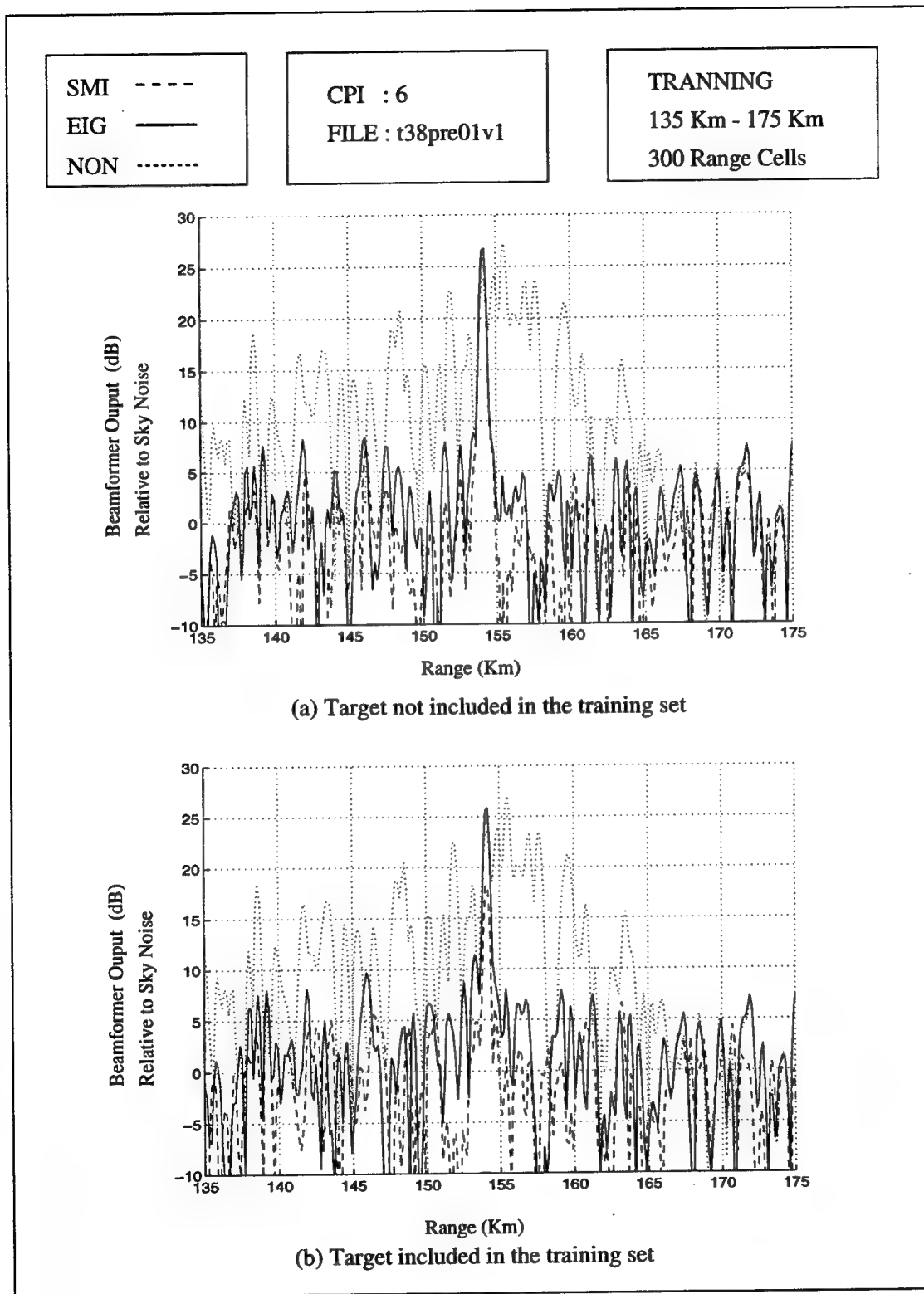


**Figure 6.16** Post-Doppler Range Plots Using 300 Training Points

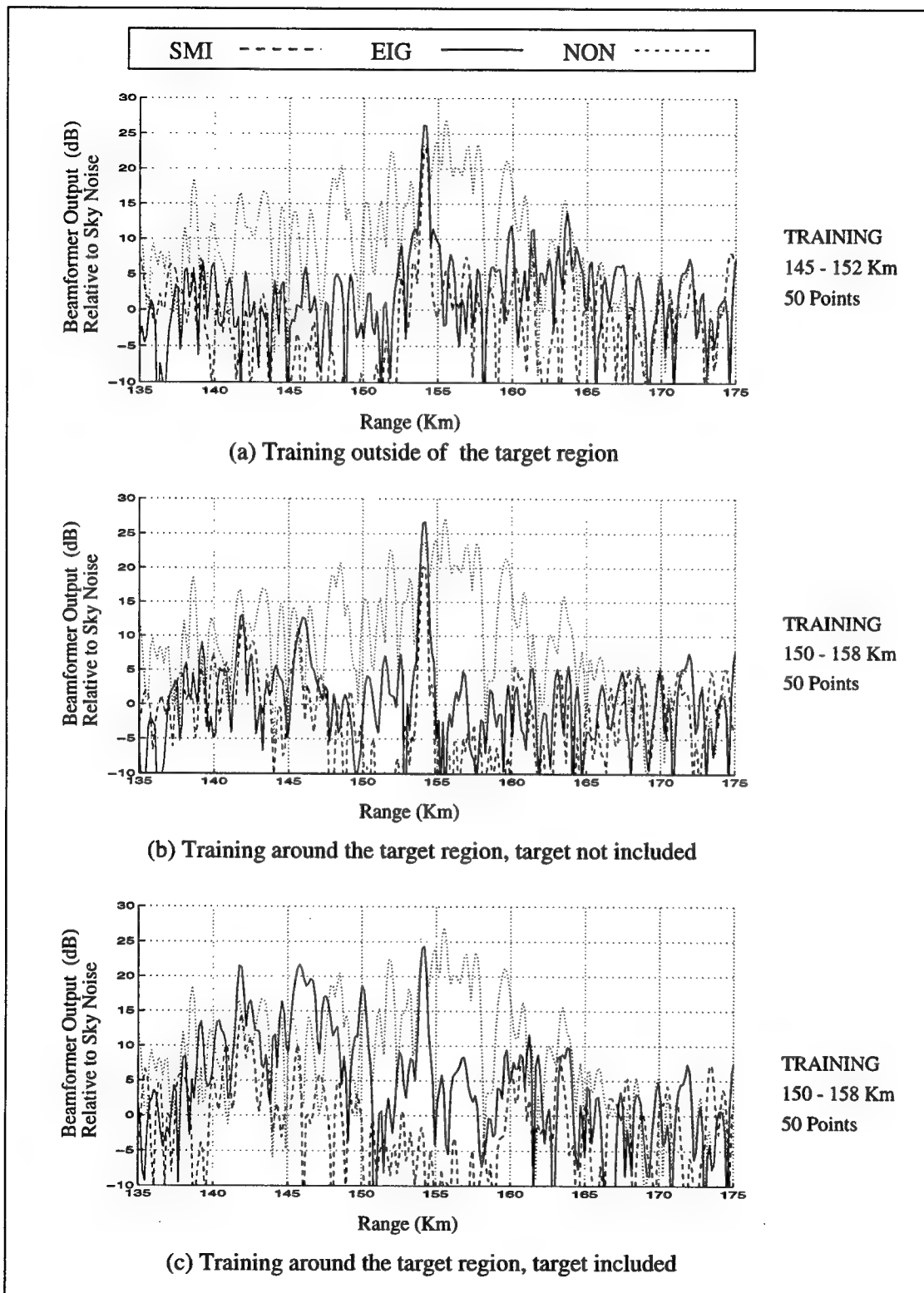


**Figure 6.17** Post-Doppler Range Plots Using 50 Training Points

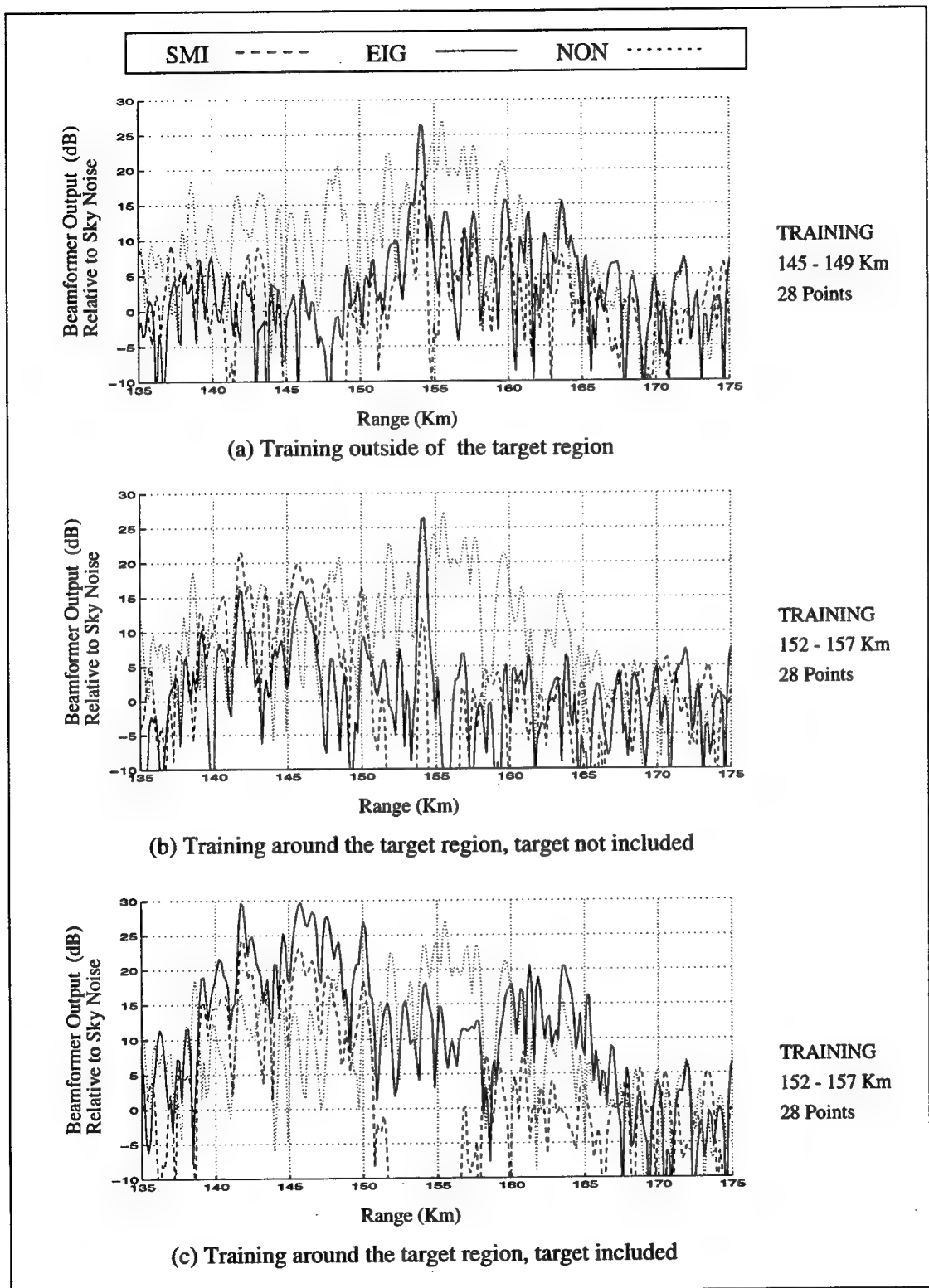


**Figure 6.18** Post-Doppler Range Plots Using 28 Training Points

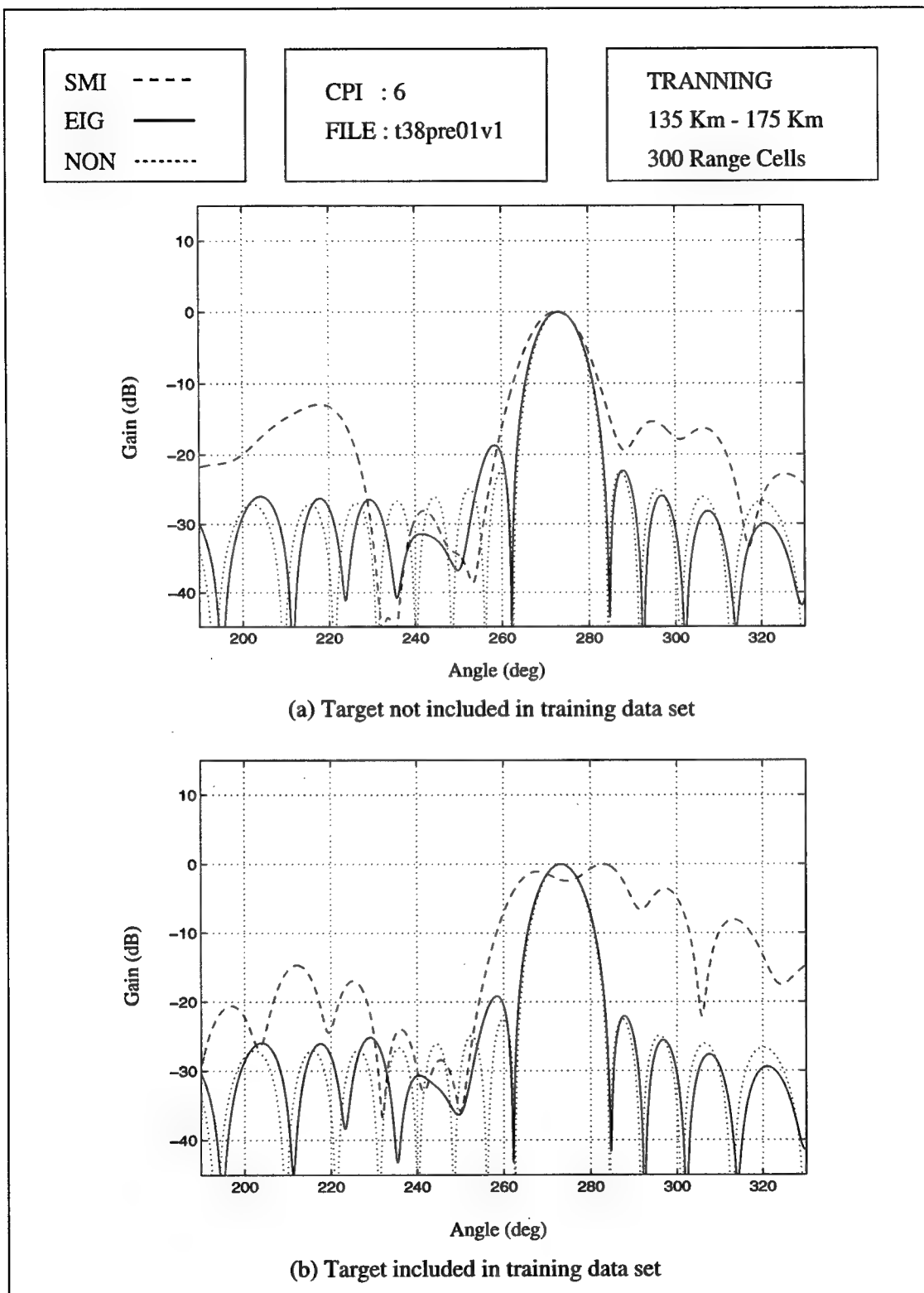


**Figure 6.19 Post-Doppler Antenna Pattern Plots Using 300 Training Points**

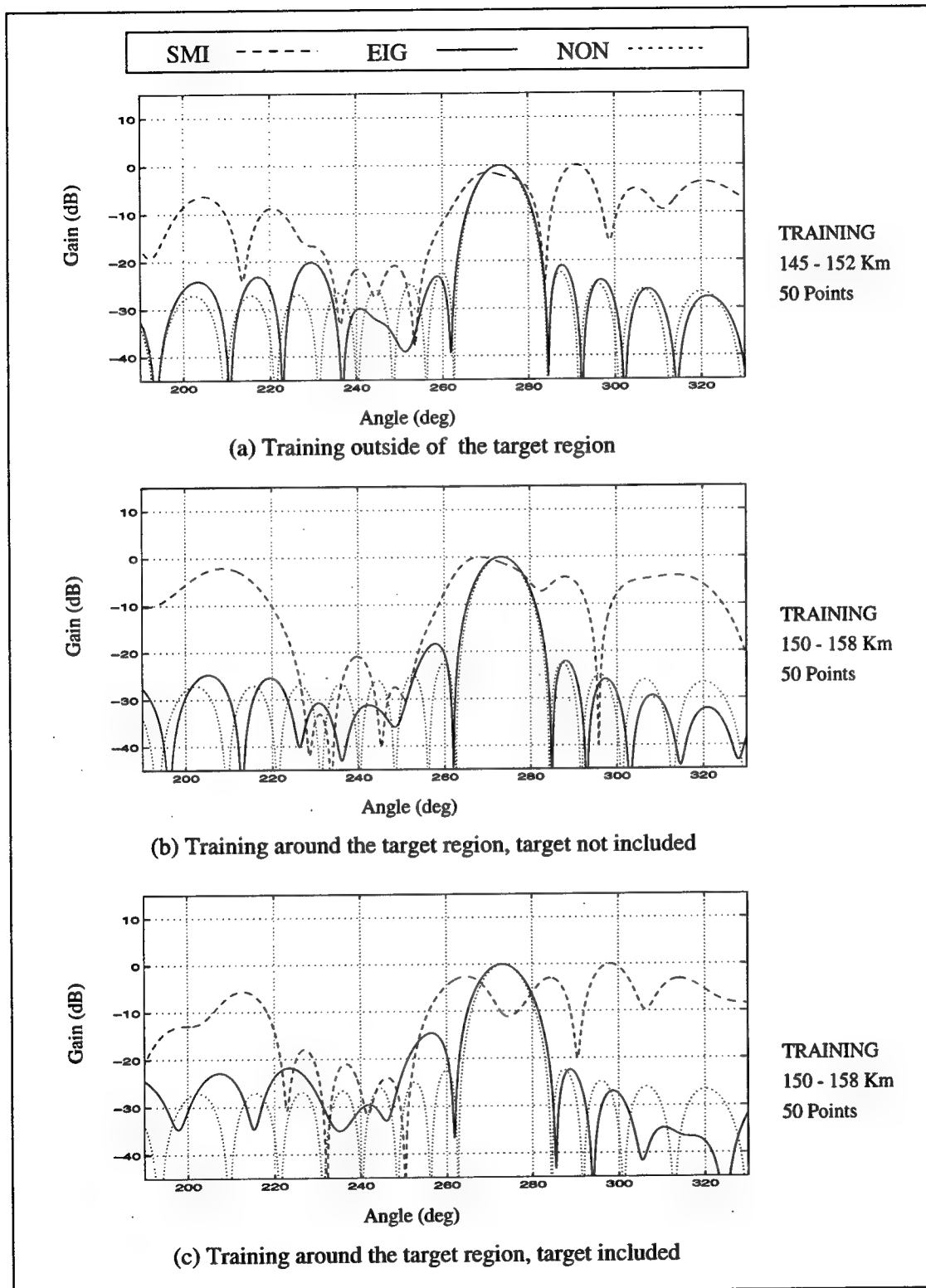


**Figure 6.20** Post-Doppler Antenna Pattern Plots Using 50 Training Points

lobe in the direction of the target and a null in the direction of the interference. In this data set the target angle is  $275^\circ$  and the interference angle is  $245^\circ$ .

In Figure 6.19, the response of the weight vectors calculated with 300 training points are plotted. The non-adaptive weight vector, plotted for reference, is the presumed steering vector for the desired signal. Around the interference angle, both adaptive beamformers have a lower sidelobe than the non-adaptive beamformer. In part (b), the target region included in the estimate, the SMI method puts a small notch on the main lobe causing the performance degradation observed in the range plots of the previous section. The eigencanceler's sidelobes resemble the non-adaptive weight vector, except in the interference region. Comparing both parts, the eigencanceler is not affected by the presence of the desired signal in the estimate. In Figure 6.20, the response of the weight vector calculated with 50 training points is plotted. In part (a), a decrease in the training set number has affected the SMI method with increased sidelobes, but the eigencanceler manages to keep the same shape. Even though interference cancellation of the eigencanceler is degraded, we also observe from range plot for the same training that the main lobe is still in the right direction and the sidelobes are relatively low, keeping the shape of the steering vector. Compared to part (b) of the previous figure, the small notch introduced by SMI on the desired signal in part (c) is even deeper.

When the training set is lowered to 28 range cells, see Figure 6.21, the SMI method does not give a desirable antenna pattern even for the case of training outside of the target region. The eigencanceler's performance is still preserved in part (a). In addition, as mentioned before for the range plots with the target included in training in part (c), both adaptive methods fail and performance is worse than the non-adaptive beamformer.

#### 6.5.4 Target Angle Detection

In this section, the target range and the Doppler frequency are assumed to be known, and the target angle is detected. The post-Doppler data vector for the target range cell at 154 km is used to detect the target angle. First the correlation matrix is estimated for a given training region, and then the weight vectors are calculated using different presumed desired signal angles. For this data set, the target is at  $245^\circ$ . In Figure 6.22, the training is done using all 300 range cells. The non-adaptive beamformer fails, due to a large sidelobe, and points in the direction of the interference. Both SMI and the eigencanceler detect the right angle for the target. When the training is lowered to 50 cells, see Figure 6.23, the sidelobes of the SMI are increased. The performance of the eigencanceler is almost unchanged. In Figure 6.24, the training support is lowered to 28 cells. The performance of SMI is degraded considerably and the eigencanceler's performance is superior. Even with the target included in the training set, the eigencanceler manages to detect the target, even though it is only a few dB above the interference. The sidelobes of the eigencanceler are much lower than the sidelobes of the SMI.

#### 6.5.5 Signal Cancellation

In this section, signal cancellation due to the high desired signal component of the estimated correlation matrix is studied. In Figure 6.25(a), the target range cell output relative to sky noise, as a function of the number of training points, is plotted. The target region is

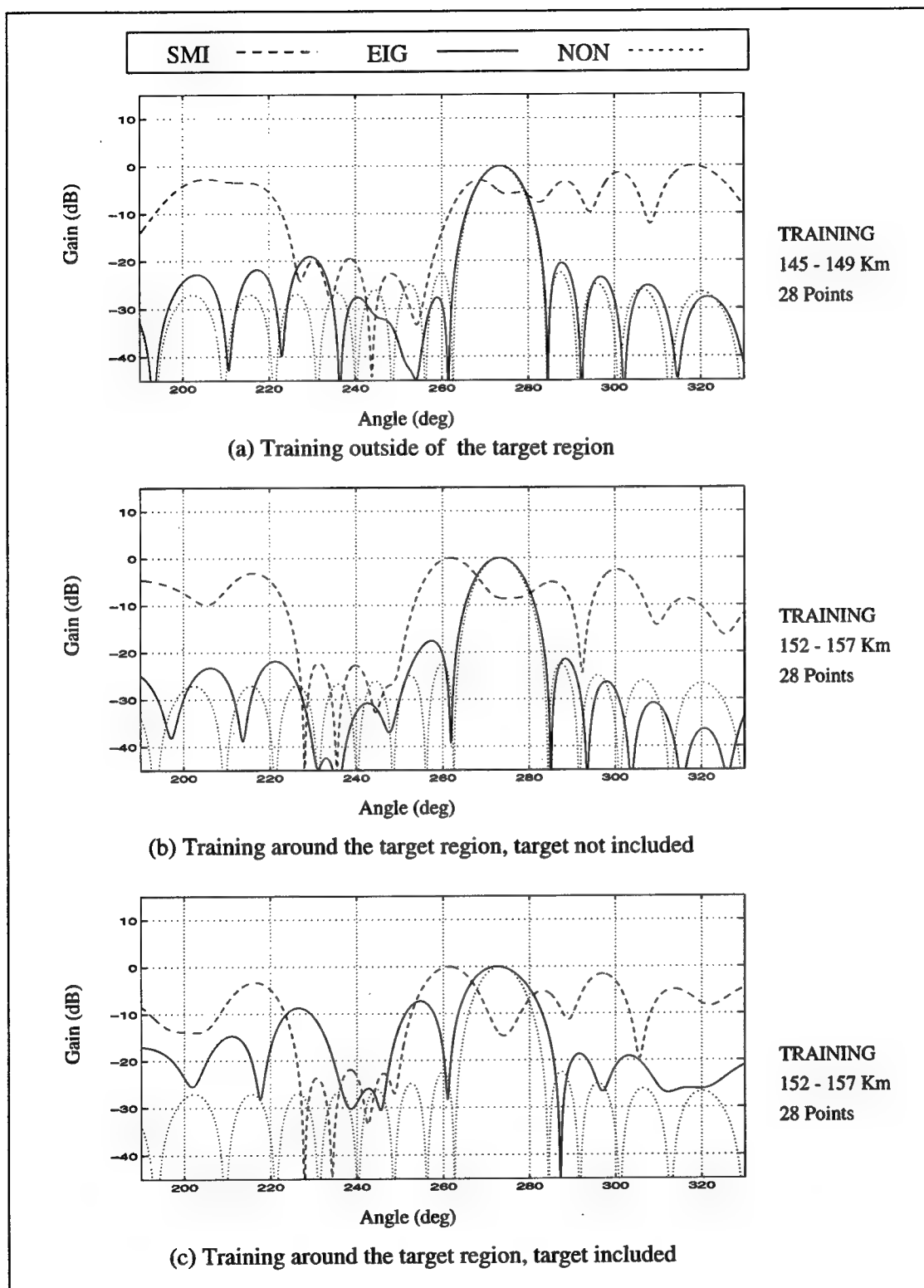


**Figure 6.21** Post-Doppler Antenna Pattern Plots Using 28 Training Points

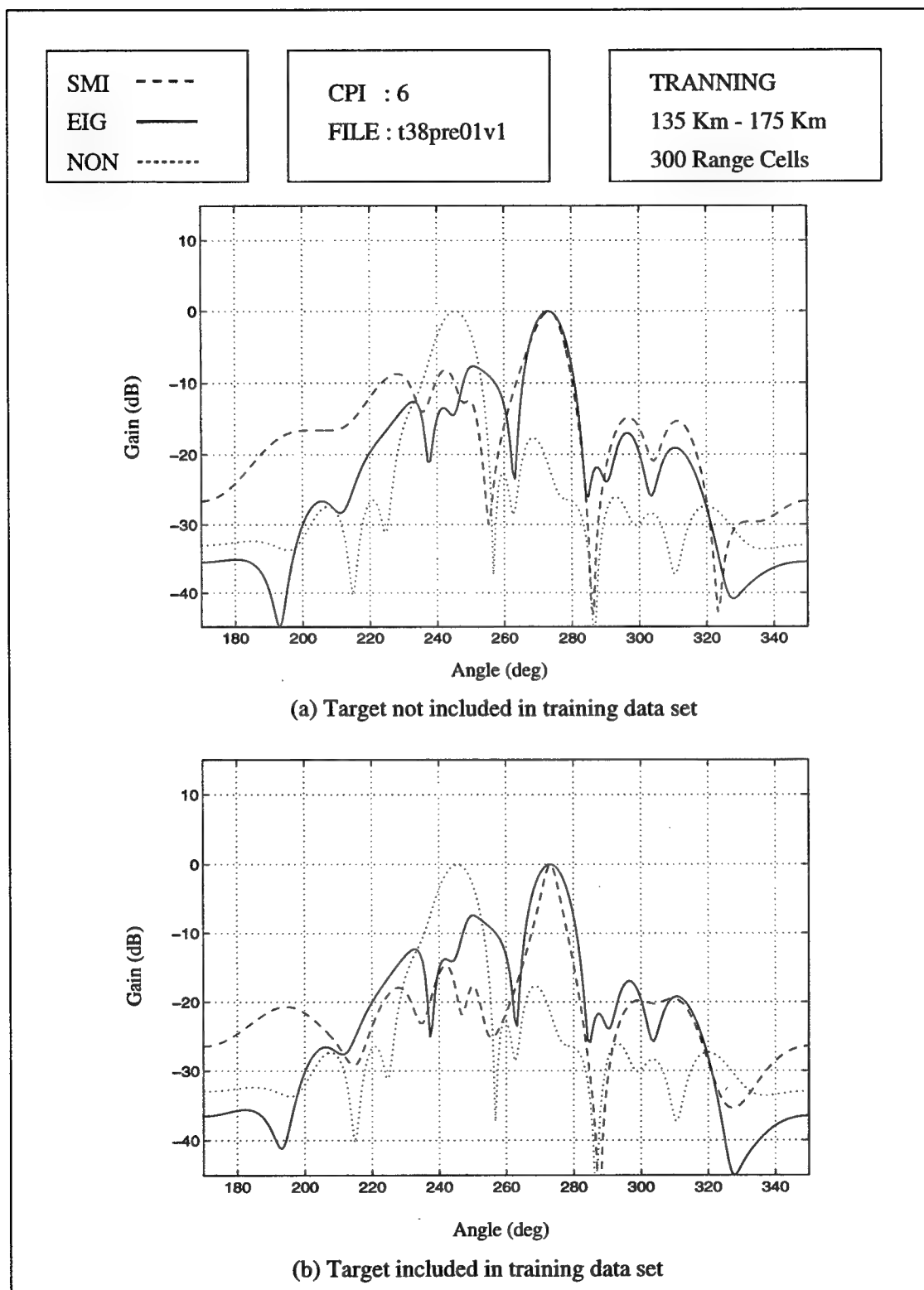


**Figure 6.22** Post-Doppler Target Detection Using 300 Training Points

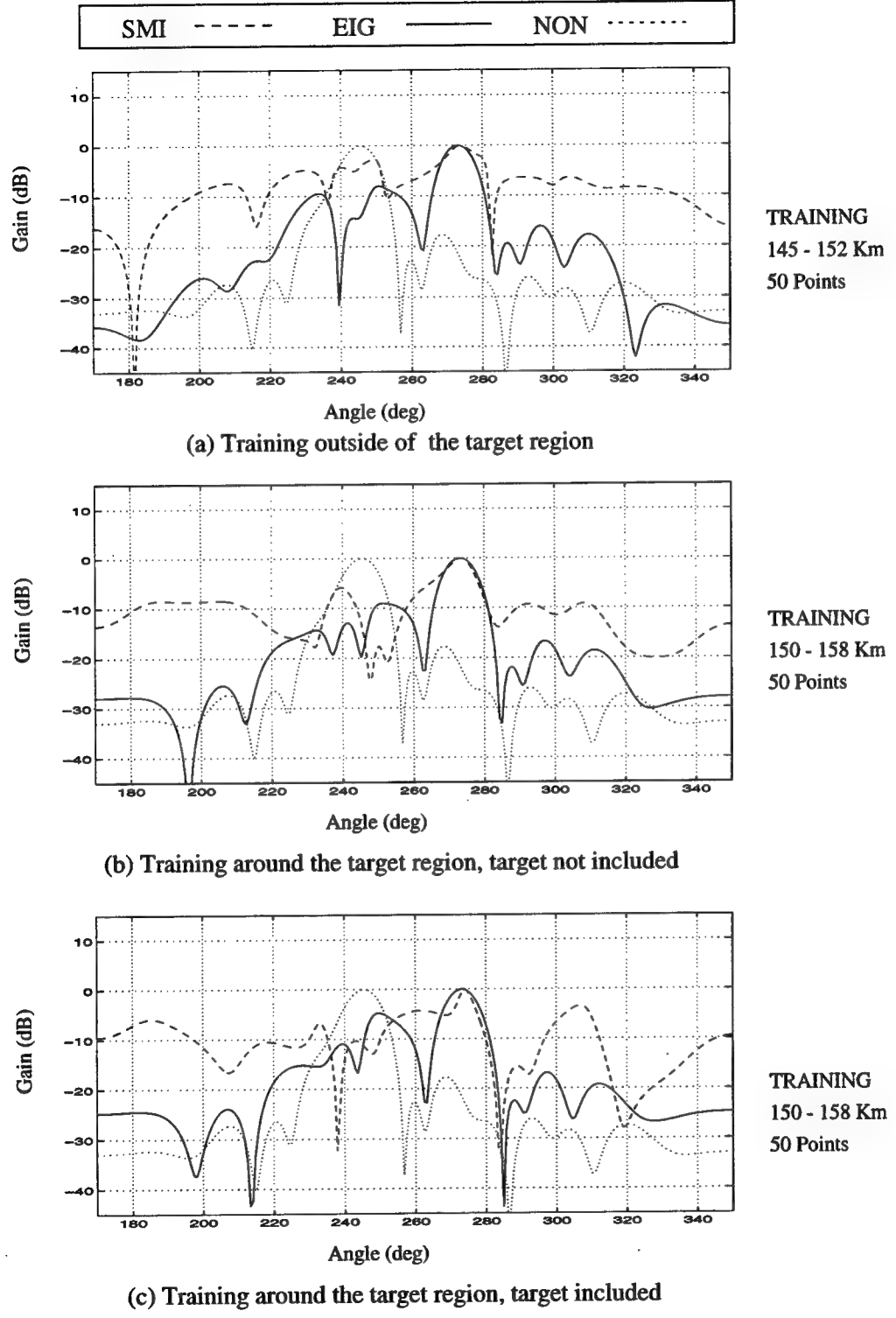


**Figure 6.23** Post-Doppler Target Detection Using 50 Training Points

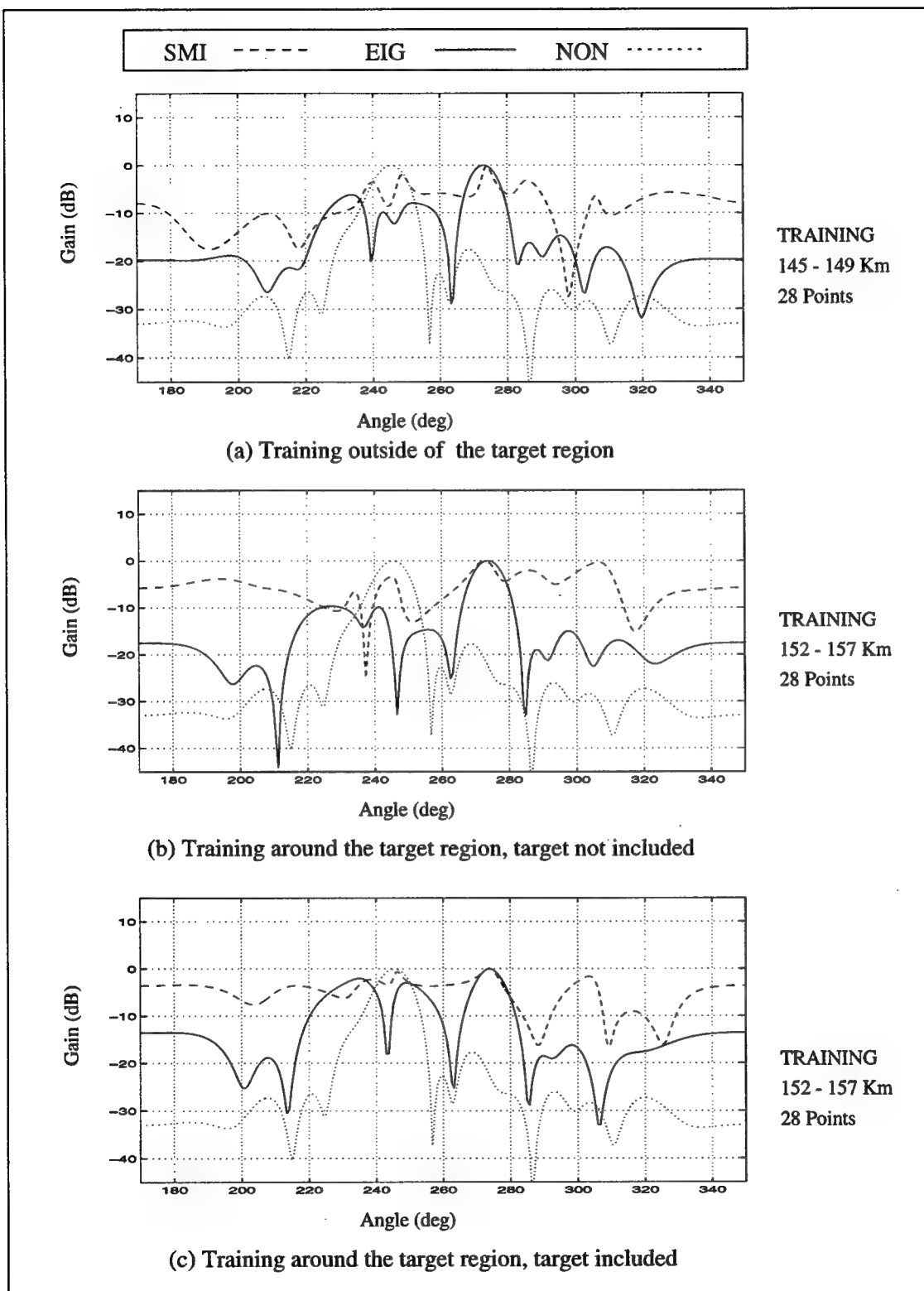


**Figure 6.24** Post-Doppler Target Detection Using 28 Training Points

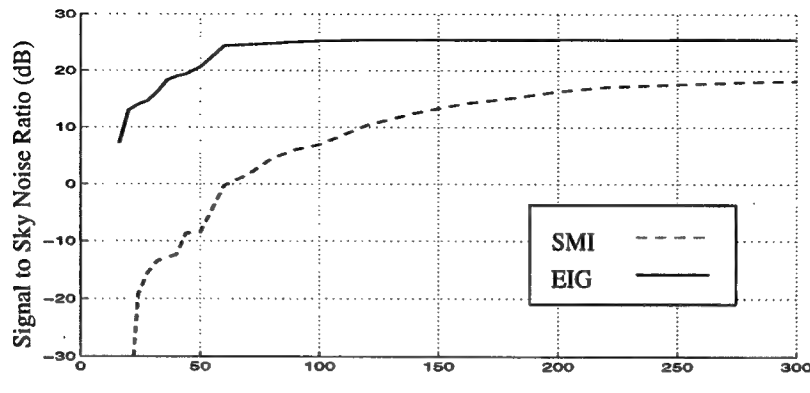
included in the training set, therefore, when the training support is decreased the desired signal component increases. The eigencanceler performs 4 dB better than SMI when the training set is large. When the training set is decreased, the performance of the SMI is affected more than the eigencanceler's performance is. This plot only provides information about how much the desired signal is preserved, but it does not give any information about how much the interference is cancelled. To study clutter cancelation, the output at the target range is plotted with respect to the background noise at the beamformer's output around the target region. The background noise level is calculated by taking the mean of the beamformer's output from 142 km to 165 km, over 150 points. The target region is not included in the calculations of the mean. Comparing part (a) to part (b), the performance of SMI approaches that of the eigencanceler. This shows that SMI cancels the interference better than the eigencanceler, but the performance is still inferior because of the signal cancellation effect. In Figure 6.25(c), instead of using a fixed region for calculation of the mean as in part (b), the background noise power is calculated using exactly the same region as the training. The performance of the SMI is improved even more because SMI cancels interference in the training region more effectively, but it performs poorly cancelling the interference outside the training region. This was also observed in the range detection plots where a null was placed around the training region, as in Figure 6.16(b). In conclusion, SMI cancels the desired signal as the number of training points is decreased.

The eigencanceler's is a better estimator of global interference than SMI, even with a localized correlation matrix. The eigencanceler uses the eigenvectors that correspond to the largest eigenvalues, which is a better representation of the global interference. On the other hand, SMI uses the inverse of the correlation matrix, which involves all the eigenvectors. This is a much better estimate locally, but it is not very effective globally.

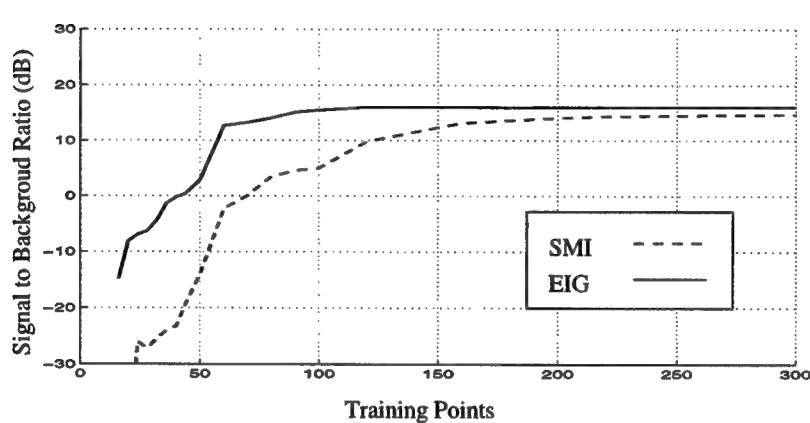
## 6.6 Discussion

In this chapter, the signal cancelation effects were studied when there is a mismatch between the true desired signal and the presumed theoretical desired signal. Adaptive radar is susceptible to signal cancelation effects when the target signal is included in the training data and in the presence of pointing/calibration errors. It was shown, by analysis and illustrations from the Mountaintop dataset, that the SMI method is very sensitive to the presence of the desired signal component in the estimated correlation matrix, and performance is degraded even with small pointing/calibration errors. The eigenanalysis-based adaptive radar is proven to be much more robust than the SMI method with respect to signal cancellation effects.

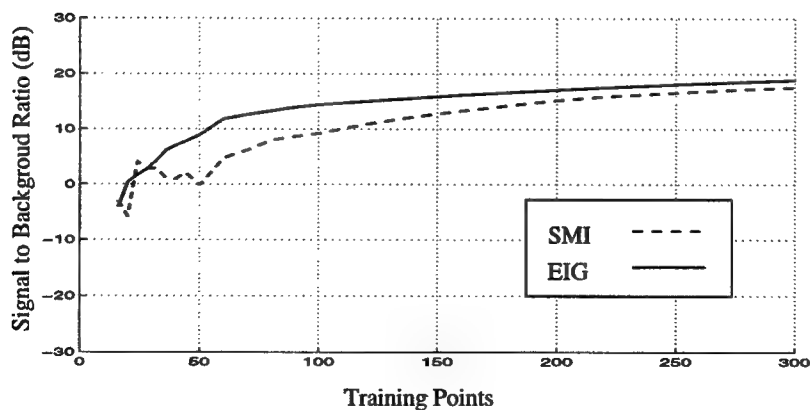
The design of calibration filters to minimize the mismatch was explained and the results of the calibration filters were illustrated on the experimental data. Also the pulse compression method to achieve high resolution was explained.



(a) Relative to sky noise



(b) Relative to background noise, 142 km to 165 km



(b) Relative to background noise, training region

**Figure 6.25** Signal Cancellation

## CHAPTER 7

### PERFORMANCE COMPARISON OF REDUCED RANK STAP TECHNIQUES

Recent publications have shown the advantages of various forms of reduced-rank methods over the full-rank SMI method [22, 1, 62]. The sample support required by reduced-rank processing is only  $K \approx 2r$ , where  $r$  is the rank of the interference to be rejected. Equivalently, for  $r \ll N$  and for the *same* sample support, the SNR loss associated with reduced-rank methods is smaller than for the SMI.

In this chapter we review and compare several reduced-rank methods. First, we first formulate the reduced-rank minimum variance beamformer (RR-MVB), which utilizes the principal components of a specified matrix transformation. RR-MVB is equivalent to the reduced-rank generalized sidelobe canceler (GSC). Another class of reduced-rank methods are based on the cross-spectral metric (CSM) [63, 64]. Those are also presented in the GSC context. The last of the reduced-rank methods reviewed is the eigencanceler [1]. It is interesting to note that reduced-rank methods are generally evaluated by the error they produce with respect to full-rank adaptive processing. When the true covariance matrix is known, reduced-rank methods are suboptimal to the Wiener solution. However, our interest in those methods arises since it has been shown that when the interference is contained within a subspace of the signal space, and the interference+noise covariance matrix is estimated from a dataset with limited support, reduced-rank methods actually *outperform* full-rank adaptive processing. This is explained by the presence, in addition to thermal noise effects, of errors resulting from the estimation process. Reduced-rank processing suppresses estimation errors at the cost of a bias in the SNR. The net effect, however, is a significant performance improvement for cases when the interference may be modeled as low-rank. Reduced-rank methods are clearly important for STAP radar, where a large number of degrees of freedom may be available. For a uniform array and for fixed PRF, the space-time clutter covariance matrix is essentially low-rank due to the inherent oversampling nature of the STAP architecture. Hence, the space-time radar problem is well suited to the application of techniques that take advantage of the low-rank property.

#### 7.1 Reduced Rank Processing with Known Covariance

A diagram of the reduced-rank MVB is shown in Figure 7.1.

The full-rank MVB weight vector is obtained as a solution to the optimization problem:

$$\min \mathbf{w}^H \mathbf{R} \mathbf{w} \quad \text{subject to} \quad \mathbf{s}^H \mathbf{w} = 1, \quad (7.1)$$

where  $\mathbf{R} = E [\mathbf{x}_k \mathbf{x}_k^H]$ ,  $\mathbf{x}_k$  are snapshots of the secondary data, and  $\mathbf{s}$  is the steering vector. With RR-MVB, the vector  $\mathbf{x}_k$  is pre-processed by a full column rank  $N \times r$  matrix transformation  $\mathbf{T}$ . The RR data is then the  $r \times 1$  vector  $\mathbf{z}_k = \mathbf{T}^H \mathbf{x}_k$ , the RR covariance matrix is  $\mathbf{T}^H \mathbf{R} \mathbf{T}$ , and the RR steering vector is  $\mathbf{t} = \mathbf{T}^H \mathbf{s}$ . The RR-MVB weight vector is the solution to

$$\min \mathbf{w}^H (\mathbf{T}^H \mathbf{R} \mathbf{T}) \mathbf{w} \quad \text{subject to} \quad (\mathbf{T}^H \mathbf{s})^H \mathbf{w} = 1, \quad (7.2)$$

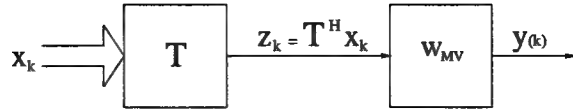


**Figure 7.1** Reduced-rank MVB.

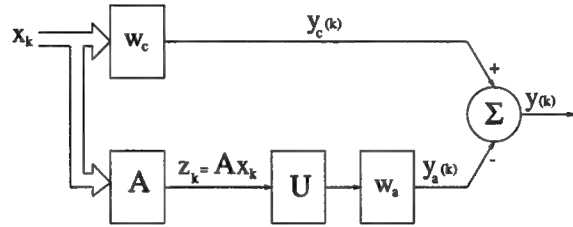


**Figure 7.2** Reduced-rank GSC.

and is given by the  $r \times 1$  weight vector

$$\mathbf{w} = k \left( \mathbf{T}^H \mathbf{R} \mathbf{T} \right)^{-1} \mathbf{T}^H \mathbf{s}, \quad (7.3)$$

where  $k = \left( \mathbf{s}^H \mathbf{T} \left( \mathbf{T}^H \mathbf{R} \mathbf{T} \right)^{-1} \mathbf{T}^H \mathbf{s} \right)^{-1}$ . Based on this weight vector, it is easy to show that the optimal SNR,  $\mu$ , is given by

$$\mu = \mathbf{s}^H \mathbf{T} \left( \mathbf{T}^H \mathbf{R} \mathbf{T} \right)^{-1} \mathbf{T}^H \mathbf{s}, \quad (7.4)$$

where to simplify notation, it is assumed that the target power  $\sigma_s^2 = 1$ .

The reduced-rank GSC is shown in Figure 7.2. From the figure it is observed that the output can be expressed

$$y = y_c(k) - y_a(k) = \mathbf{w}_c^H \mathbf{x}_k - \mathbf{w}_a^H \mathbf{U}^H \mathbf{A} \mathbf{x}_k, \quad (7.5)$$

where  $\mathbf{w}_c$ , the weight vector of the nonadaptive portion, is just the steering vector  $\mathbf{w}_c = \mathbf{s}$ ,  $\mathbf{w}_a$  is the adaptive weight, the matrix  $\mathbf{U}$  is a full column rank transformation, and  $\mathbf{A}$  is set such the MVB and GSC methods are equivalent. The weight vector  $\mathbf{w}_a$  is found as the solution to the unconstrained optimization problem

$$\min_{\mathbf{w}_a} \left( \mathbf{s} - \mathbf{A}^H \mathbf{U} \mathbf{w}_a \right)^H \mathbf{R} \left( \mathbf{s} - \mathbf{A}^H \mathbf{U} \mathbf{w}_a \right). \quad (7.6)$$

The overall GSC weight vector is then given by

$$\mathbf{w} = \left( \mathbf{I}_N - \mathbf{A}^H \mathbf{U} \left( \mathbf{U}^H \mathbf{A} \mathbf{R} \mathbf{A}^H \mathbf{U} \right)^{-1} \mathbf{U}^H \mathbf{A} \mathbf{R} \right) \mathbf{s}, \quad (7.7)$$

where  $\mathbf{I}_N$  is the  $N$ -dimensional identity matrix. In [65] it is shown that for the MVB and GSC methods to be equivalent, the following conditions need to be met: (i)the matrix  $\mathbf{A}$

must block the look direction,  $\mathbf{As} = \mathbf{0}$ , (ii)  $\mathbf{s}^H \mathbf{s} = 1$ . Assuming that  $\mathbf{A}$  has full column rank, and that  $\mathbf{s}$  is the only vector in the null space of  $\mathbf{A}$ , the dimensions of  $\mathbf{A}$  are  $(N - 1) \times N$ . Consequently, the rank reducing matrix  $\mathbf{U}$  is  $(N - 1) \times r$ . Multiple linear constraints can be incorporated in  $\mathbf{A}$  resulting in a null space of dimension equal to the number of constraints. The output SNR (when target power  $\sigma_s^2 = 1$ ) is given by

$$\mu = \left( \mathbf{s}^H \mathbf{Rs} - \mathbf{s}^H \mathbf{RA}^H \mathbf{U} \left( \mathbf{U}^H \mathbf{ARA}^H \mathbf{U} \right)^{-1} \mathbf{U}^H \mathbf{ARs} \right)^{-1} \quad (7.8)$$

Various choices of the rank reducing transformation  $\mathbf{U}$  are now considered:

1. The goal is to maximize  $\mu$ . In turn, this is achieved by maximizing the term  $\eta = \mathbf{s}^H \mathbf{RA}^H \mathbf{U} \left( \mathbf{U}^H \mathbf{ARA}^H \mathbf{U} \right)^{-1} \mathbf{U}^H \mathbf{ARs}$ . For a given reduced rank  $r$ ,  $\eta$  is optimized by a transformation  $\mathbf{U}$  that meets the relation

$$\mathbf{A}^H \mathbf{U} = \mathbf{Q}_1, \quad (7.9)$$

where  $\mathbf{Q}_1$  consists of the  $r$  principal eigenvectors of  $\mathbf{R}$ . Assuming that the  $(N - 1) \times N$  signal blocking matrix  $\mathbf{A}$  has full column rank, the elements of  $\mathbf{U}$  can be obtained from the solution of a least-squares problem. It is easy to show that with this choice of  $\mathbf{U}$ :

$$\begin{aligned} \mu &= \left( \mathbf{s}^H \mathbf{Rs} - \mathbf{s}^H \mathbf{Q}_1 \Lambda_1 \mathbf{Q}_1^H \mathbf{s} \right)^{-1} \\ &= \mathbf{s}^H \mathbf{Q}_2 \Lambda_2^{-1} \mathbf{Q}_2^H \mathbf{s}. \end{aligned} \quad (7.10)$$

2. To avoid the complication of a least-squares problem, let the matrix  $\mathbf{U}$  be restricted to consist of  $r$  of the  $(N - 1)$  eigenvectors of  $\mathbf{R}_a = \mathbf{ARA}$ , where  $\mathbf{R}_a = \overline{\mathbf{Q}}_1 \overline{\Lambda}_1 \overline{\mathbf{Q}}_1^H + \overline{\mathbf{Q}}_2 \overline{\Lambda}_2 \overline{\mathbf{Q}}_2^H$ , and  $\text{rank}(\overline{\mathbf{Q}}_1) = r$ . A natural choice would be to let the rank reducing transformation consist of the  $r$  principal eigenvectors of  $\mathbf{R}_a$ , i.e.,  $\mathbf{U} = \overline{\mathbf{Q}}_1$ . A less intuitive, but optimal approach is suggested in [63, 64]: construct  $\mathbf{U}$  from the  $r$  eigenvectors of  $\mathbf{R}_a$  that maximize the quantity

$$\frac{\left| \overline{\mathbf{q}}_i^H \mathbf{ARs} \right|^2}{\lambda_i}, \quad (7.11)$$

where  $\overline{\mathbf{q}}_i$ ,  $\lambda_i$  are respectively eigenvectors and eigenvalues of  $\mathbf{R}_a$ . In the references, this method is referred as the *cross-spectral metric* (CSM) method.

3. Principal components decomposition, such as considered above, is data dependent. Fixed, reduced-rank transformations can be constructed by selecting the principal components of the discrete Fourier transform (DFT) or the discrete cosine transform (DCT). The cross spectral metric can also be used in conjunction with these fixed transforms [63, 64].

Rank-reducing transformations are now evaluated in the MVB framework. Consider the SNR at the MVB output, as given by (7.4). When the transformation  $\mathbf{T}$  is unitary, it has no effect on the output SNR, and  $\mu = \mathbf{s}^H \mathbf{R}^{-1} \mathbf{s} = \mu_{\max}$ . For any  $N \times r$  rank reducing transformation  $\mathbf{T}$ ,  $r < N$ ,  $\mu = \mathbf{s}^H \mathbf{T} \left( \mathbf{T}^H \mathbf{RT} \right)^{-1} \mathbf{T}^H \mathbf{s} < \mu_{\max}$ . Specific examples are considered below.

1. Consider how *Case 1* of the GSC translates to the MVB framework. By substituting (7.9) in (7.7), we obtain the equivalent MVB weight vector

$$\mathbf{w} = (\mathbf{I}_N - \mathbf{Q}_1 \mathbf{Q}_1^H) \mathbf{s}. \quad (7.12)$$

This relation establishes the equivalence between the reduced-rank GSC and the eigencanceler [1]. The eigencanceler is a method that produces the minimum norm weight vector meeting the set of linear constraints, and subject to the additional constraint of orthogonality to the interference subspace (formed by the principal eigenvectors of the space-time covariance matrix). Since  $\mathbf{Q}_2 \mathbf{Q}_2^H = \mathbf{I}_N - \mathbf{Q}_1 \mathbf{Q}_1^H$ , the eigencanceler is equivalent to the application of a rank reducing transformation  $\mathbf{T} = \mathbf{Q}_2$ , where the columns of  $\mathbf{Q}_2$  span the noise subspace of the covariance  $\mathbf{R}$ . Indeed, (7.12) is obtained by using  $\mathbf{T} = \mathbf{Q}_2$  and (4.1) in (7.3). The eigencanceler requires that the partition of eigenvectors into  $\mathbf{Q}_1$  and  $\mathbf{Q}_2$  be such that the desired signal lies mostly in the noise subspace (this is indeed the case when  $\mathbf{R}$  is estimated from the secondary data). The output SNR is given by

$$\begin{aligned} \mu &= \mathbf{s}^H \mathbf{Q}_2 \left( \mathbf{Q}_2^H \mathbf{R} \mathbf{Q}_2 \right)^{-1} \mathbf{Q}_2^H \mathbf{s} \\ &= \mathbf{s}^H \mathbf{Q}_2 \Lambda_2^{-1} \mathbf{Q}_2^H \mathbf{s} \\ &< \mu_{\max}, \end{aligned} \quad (7.13)$$

where

$$\mu_{\max} = \mathbf{s}^H \mathbf{Q}_1 \Lambda_1^{-1} \mathbf{Q}_1^H \mathbf{s} + \mathbf{s}^H \mathbf{Q}_2 \Lambda_2^{-1} \mathbf{Q}_2^H \mathbf{s}. \quad (7.14)$$

2. The  $N \times (r+1)$  matrix is given by  $\mathbf{T} = [\mathbf{Q}_1, \mathbf{q}_{r+1}]$ , i.e., it consists of the  $r$  principal components of the signal-plus-interference subspace, augmented with one of the eigenvectors of the noise subspace [62]. In this case  $\mathbf{T}$  consists of the principal components of the Karhunen-Loeve transform. The output SNR is given by  $\mu = \mathbf{s}^H \mathbf{Q}_1 \Lambda_1^{-1} \mathbf{Q}_1^H \mathbf{s} + \mathbf{s}^H \mathbf{q}_{r+1} \lambda_{r+1}^{-1} \mathbf{q}_{r+1}^H \mathbf{s}$ . Note that if the look direction is in the noise subspace of the transform  $\mathbf{T}$ , i.e.,  $\mathbf{T}^H \mathbf{s} = \mathbf{0}$ , there is no solution that meets the linear constraint in (7.2). This problem is circumvented in [66] by the augmentation of  $\mathbf{T}$  with the vector  $\mathbf{s}$ ,  $[\mathbf{T}, \mathbf{s}] \rightarrow \mathbf{T}$ .
3. Similar to *Case 3* of the GSC, the rank reducing transformation  $\mathbf{T}$  may be constructed from the principal components of a fixed transform such as the DFT or the DCT.
4. The columns of  $\mathbf{T}$  may be designed using the cross-spectral metric approach.

In conclusion of this section, when the covariance matrix  $\mathbf{R}$  is known, a rank reducing transformation induces a loss in the SNR. In the next section, this loss will be incorporated in the performance evaluation of the case when the covariance is not known and is evaluated from the data.

## 7.2 Reduced Rank Processing with Unknown Covariance

In practice, the space-time covariance matrix is not known and it needs to be estimated from the secondary data, as explained in the previous chapters. This is the application for which reduced rank methods are advantageous due to their improved statistical stability. Let the number of snapshots from the secondary dataset be equal to  $K$ . Then the estimated covariance matrix is given by  $\widehat{\mathbf{R}} = \frac{1}{K} \sum_{k=1}^K \mathbf{x}_k \mathbf{x}_k^H$ . In this section, the performance of reduced-rank processors is analyzed as a function of the sample support  $K$ .

With SMI, the full-rank MVB weight vector is given by  $\mathbf{w} = \widehat{\mathbf{R}}^{-1}\mathbf{s}$ . The CSNR can be expressed as

$$\rho = \frac{(\mathbf{s}^H \widehat{\mathbf{R}}^{-1} \mathbf{s})^2}{\mathbf{s}^H \widehat{\mathbf{R}}^{-1} \mathbf{R} \widehat{\mathbf{R}}^{-1} \mathbf{s}} \frac{1}{\mathbf{s}^H \mathbf{R}^{-1} \mathbf{s}}. \quad (7.15)$$

The density of the conditioned SNR for the SMI method with Gaussian data has been characterized in [10], and is given by the beta distribution with parameters  $K$  and  $N$ ,

$$f(\rho) = B(N) = C (1 - \rho)^{N-2} \rho^{K+1-N}, \quad (7.16)$$

where  $C = \Gamma(K+1) / (\Gamma(N-1)\Gamma(K+2-N))$ , and  $\Gamma(K+1) = K!$  is the standard gamma function. The notation  $B(N)$  emphasizes the signal space parameter  $N$  of the beta distribution shown above. When a reduced-rank transformation  $\mathbf{T}$  is applied to the data, the CSNR can be written:

$$\rho = \frac{(\mathbf{t}^H \widehat{\Sigma}^{-1} \mathbf{t})^2}{\mathbf{t}^H \widehat{\Sigma}^{-1} \Sigma \widehat{\Sigma}^{-1} \mathbf{t}} \frac{1}{\mathbf{s}^H \mathbf{R}^{-1} \mathbf{s}}, \quad (7.17)$$

where  $\mathbf{t} = \mathbf{T}^H \mathbf{s}$  is an  $r \times 1$  vector, and  $\Sigma = \mathbf{T}^H \mathbf{R} \mathbf{T}$ ,  $\widehat{\Sigma} = \mathbf{T}^H \widehat{\mathbf{R}} \mathbf{T}$  are  $r \times r$  matrices. Of interest is to determine the distribution of  $\rho$  for various reduced-rank methods. It is important to distinguish between two cases: (1) the transformation  $\mathbf{T}$  is fixed, (2) the transformation  $\mathbf{T}$  is data dependent. The former case applies when  $\mathbf{T}$  is formed from the DFT or the DCT. The transformation  $\mathbf{T}$  is also fixed when it is formed by eigenvectors of the true covariance  $\mathbf{R}$ , but this case is of no great practical value as the assumption here is that  $\mathbf{R}$  is not known. Rather,  $\mathbf{T}$  is formed from the eigenvectors of the estimated covariance  $\widehat{\mathbf{R}}$  and, as such, is data dependent.

When  $\mathbf{T}$  is fixed, (7.17) can be rewritten as follows:

$$\rho = \rho_r \rho_b, \quad (7.18)$$

where  $\rho_r$  is the reduced-rank CSNR,

$$\rho_r = \frac{(\mathbf{t}^H \widehat{\Sigma}^{-1} \mathbf{t})^2}{\mathbf{t}^H \widehat{\Sigma}^{-1} \Sigma \widehat{\Sigma}^{-1} \mathbf{t}} \frac{1}{\mathbf{t}^H \Sigma^{-1} \mathbf{t}} = B(r), \quad (7.19)$$

and  $\rho_b$  is the bias in the optimal SNR introduced by the transformation  $\mathbf{T}$ ,

$$\rho_b = \frac{\mathbf{t}^H \Sigma^{-1} \mathbf{t}}{\mathbf{s}^H \mathbf{R}^{-1} \mathbf{s}}. \quad (7.20)$$

Equations (7.18)-(7.20) clearly demonstrate the effect of reduced rank transformation on the SMI-MVB method. The linear transformation  $\mathbf{T}$  preserves the Gaussian distribution of the

data, hence the reduced-rank CSNR,  $\rho_r$ , has a beta distribution  $B(r)$  with parameters  $K$  and  $r$ . Improved statistical stability is evident in the higher CSNR values associated with  $\rho_r$ . For example, for the full-rank SMI,  $E[\rho] = 0.5$  for  $K = 2N - 3$  [10], while for the reduced-rank SMI,  $E[\rho_r] = 0.5$  for  $K = 2r - 3$ , i.e., fewer samples are required for the same performance level. The higher CSNR values due to improved statistical stability, are somewhat offset by the bias  $\rho_b$ , which is the loss in the optimal SNR due to the rank reduction. This loss is the quantity  $\mu/\mu_{\max}$  analyzed in the previous section. The performance of the GSC processor with a fixed rank-reducing transformation is analyzed in [67].

The case when  $\mathbf{T}$  is data dependent cannot be directly derived from the SMI distribution. The asymptotic density of the conditioned SNR for the eigencanceler ( $\mathbf{T}$  consists of the noise eigenvectors of the estimated covariance) is derived in [1].

### 7.3 Numerical Results

In this section are provided numerical results for several of the reduced-rank methods presented in previous sections. The simulation model used an  $N_s = 8$  element array with  $N_t = 4$  taps at each element. The clutter was located in the angular sector of 0 to 30 degrees. The steering vector was set at 50 degrees, and at a normalized Doppler frequency of 0.4. The total input clutter-to-noise ratio (CNR) of the distributed clutter was 10 dB. In Figure 7.3, the distribution of  $\rho$  based on 20,000 runs is shown for several reduced-rank methods, as well as for full-rank SMI. The reduced-rank methods were: eigencanceler, DCT, DFT, and CSM based on the eigen-decomposition and implemented as a GSC. The number of principal components used to generate the results shown in the figure was  $r = 4$  for all methods. The CSM and eigencanceler methods are shown to produce the highest CSNR's, with reduced-rank MVB based on the DCT and DFT providing slightly lower performance. All reduced-rank methods clearly outperform the full-rank SMI. Figure 7.4 plots the average probability of detection based on 200 runs and a false alarm probability of  $10^{-5}$ . The figure illustrates the same trend as Figure 7.3; best detection performance is provided by the eigencanceler and CSM, followed by DCT and DFT (indistinguishable), and by the full-rank SMI. The effect of the rank order on the performance is illustrated in Figure 7.5. In the figure, the CSNR is plotted as a function of rank of the rank-reducing transformation. For all methods it seems that  $r = 4$  is the optimal rank order (for the particular scenario considered). CSM provides slightly better performance when the rank is underestimated. The DCT transformation seems to be the least affected by overestimating the rank. Obviously, the rank has no effect on the SMI method. The effect of the CNR on performance is illustrated in Figure 7.6. The CSNR is plotted as a function of the input CNR. The CSNR is computed for a rank-reducing transformation with  $r = 4$ . As the CNR increases, the interference power spills over more than 3-4 principal values. Thus the rank reducing transformations are inadequate in capturing the interference power and performance is degraded.

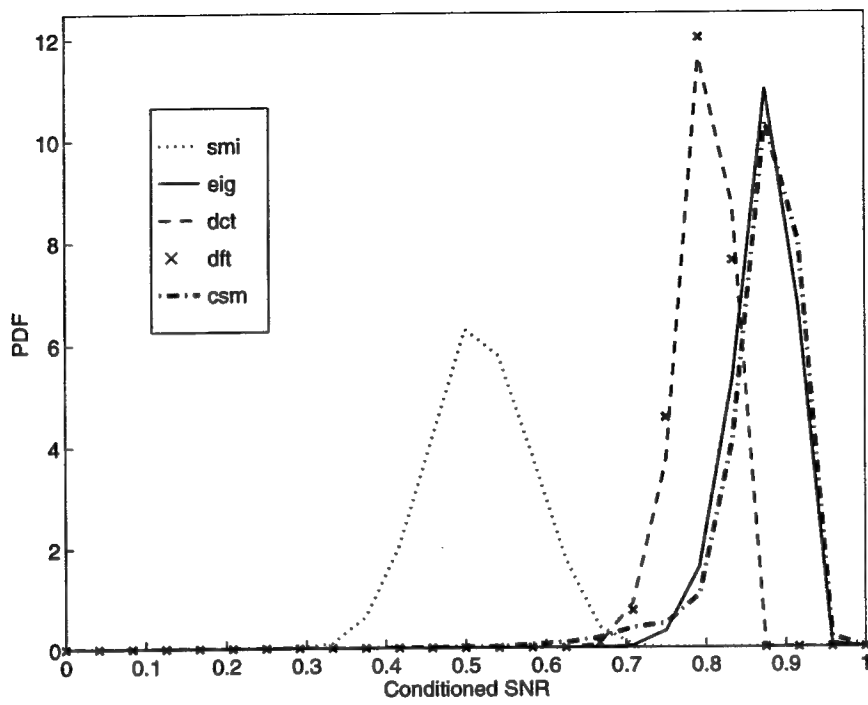


**Figure 7.3** Probability density of the CSNR.

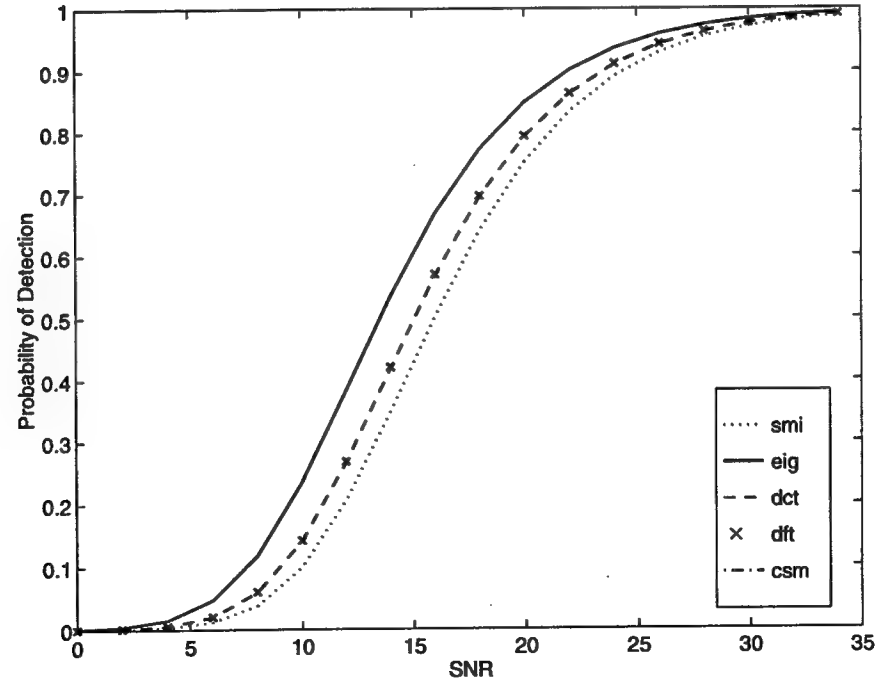


**Figure 7.4** Probability of detection for reduced-rank methods.

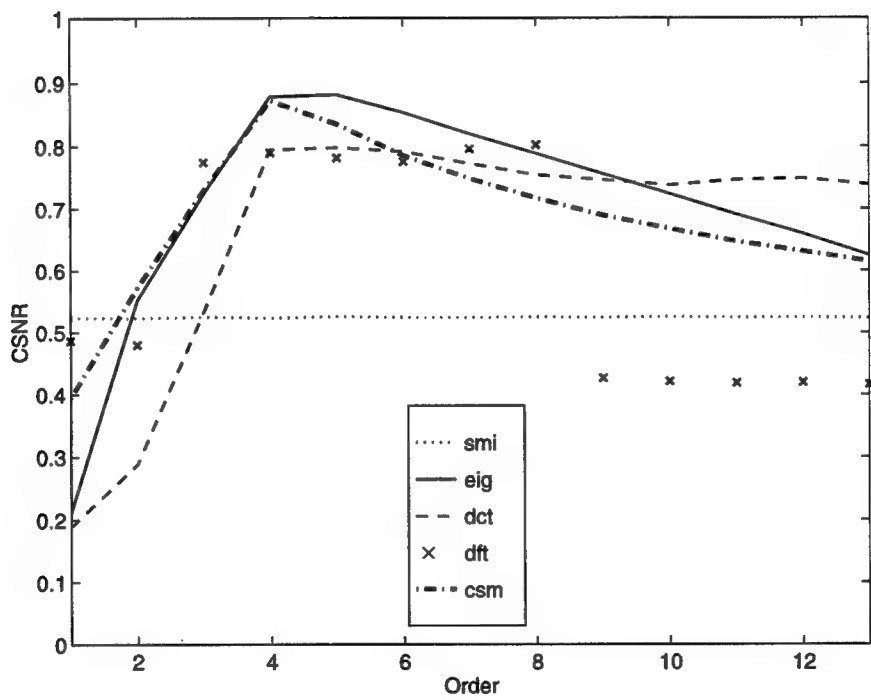


**Figure 7.5 Rank order.**

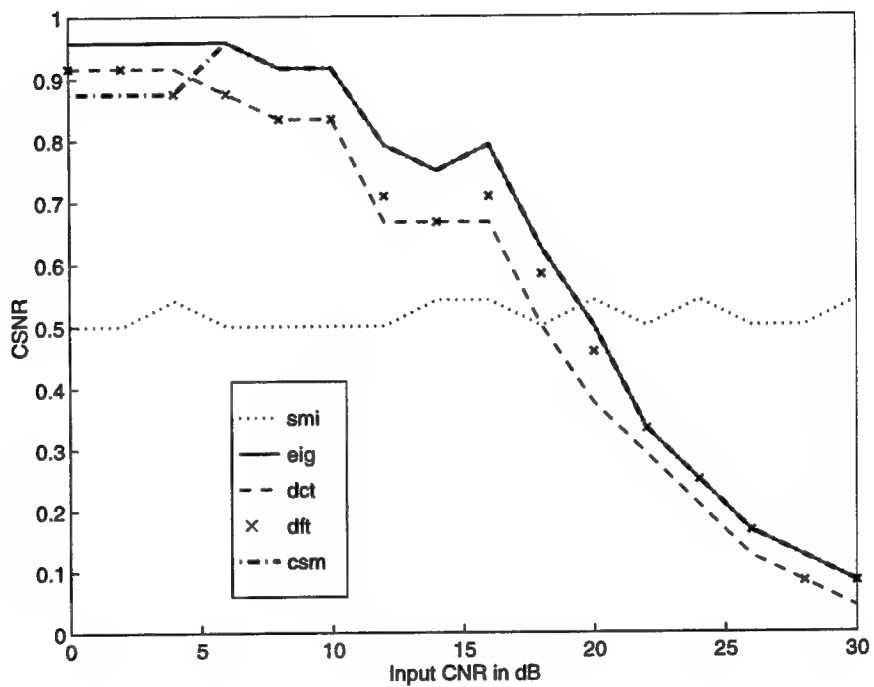


**Figure 7.6** CSNR vs CNR.

## CHAPTER 8

### EIGENCANCELER APPLIED TO HPRF RADAR

In airborne radar, ground clutter returns from all ranges and angles appear to be moving relative to the platform. These mainlobe and sidelobe clutter returns exist in the Doppler region given by  $\pm 2Vf_c/c$  Hz, where  $V$  is the platform velocity,  $f_c$  is the radar's carrier frequency, and  $c$  is the speed of light. The geometry for an airborne radar system is shown in Figure 8.1. A clutter patch seen by the radar at an azimuth angle  $\phi$  and an elevation (depression) angle  $\theta$  has a Doppler frequency  $f_d = (2V/\lambda) \sin \phi \cos \theta$  Hz, where  $\lambda$  is the wavelength corresponding to the transmitted carrier frequency. Radar systems, for missions such as airborne early warning (AEW), may employ high pulse repetition frequency (HPRF) waveforms to enhance long-range detection of high closing-rate targets which appear in the clutter free region of the radar system's Doppler spectrum. However, due to the range-ambiguous nature of the HPRF waveform, strong near-range ground clutter returns received in the antenna sidelobes cannot be simply gated out and are, therefore, folded in with desired signal returns that fall within the Doppler bandwidth of the clutter. This chapter discusses the application of space time adaptive processing (STAP) techniques for clutter suppression in HPRF radar systems.

Space-time processing is a multidimensional filtering approach that mitigates interference in range and Doppler simultaneously. STAP can improve the detection of low velocity targets in mainlobe clutter or small targets in sidelobe clutter. In recent years, STAP has been studied and applied mainly to low PRF (LPRF) radar [9, 61, 68, 69]. The application of STAP to the HPRF radar problem presents a unique set of challenges and differences from the traditional LPRF radar, which are discussed in the chapter.

Three STAP approaches will be investigated. The first is the *pseudoinverse sample matrix inversion* (P-SMI) technique. With traditional SMI, the adaptive weight vector is computed by taking the inverse of the sample covariance matrix. In HPRF radar, the sample support is greatly reduced compared to LPRF due to range ambiguity effects. Hence the pseudoinverse of the covariance matrix is used. The second method investigated is the diagonally loaded SMI [70]. This method is traced back to the early 1980's with publications by Abramovich and Cheremisin [71, 72]. In this technique the singularity of the sample covariance matrix is overcome by diagonal loading. The last STAP technique investigated is the *eigencanceler*[1]. The different STAP techniques are evaluated through a number of performance measures such as output signal to clutter and noise ratio and probability of detection.

#### 8.1 Problem Statement

As a result of the airborne radar platform motion, regions of ground clutter can compete in both range and Doppler with targets of interest. As illustrated in Figure 8.2, regions of competing clutter for LPRF airborne radars are at the intersections of the target range ring and iso-Dopplers ambiguous with the target Doppler. Classical STAP techniques which use range samples on either side of the target to form an estimate of the clutter covariance

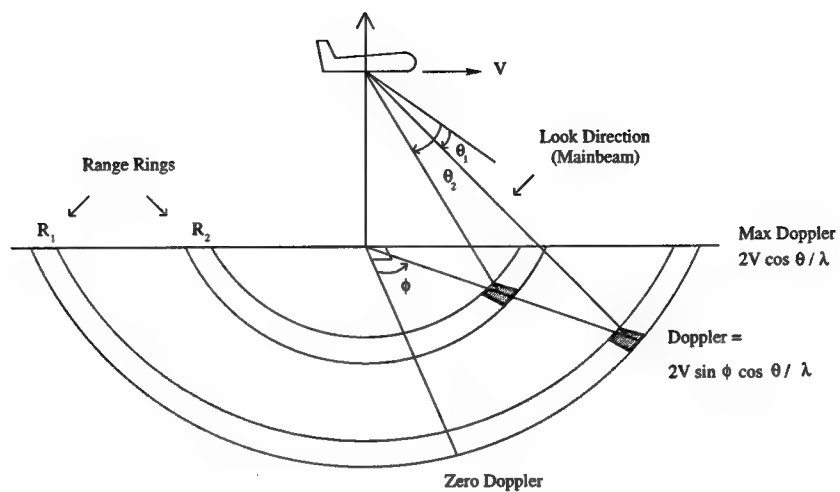


**Figure 8.1** Geometry of the airborne radar problem.

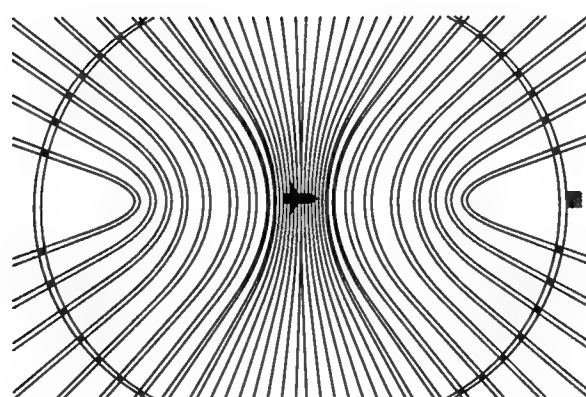


**Figure 8.2** Iso-Doppler, Iso-range ring map for LPRF radar.

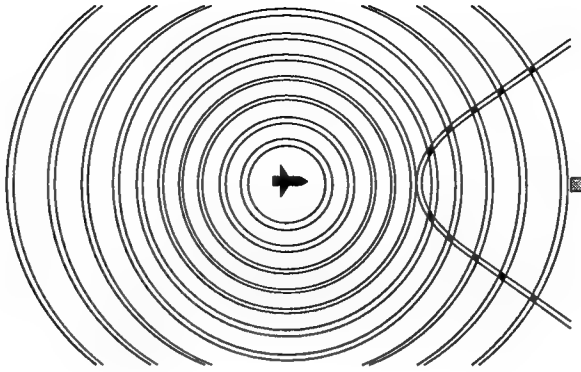


**Figure 8.3** Iso-Doppler, Iso-range ring map for HPRF radar.

matrix have been shown to be effective in suppressing this competing clutter for LPRF radars [9, 69].

Unlike the LPRF problem, for HPRF airborne radars, regions of competing clutter lie along the iso-Doppler contour at points where the ambiguous range is the same as that of a target. This is shown schematically in Figure 8.3. Due to the range-ambiguous nature of the HPRF waveform, each range gate consists of the superposition of the returns from all visible ambiguous ranges. Therefore, regions of strong sidelobe clutter, located at relatively short ranges and steep grazing angles, cannot be gated out and are folded in with mainbeam target returns. Another issue of much importance is sample support. Due to the nature of the HPRF waveform, sample support for estimation of the clutter covariance matrix is limited to the number of range gates available in the radar system. This limited sample support can lead to ill-conditioning of the covariance matrix for classical STAP approaches, such as SMI.

The application of innovative reduced rank STAP solutions, shown to outperform conventional STAP techniques [22, 1, 7], is proposed to address the two problems of range ambiguity and limited sample support associated with HPRF radar systems.

## 8.2 HPRF System's Definitions and Properties

This section presents the system's definitions and requirements for the HPRF radar system discussed in this chapter. Also an explanation of the spectrum of the clutter seen by the airborne radar for such a system is presented.

### 8.2.1 System's Definitions

We use the same signal model presented in chapter 2, however, we define a few extra parameters that are necessary for the discussion of HPRF radar.

The radar's unambiguous range is related to the PRF:

$$R_{\text{un}} = c/(2\text{PRF}). \quad (8.1)$$

If the target's range extends beyond  $R_{\text{un}}$ , the radar cannot measure the true range of the target. Consequently, target returns may be folded over close range clutter echoes. As a consequence of (8.1), radar echoes will have an apparent range,  $R_{\text{app}}$ , and a true range which are related by

$$R_{\text{app}} = R_{\text{true}} - R_{\text{un}}[R_{\text{true}}/R_{\text{un}}], \quad (8.2)$$

where the brackets denote integer part. The data vector  $\mathbf{x}_m$  consists of the sum of contributions of all the range cells folded onto the cell corresponding to index  $m$ . Also, the number of independent data samples equals the number of range cells in an unambiguous range interval. Let  $M$  be the number of range gates spanning the unambiguous range interval of the radar. The maximum likelihood estimate of the space-time covariance matrix is given again by

$$\hat{\mathbf{R}} = \sum_{m=1}^K \mathbf{x}_m \mathbf{x}_m^H. \quad (8.3)$$

The matrix is clearly singular if  $K < N$ . The parameter  $K$  is controlled by the radar's range resolution which is a direct function of the system's bandwidth.

### 8.2.2 Degrees of Freedom

The number of the degrees of freedom that is needed for effective clutter cancelation is determined by the rank of the clutter covariance matrix. In a typical airborne scenario and a calibrated radar, eigen-decomposition, when applied to the covariance matrix, yields a few large eigenvalues while the rest are relatively small. The number of significant eigenvalues or equivalently the rank, can be predicted by the Landau-Pollak relation  $r \cong 2BT + 1$ , where  $B$  is the clutter bandwidth and  $T$  is the time across the filter structure.

The Landau-Pollak relation can be applied to a space-time array as well. The rank of the space-time covariance matrix has been studied in [1, 69]. Here we provide a brief argument for illustrative purposes. For an array with elements at half-wavelength intervals, and a point clutter source at azimuth angle  $\phi$  with respect to the array normal and at elevation angle  $\theta$ , a space-time sample is given by,

$$x_{nk} = e^{j\pi(n-1)\sin\phi\cos\theta} e^{j2\pi(k-1)\nu}, \quad (8.4)$$

where  $\nu$  is the point source Doppler frequency normalized with respect to the PRF. The maximum frequency space-time component is then

$$x_{nk} = e^{j\pi[(N_s-1)+2(N_t-1)\nu_{\max}]}, \quad (8.5)$$

where  $\nu_{\max} = 2V/(\lambda \text{ PRF})$  is the highest normalized Doppler component of the clutter returns. It follows that the number of space-time samples required to represent the clutter contributions is upper bounded

$$r \leq N_s + 2(N_t - 1)\nu_{\max}. \quad (8.6)$$

This is also the highest approximate rank of the clutter plus noise covariance matrix for high clutter-to-noise ratio. In the case of a HPRF radar,  $\nu_{\max} \ll 1$  since the clutter occupies only a fraction of the Doppler spectrum. Thus, the HPRF problem is of lower rank than an equivalent LPRF problem.

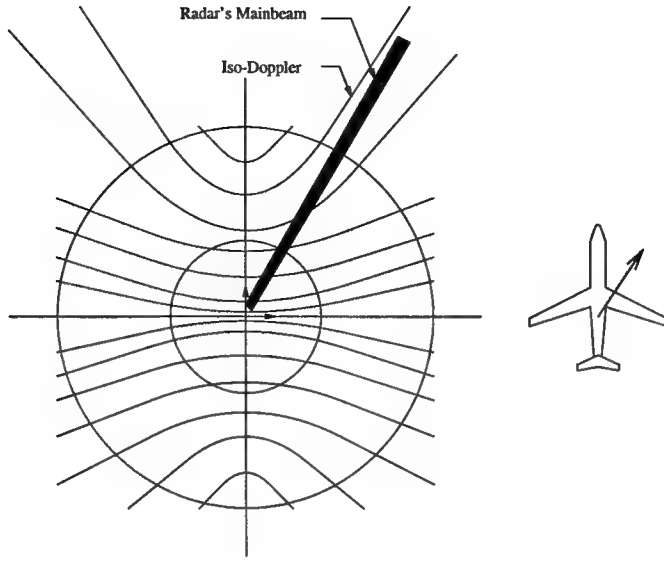


**Figure 8.4** HPRF Clutter Intensity map.

### 8.2.3 ‘J-Hook’ Clutter

In an airborne HPRF application, clutter enters the receiver primarily through the mainbeam and principal elevation sidelobes. This is illustrated in the clutter intensity plot, shown in Figure 8.4. It can be observed that at far ranges clutter returns are approximately parallel to iso-Doppler contours. This implies little variation in the Doppler frequency. The clutter ridge crosses increasingly more iso-Doppler contours as it gets closer to Nadir. This results in the characteristic ‘J-Hook’ curvature of the clutter ridge in the range-Doppler domain. The ‘J-Hook’ is clearly visible on the range-Doppler plot shown in Figure 8.7 in the Numerical Analysis section. As this plot illustrates, for the HPRF waveform, most of the Doppler band is clutter free with mainlobe and sidelobe ground clutter returns located only in the Doppler region given by  $f_d = \pm 2V/\lambda$ .

## 8.3 STAP Techniques

This section describes the various STAP approaches used to combat clutter in HPRF radar.

### 8.3.1 Pseudoinverse SMI

As previously pointed out, the HPRF problem is characterized by low sample support which may often result in an ill-conditioned covariance matrix estimate  $\hat{\mathbf{R}}$  (defined in (8.3)). For such cases, the *pseudoinverse*  $\hat{\mathbf{R}}^\# = (\hat{\mathbf{R}}^H \hat{\mathbf{R}})^{-1} \hat{\mathbf{R}}^H$  is substituted for  $\hat{\mathbf{R}}^{-1}$ . The pseudoinverse SMI (P-SMI) weight vector is then given by

$$\mathbf{w} = \hat{\mathbf{R}}^\# \mathbf{s}. \quad (8.7)$$

### 8.3.2 Diagonally Loaded SMI

The diagonally loaded SMI (L-SMI) is a modification of the traditional SMI method in which a constant is added to the diagonal of the estimated covariance matrix  $\hat{\mathbf{R}}$  in order to improve numerical conditioning. This constant is referred to as the loading factor. In [73] it is suggested to choose a loading factor  $\alpha$  such that  $\sigma^2 < \alpha < \lambda_{\min}$ , where  $\sigma^2$  is the noise power, and  $\lambda_{\min}$  denotes the smallest interference eigenvalue. The L-SMI weight vector is then given by

$$\mathbf{w} = (\hat{\mathbf{R}} + \alpha \mathbf{I})^{-1} \mathbf{s}. \quad (8.8)$$

The loading of the covariance matrix decreases the fluctuations of the small eigenvalues, which are predominantly noise eigenvalues, and as a result decreases fluctuations in  $\mathbf{w}$ .

### 8.3.3 The Eigencanceler

The estimated covariance matrix of the clutter was obtained using (8.3). It has been shown in [1], and as was previously derived in chapter 3, that the eigencanceler's weight vector is given by

$$\mathbf{w} = (\mathbf{I} - \hat{\mathbf{Q}}_1 \hat{\mathbf{Q}}_1^H) \mathbf{s} = \hat{\mathbf{Q}}_2 \hat{\mathbf{Q}}_2^H \mathbf{s} \quad (8.9)$$

where  $\mathbf{I}$ , is the identity matrix.

## 8.4 Numerical Analysis

The simulation model assumed an  $N_s = 8$  elements array with a CPI of length  $N_t = 64$ . The clutter was assumed to come from all elevation angles and was modeled to have a complex-valued Gaussian distribution with zero-mean and variance equal to the clutter-to-noise ratio (CNR). Attenuation due to free-space propagation was assumed proportional to  $R_{\text{true}}^{-3}$ , where  $R_{\text{true}}$  is true range of the cell under test. The CNR was set to 60 dB. The radar parameters were assumed as follows: PRF = 25kHz, platform velocity  $V = 250$  m/s, platform altitude = 30,000 ft, and the transmitted frequency = 3.3 GHz. The target's range was 90 km, its Doppler frequency =  $0.05 \times \text{PRF}$ , and the SNR = 48 dB. The radar's unambiguous range was about 6 km.

Equations (8.7), (8.8), and (8.9) are used to calculate the space-time adaptive filter weights for the P-SMI, L-SMI and eigencanceler, respectively. Figure 8.5 shows the density functions of the conditioned signal-to-noise ratio (CSNR) for the three methods (the conditioning is on the realization of the weight vector, which, in turn, depends on the covariance matrix estimate). The term CSNR refers to the output effective SNR normalized by the optimal SNR (obtained from the application of the true covariance matrix). The application of the eigencanceler and L-SMI result in high values of the CSNR. Figure 8.6 shows the probability of detection of the three STAP techniques showing similar results as in Figure 8.5. The range ambiguous clutter map is shown in Figure 8.7. The clutter map post-processing is shown in Figures 8.8 and 8.9 for L-SMI and the eigencanceler respectively. The near range clutter masking the target has been rejected and the target is now evident.

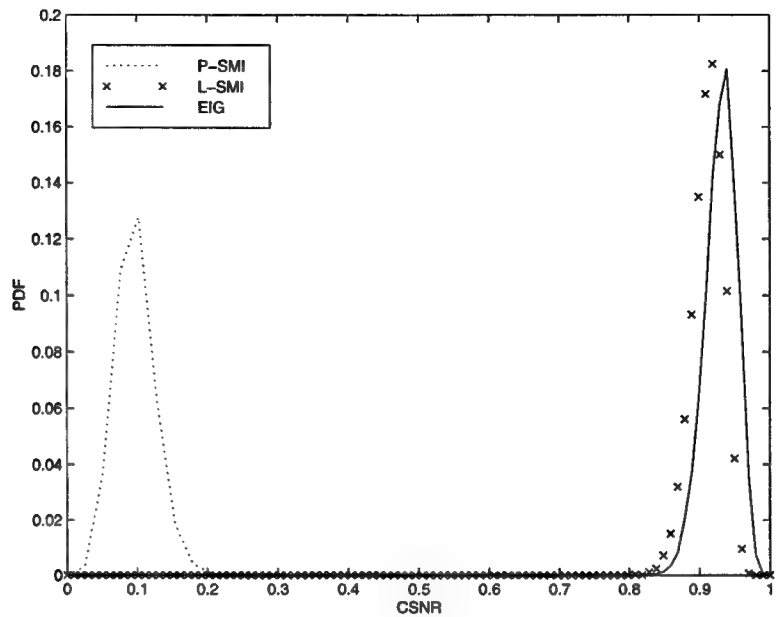


**Figure 8.5** PDF of the CSNR obtained by averaging 2000 runs.

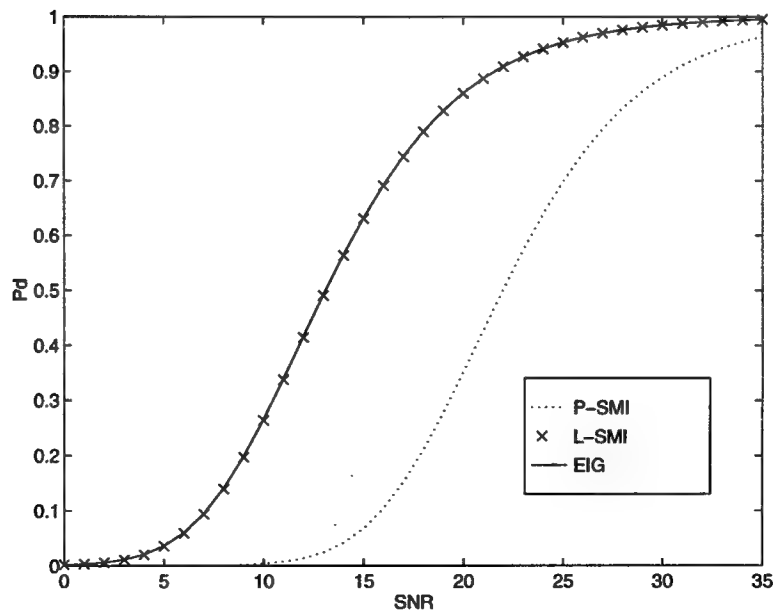


**Figure 8.6** Probability of detection of the CSNR obtained by averaging 200 runs.

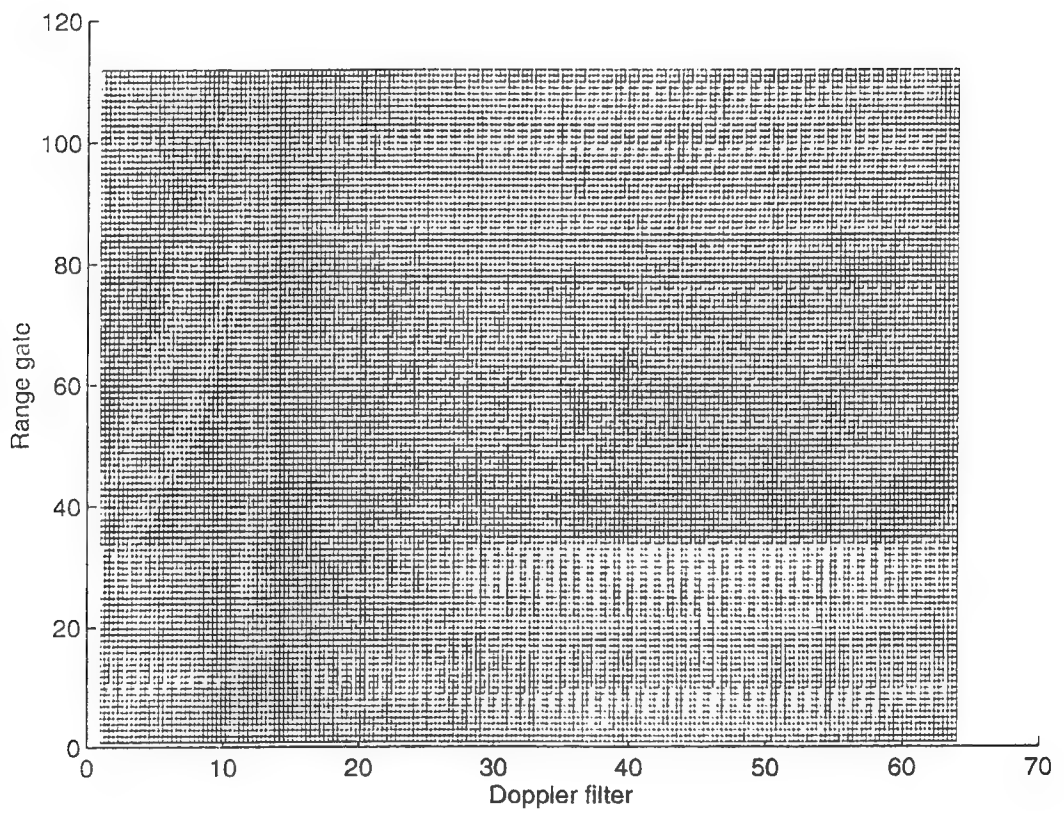


**Figure 8.7** Clutter map for HPRF radar.

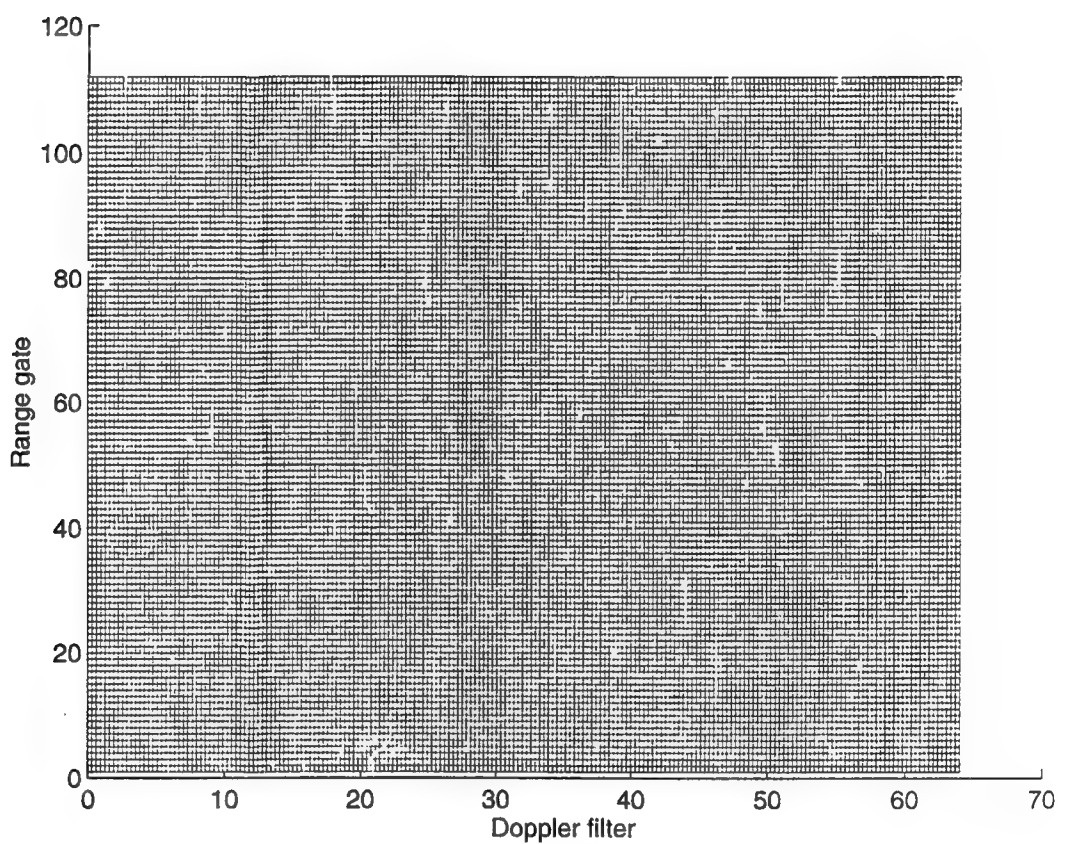


**Figure 8.8** Post-processing clutter using the Loaded SMI.

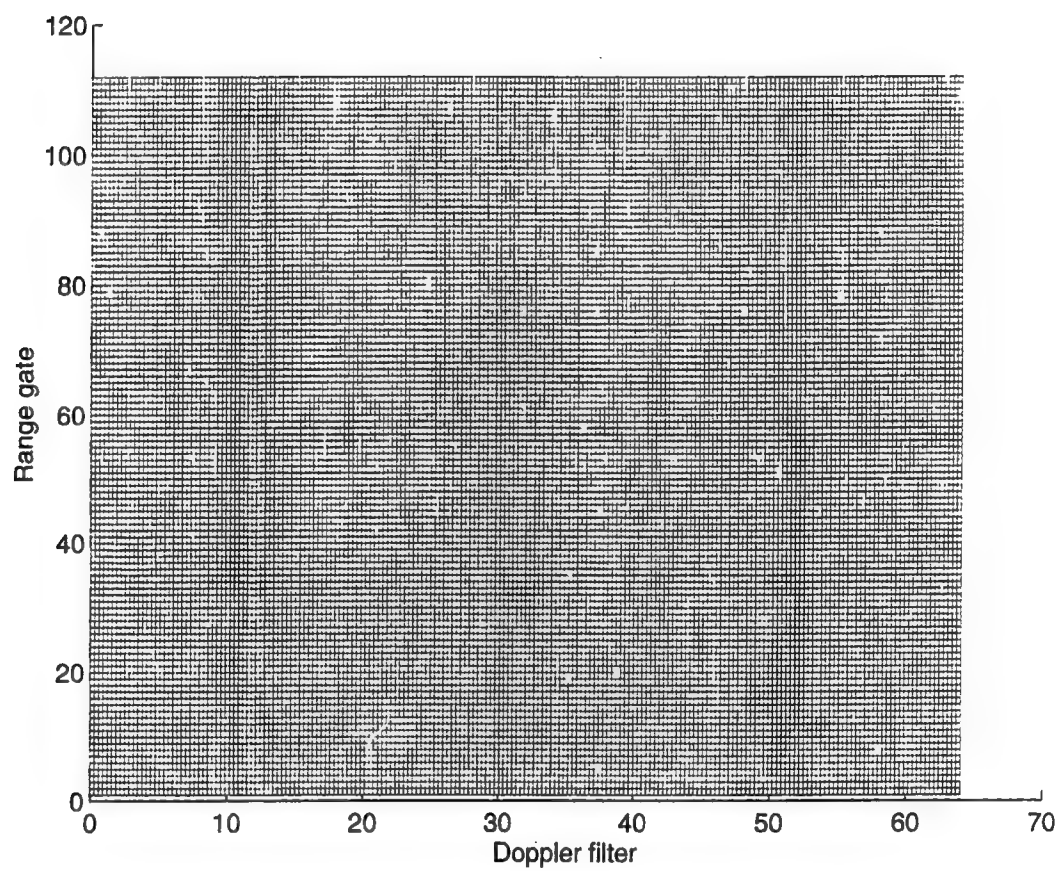


**Figure 8.9** Post-processing clutter using the eigencanceler.

## APPENDIX A

### Derivations of equations (5.25) and (5.26)

This appendix provides the proof to (5.25) and (5.26). From (5.21), and through two consecutive applications of the matrix inversion lemma, one obtains a closed form expression for the inverse of the normalized covariance matrix:

$$\mathbf{R}^{-1} = \mathbf{I} - \gamma_s \mathbf{s} \mathbf{s}^H - \gamma_i \mathbf{s}_i \mathbf{s}_i^H$$

where  $\gamma_s$  and  $\gamma_i$  are defined in section 3. The gain to be calculated is defined in (5.22). Consider the numerator and denominator of  $G$ , for the SMI weight vector in (5.23):

$$\text{NUM1} = |\tilde{\mathbf{s}}^H \mathbf{R}^{-1} \mathbf{s}|^2 \quad (\text{A.1})$$

$$= |\rho_1|^2 (1 - \gamma_s)^2 \quad (\text{A.2})$$

where the inner product between the presumed and true steering vectors is  $|\rho_1|^2 = |\tilde{\mathbf{s}}^H \mathbf{s}|^2 = \frac{1}{N} \frac{\sin^2 N\psi}{\sin^2 \psi}$ ,  $\psi$  is the angle between the vectors as shown in Figure A.1, and it is assumed that  $\mathbf{s}^H \mathbf{s}_i = 0$ . The denominator of the gain term is given by:

$$\text{DEN1} = \tilde{\mathbf{s}}^H \mathbf{R}^{-1} \mathbf{R}_i \mathbf{R}^{-1} \tilde{\mathbf{s}} \quad (\text{A.3})$$

$$= \tilde{\mathbf{s}}^H \left( \mathbf{I} - \gamma_s \mathbf{s} \mathbf{s}^H - \gamma_i \mathbf{s}_i \mathbf{s}_i^H \right)^2 \tilde{\mathbf{s}} \quad (\text{A.4})$$

$$= \tilde{\mathbf{s}}^H \left[ \mathbf{I} - \gamma_s (2 - \gamma_s) \mathbf{s} \mathbf{s}^H - \gamma_i (2 - \gamma_i) \mathbf{s}_i \mathbf{s}_i^H \right] \tilde{\mathbf{s}} \quad (\text{A.5})$$

where  $\mathbf{R}_i = \mathbf{I} + \bar{\sigma}_i^2 \mathbf{s}_i \mathbf{s}_i^H$ . Defining  $|\rho_2|^2 = |\tilde{\mathbf{s}}^H \mathbf{s}_i|^2$  we obtain

$$\text{DEN1} = 1 - \gamma_s (2 - \gamma_s) |\rho_1|^2 - \gamma_i (2 - \gamma_i) |\rho_2|^2$$

and relation (5.25) follows.

For the eigencanceler from (5.24) we have:

$$\text{NUM2} = |\tilde{\mathbf{s}}^H \left( \mathbf{I} - \mathbf{s}_i \mathbf{s}_i^H \right) \mathbf{s}|^2 \quad (\text{A.6})$$

$$= |\rho_1|^2 \quad (\text{A.7})$$

and

$$\text{DEN2} = \tilde{\mathbf{s}}^H \left( \mathbf{I} - \mathbf{s}_i \mathbf{s}_i^H \right) \mathbf{R}_i \left( \mathbf{I} - \mathbf{s}_i \mathbf{s}_i^H \right) \tilde{\mathbf{s}} \quad (\text{A.8})$$

$$= 1 - |\rho_2|^2 \quad (\text{A.9})$$

and relation (5.26) follows.

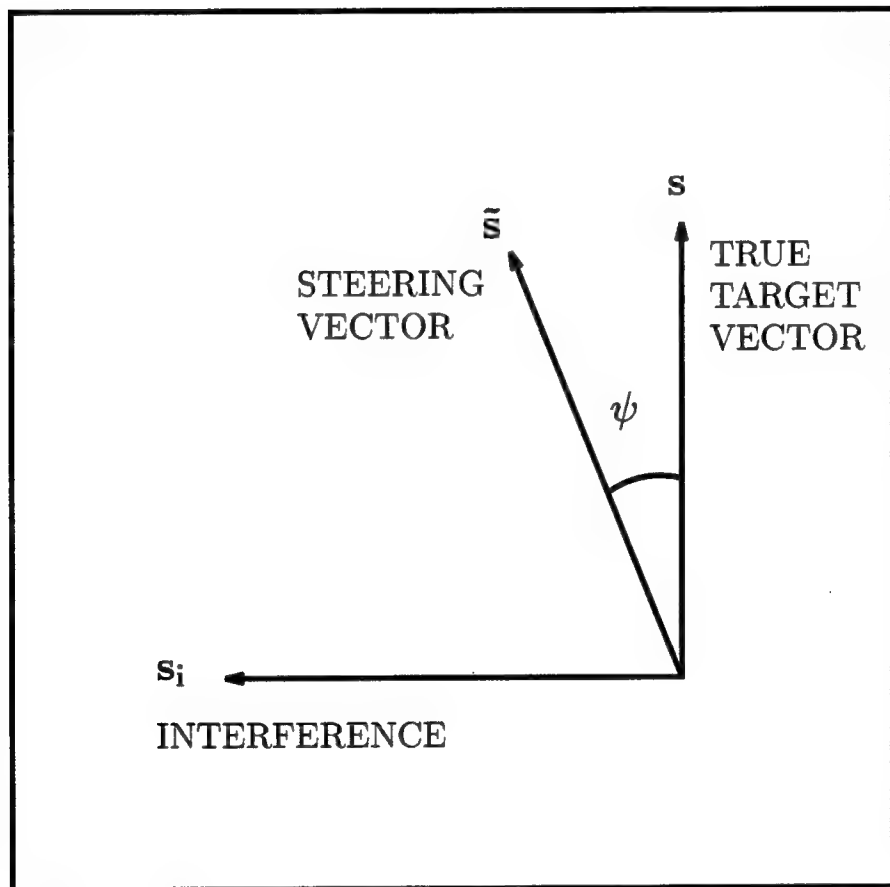


**Figure A.1** Geometry for robustness analysis.

## REFERENCES

1. A. M. Haimovich, "The eigencanceler: Adaptive radar by eigenanalysis methods," *IEEE Transactions on Aerospace and Electronic Systems*, vol. 32, pp. 532–542, April 1996.
2. A. Haimovich, M. Pugh, and M. Berin, "Training and signal cancellation in adaptive radar," in *1996 National Radar Conference*, Ann Arbor, MI, pp. 124–129, May 1996.
3. A. Haimovich, "Asymptotic distribution of the conditioned signal-to-noise ratio in an eigenanalysis-based adaptive array," *IEEE Transactions on Aerospace and Electronic Systems*, vol. 33, no. 3, pp. 988–996, July 1996.
4. A. Haimovich and M. Berin, "Eigenanalysis-based space-time adaptive radar: Performance analysis," *IEEE Transactions on Aerospace and Electronic Systems*, vol. 33, pp. 1170–1179, October 1997.
5. A.M.Haimovich, M.Berin, and X.Wu, "Performance of the eigencanceler: Eigenanalysis space-time adaptive radar," in *Adaptive Sensors Array Processing Workshop*, Lincoln Labs., Lexington, MA, pp. 419–445, March 15-17 1995.
6. A.M.Haimovich and M.Berin, "Signal cancellation effects in adaptive radar mountain-top data set," in *ICASSP'96*, Atlanta, pp. 2614–2617, May 7-10 1996.
7. A. M. Haimovich, C. Peckham, T. Ayoub, J. S. Goldstein, I. S. Reed, "Performance Analysis of Reduced-Rank STAP," *1997 IEEE National Radar Conference*, pp. 42–47, May 13-15 1997.
8. T. F. Ayoub, M. L. Pugh, A. M. Haimovich, "Space-Time Adaptive Processing for High PRF Radar," *IEE Radar'97 Conference*, pp. 468–472, October 14-16 1997.
9. L. E. Brennan and I. S. Reed, "Theory of adaptive radar," *IEEE Transactions on Aerospace and Electronic Systems*, vol. 9, pp. 237–252, March 1973.
10. I. S. Reed, J. D. Mallett, and L. E. Brennan, "Rapid convergence rates in adaptive arrays," *IEEE Transactions on Aerospace and Electronic Systems*, vol. 10, pp. 853–863, November 1974.
11. D. M. Boroson, "Sample size considerations for adaptive arrays," *IEEE Transactions on Aerospace and Electronic Systems*, vol. 16, pp. 446–451, July 1980.
12. R. C. Hanumara, "An alternate derivation of the distribution of the conditioned signal-to-noise ratio," *IEEE Transactions on Antenna Propagation*, vol. 34, pp. 463–464, March 1986.
13. C. G. Khatri, "Effects of estimated noise covariance matrix in optimal signal detection," *IEEE Transactions on Acoustics, Speech, and Signal Processing*, vol. 35, pp. 671–679, May 1987.

14. E. J. Kelly, "An adaptive detection algorithm," *IEEE Transactions on Aerospace and Electronic Systems*, vol. 22, pp. 115–127, March 1986.
15. H. Cox, "Resolving power and sensitivity to mismatch of optimum array processors," *J Acoust. Soc. Amer.*, vol. 54, pp. 771–785, 1973.
16. N. K. Jablon, "Adaptive beamforming with the generalized sidelobe canceller in the presence of array imperfections," *IEEE Transactions on Antenna Propagation*, vol. AP-34, pp. 996–1012, Aug. 1986.
17. M. H. Er and A. Cantoni, "An alternative formulation for an optimum beamformer with robustness capability," *Proc. Inst. Elec. Eng.*, pp. 447–460, Oct. 1985.
18. D. Feldman and L. J. Griffith, "A projection approach for robust adaptive beamforming," *IEEE Trans. Sig. Proc.*, vol. 42, pp. 867–876, Apr. 1994.
19. L. Cai and H. Wang, "Performance Comparisons of Modified SMI and GLR Algorithms," *IEEE Transactions on Aerospace and Electronic Systems*, vol. 27, pp. 487–491, May 1991.
20. R. Nitzberg, *Adaptive Signal Processing for Radar*, Artech House, Norwood, MA, second ed., 1992.
21. A. M. Haimovich, "The eigencanceler: a new space-time interference canceler," in *Proc. '94 IEEE National Radar Conf.*, Atlanta, GA, pp. 194–198, 1994.
22. I. P. Kirsteins and D. W. Tufts, "Adaptive detection using low rank approximation to data matrix," *IEEE Transactions on Aerospace and Electronic Systems*, vol. 30, pp. 55–67, Jan. 1994.
23. R. Monzingo and T. Miller, *An Introduction to Adaptive Arrays*, Wiley and Sons, New York, NY, 1980.
24. A. M. Haimovich and Y. Bar-Ness, "An eigenanalysis interference canceler," *IEEE Transactions on Acoustics, Speech, and Signal Processing*, vol. 39, pp. 76–84, Jan. 1991.
25. I. P. Kirsteins and D. W. Tufts, "Rapidly adaptive nulling of interference," in *High Resolution Methods in Underwater Acoustics* (M. Bouvet and G. Bienvenu, eds.), Springer-Verlag, Berlin Heidelberg, NY, ch. 6, pp. 220–249, 1991.
26. L. E. Brennan, J. D. Mallett, and I. S. Reed, "Adaptive arrays in airborne MTI radar," *IEEE Transactions on Antenna Propagation*, vol. 24, pp. 607–615, September 1976.
27. S. P. Applebaum, "Adaptive arrays," *IEEE Transactions on Antenna Propagation*, vol. 24, pp. 585–594, September 1976.

28. B. e. Widrow, "Adaptive antenna systems," *Proceedings of the IEEE*, vol. 55, pp. 2143–2159, December 1967.
29. W. F. Gabriel, "Using spectral estimation techniques in adaptive processing antenna systems," *IEEE Transactions on Antenna Propagation*, vol. 34, pp. 291–300, March 1986.
30. S. Haykin, *Adaptive Filter Theory*, Prentice Hall, Englwood Cliffs, NJ, second ed., 1991.
31. E. D'Addio, A. Farina, and F. A. Stvder, "The maximum entropy method and its application to clutter cancellation," in *Optimized Radar Processors* (A. Farina and P. Peregrinus, eds.), 1987.
32. J. Capon, "High-resolution frequency wavenumber spectrum analysis," *Proceedings of the IEEE*, vol. 57, pp. 1408–1418, 1969.
33. O. L. Frost III, "An algorithm for linearly constrained adaptive array processing," *Proceedings of the IEEE*, vol. 60, pp. 926–935, August 1972.
34. M. I. Miller and D. L. Snyder, "The role of likelihood and entropy in incomplete data problems: Applications to estimating point-process intensities and Toeplitz-constrained covariances," *Proceedings of the IEEE*, vol. 75, pp. 892–907, July 1987.
35. W. F. Gabriel, "Adaptive arrays: An introduction," *Proceedings of the IEEE*, vol. 64, pp. 239–272, 1976.
36. K. Takao and Komiyama, "An adaptive antenna for rejection of wideband interference," *IEEE Transactions on Aerospace and Electronic Systems*, vol. 16, pp. 452–459, July 1980.
37. W. H. Long and K. A. Harriger, "Medium PRF for the AN/APG-66 radar," *Proceedings of the IEEE*, vol. 73, pp. 310–311, February 1985.
38. W. F. Gabriel, "Spectral analysis and adaptive array superresolution techniques," *Proceedings of the IEEE*, vol. 68, pp. 654–666, June 1980.
39. D. H. Johnson, "The application of spectral estimation methods to bearing estimation problems," *Proceedings of the IEEE*, vol. 70, pp. 1018–1028, Sep. 1982.
40. A. M. Haimovich, *Eigenanalysis Techniques for Canceling Narrowband Interferences*, PhD thesis, University of Pennsylvania, 1989.
41. R. Klemm, "Adaptive clutter suppression for airborne phased array radars," *Proceedings of the IEEE*, vol. 130, Pts. F and H, pp. 125–132, February 1983.
42. K. M. Buckley, "Spatial/Spectral filtering with linearly constrained minimum variance beamformers," *IEEE Transactions on Acoustics, Speech, and Signal Processing*, vol. 35, pp. 249–266, March 1987.

43. L. E. Brennan, D. J. Piwinski, and F. Staudaher, "Space-Time adaptive processing algorithm performance evaluation," in *Proc. IEEE Long Island Section Adaptive Antenna Symposium*, pp. 105–110, November 1992.
44. D. J. Jeffries et. al., "Asymptotic results for eigenvector methods," *Proceedings of the IEEE*, vol. 132, Pt. F, pp. 589–594, December 1985.
45. S. Orfanidis, *Optimum Signal Processing: An Introduction*, McGraw-Hill, New York, NY, second ed., 1993.
46. A. Haimovich and X. Wu, "Eigenanalysis based array processing for mobile communications," in *28th Annual Conf. on Information Sciences and Systems*, Princeton, NJ, pp. 203–208, March 1994.
47. T. Anderson, "Asymptotic theory for principal component analysis," *Ann. Math. Stat.*, vol. 34, pp. 122–148, 1963.
48. R. Gupta, "Asymptotic theory for principal component analysis in the complex case," *J. Indian Stat. Assoc.*, vol. 3, pp. 97–106, 1965.
49. N. Goodman, "Statistical analysis based on a certain multivariate complex gaussian distribution (an introduction)," *Ann. Math. Stat.*, vol. 34, pp. 152–177, 1963.
50. J. Proakis, *Digital Communications 3/e*, McGraw-Hill, New York, 1995.
51. F. Haber, Y. Bar-Ness, and C. C. Yeh, "An adaptive interference canceling array utilizing hybrid techniques," *IEEE Transactions on Aerospace and Electronic Systems*, vol. 19, September 1983.
52. G. T. Zunich and L. J. Griffiths, "A robust method in adaptive array processing for random phase errors," in *Proceedings Int. Conf. Acoust. Speech Signal Processing*, vol. 24 No. 5, Toronto, Canada, pp. 1357–1360, May 1991.
53. A. M. Vural, "Effects of perturbations on the performance of optimum/adaptive arrays," *IEEE Transactions on Aerospace and Electronic Systems*, vol. 15 No. 1, pp. 76–87, January 1979.
54. H. Cox, R. M. Zeskind, and M. M. Owen, "Robust adaptive beamforming," *IEEE Transactions on Acoustics, Speech, and Signal Processing*, vol. 35, pp. 1365–1376, October 1987.
55. K. Gerlach, "The effect of I,Q mismatch errors on adaptive cancellation," *IEEE Transactions on Aerospace and Electronic Systems*, vol. 28, pp. 729–740, July 1992.
56. D. R. Wehner, *High Resolution Radar*, Artech House, Inc., No. wood, MA, 1987.
57. G. W. Titi, "An overview of the arpa mountaintop program," in *1994 Adaptive Antenna Systems Symposium*, Melville, NY, pp. 53–59, Nov. 1994.

58. S. Haykin, *Adaptive Filter Theory*, Prentice Hall, Englewood Cliffs, NJ, third ed., 1996.
59. P. Zulch, *Mountain Top Program Summit Data: ASPA 95 Data Distribution*, Rome Laboratory, Griffiss AFB NY 13441, Rome, NY, March 1995.
60. J. R. Klauder et. al., "The theory and design of chirp radars," July 1960.
61. H. Wang and L. Cai, "On adaptive spatial-temporal processing for airborne surveillance radar systems," *IEEE Trans. on Aero. and Elec. Sys.*, pp. 660–668, July 1994.
62. L. Chang and C. Yeh, "Performance of DMI and eigenspace-based beamformers," *IEEE Trans. on Ant. and Propagation*, vol. 40, pp. 1336–1347, Nov. 1992.
63. J. Goldstein and I. Reed, "Subspace selection for partially adaptive sensor array processing," *IEEE Transactions on Aerospace and Electronic Systems*, vol. 33, no. 2, pp. 539–543, April 1996.
64. J. Goldstein and I. Reed, "Reduced-rank adaptive filtering," *IEEE Transactions on Signal Processing*, vol. 45, no. 2, pp. 492–496, February 1996.
65. B. VanVeen and R. Roberts, "Partially adaptive beamformer design via output power minimization," *IEEE Transactions on Acoustics, Speech and Signal Processing*, vol. 35, pp. 1524–1532, Nov. 1987.
66. D. Marshall, "A two step adaptive interference nulling algorithm for use with airborne sensor arrays," in *Seventh SP Workshop on Statistical Signal and Array Processing*, Quebec City, Canada, pp. 301–304, June 1994.
67. J. S. Goldstein and I. S. Reed, "Theory of partially adaptive radar," *IEEE Transactions on Aerospace and Electronic Systems*, in press.
68. E. Barile, R. Fante, and J. Torres, "Some limitations on the effectiveness of airborne adaptive radar," *IEEE Trans. on Aero. and Elec. Sys.*, pp. 1015–1031, Oct. 1992.
69. J. Ward, "Space-time adaptive processing for airborne radar," *Lincoln Laboratory Technical Report 1015*, Dec. 1994.
70. R. L. Dilsavor and R. L. Moses, "Analysis of Modified SMI Method for Adaptive Array weight Control," *IFAC Identification and System Parameter Estimation*, pp. 417–422, 1991.
71. Y. I. Abramovich, "Controlled method for adaptive optimization of filters using the criterion of maximum signal to noise ratio," *Journal of Communication Technology and Electronics*, vol. 26, pp. 87–95, 1981, translated from Russian.
72. O. P. Cheremisin, "Efficiency of an adaptive algorithm with regularization of the sampled correlation matrix," *Journal of Communication Technology and Electronics*, vol. 27, pp. 69–77, 1982, translated from Russian.

73. C. H. Gierull, "Performance analysis of fast projections of the hung turner type for adaptive beamforming," *Signal Processing*, Elsevier, vol. 50, pp. 17-28, April 1996.